Design, Microfabrication, and Characterization of MHD Pumps and their Applications in NMR Environments

Dissertation submitted to the faculty of Sciences of the University of Neuchâtel, in fulfillment of the requirements for the degree of
"Docteur ès Sciences"

by

Alexandra Homsy

Dipl. Ing. Phys. EPFL

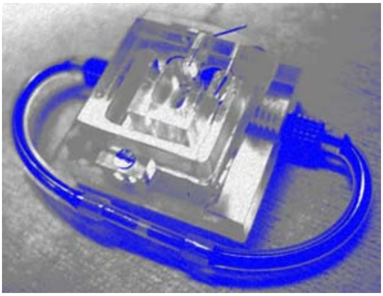

Institute of Microtechnology
University of Neuchâtel
Rue Jaquet-Droz 1, CH-2002 Neuchâtel
Switzerland

2006

Ce travail est dédié

A mes Parents

A ma soeur

IMPRIMATUR POUR LA THESE

Design, Microfabrication and Characterization of MHD Pumps and their Applications in NMR Environments

Alexandra HOMSY

UNIVERSITE DE NEUCHATEL

FACULTE DES SCIENCES

La Faculté des sciences de l'Université de Neuchâtel,
sur le rapport des membres du jury

Mmes M. Koudelka-Hep, E. Verpoorte (RUG, NL)
MM. N. de Rooij (directeur de thèse),
J. Eijkel (UT, NL) et R. Popovic (EPF Lausanne)

autorise l'impression de la présente thèse.

Neuchâtel, le 16 mars 2006

Le doyen :

J.-P. Derendinger

Résumé

Contrôler les petits volumes avec une grande précision est d'une importance cruciale pour la microfluidique et le développement de "systèmes d'analyse intégrés" (µTAS). Dans le cas des puces microfluidiques intégrant l'analyse par résonnance magnétique nucléaire (RMN), un débit volumique faible et précis est même impératif. La RMN est une technique d'analyse chimique très précise et très populaire qui s'effectue dans un environnement à très fort champ magnétique (B_0). Cette thèse vous présente une pompe à l'échelle microfluidique qui utilise la magnétohydrodynamique (MHD) pour manipuler les liquides dans un environnement RMN.

Nous allons commencer par expliquer les phénomènes physiques se cachant derrière la magnétohydrodynamique. Ce phénomène a permis de développer une technique nouvelle permettant de bouger des espèces ioniques en présence à la fois de champs magnétiques et électriques. Les micropompes MHD contrôlent le flux à l'intérieur du système microfluidique en générant une différence de pression le long du microcanal, proportionnelle à l'intensité du courant électrique et au champ magnétique. Pomper des solutions électrolytiques avec la MHD implique la génération de courants électriques continus (DC) dans de tels environnements. Bien que peu de recherche ait été conduite à ce sujet, nos études préliminaires sur un éventail de géométries MHD très simples ont conduit à un design de micropompe MHD idéal pour le pompage en mode DC. Le débit volumique de la micropompe est proportionnel à la densité de courant et à la densité du flux magnétique. La micropompe génère une haute densité de courant DC à travers son canal principal grâce à un alignement de canaux subsidiaires (de chaque côté du canal principal) ne faisant que 100 nm de profond. La génération de bulles dans les canaux due à l'électrolyse a été évitée, les électrodes responsables du phénomènes étant placées dans des réservoirs extérieurs en connexion fluidique avec le système.

En partenariat avec le groupe de design de microsystèmes (IMM - LMIS3) à l'EPFL, nous avons développé un système microfluidique compatible avec la détection RMN. Nous avons démontré qu'il était possible de déplacer avec précision des solutions électrolytiques à l'aide de la magnétohydrodynamique dans les environnements RMN. Le débit maximum généré par notre pompe MHD est de 1.5 $\mu L \cdot min^{-1}$ dans l'aimant supraconducteur RMN.

Mots clés
MicroTAS, Laboratoire sur puce, Microfluidique, Micropompe, Flux magnetohydrodynamique, MHD DC, Analyse RMN

Abstract

Precise control of small volumes of sample is of great interest in microfluidics and for developing portable, micro total analysis systems (µTAS). More specifically, low and precise flow rates are imperative for the manipulation of fluids within an on-chip nuclear magnetic resonance (NMR) system. NMR is a powerful and popular molecular analysis technique that takes place in high static magnetic field environments (B_0). In this thesis, we present a microfluidics-based micropump using magnetohydrodynamics for the manipulation of fluids in an NMR environment.

The physics behind the magnetohydrodynamics (MHD) phenomenon will be discussed first. MHD introduces a novel way to move ionic species in a microfluidic system combining both magnetic and electric fields. Next, the idea of an MHD-based micropump exploiting B_0 to precisely control and manipulate fluids will be presented. Pumping electrolytic solutions with MHD involves the generation of an electric current in such environments. Although not much research has been done on MHD pumping of electrolytic solutions in microchannels, preliminary studies with simple MHD pump designs has led to an ideal microchannel geometry and DC MHD micropump. It is shown that MHD flow rate is directly proportional to both current density and magnetic field intensity. The micropump generates a high DC current density across the pumping channel with the help of an array of nanometer deep side-channels. Bubble generation in the channels due to water electrolysis was avoided by placing the electrodes in outer reservoirs in fluidic connection with the system.

In partnership with the microsystems design group (IMM - LMIS3) at EPFL, we developed a chip-based microfluidic system compatible with NMR detection. We have been able to demonstrate that micropumping of electrolytes based on MHD was possible in NMR environments. The maximum flow rate generated by our MHD pump was 1.5 μL$\cdot$min^{-1} in the NMR superconductive magnet.

Keywords
MicroTAS, Lab on a chip, Microfluidics, Micropump, Magnetohydrodynamic flow, DC MHD, NMR analysis

Contents

List of Figures

Chapter 1

Introduction

A μTAS (micro total analysis system) is defined as a platform, not bigger than a compact disc, which contains all the components necessary to perform the complete analysis of any raw chemical species. In this chapter, we will introduce the concept of μTAS, and explain why there has been many recent advances in the field. The transport mechanisms (namely microfluidics) involved in those systems will be described as well as the technology necessary to build such small and complex devices. The last paragraph of this chapter will be devoted to the scope of the thesis, which was to build a μTAS for NMR (nuclear magnetic resonance) analysis of chemical/biological samples.

1.1 Micro total analysis systems (μTAS)

Chemical analysis are affected by the volumes used, in the sense that smaller volumes will often decrease the response time of an analysis as diffusion times are shortened, mixing is improved, and reaction conditions can be better controlled. Over the past decade, a need for miniaturization in laboratories for low cost, fast and sensitive measurements has developed in many fields, including chemical production, DNA analysis, drug discovery, and environmental analysis [1–6].

The concept of µTAS was first introduced by Andreas Manz and H. Michael Widmer [7–10]. The area of µTAS is growing rapidly, and the idea is to place all the functions carried out in a laboratory room onto a chip (Lab-on-a-chip). Here, all the components necessary for the analysis are assembled into a small device, which performs the whole analysis process in an autonomous fashion. However, instead of assembling the system from discreet components, it is integrated onto a planar, microchip-like platform [11–17]. Those microchips are made of networks of microchannels with dimensions in the range from hundreds down to few micrometers (see section 1.2), which are fabricated in substrates like glass, quartz, silicon, or polymers [18–21]. Miniaturization firstly leads to the reduction of reagent consumption, greater separation efficiencies, and reduced analysis time. On the other hand, the applicability of µTAS for biochemical analysis is also determined by considerations such as improved analytical performance, component integration, increased throughput and automation.

1.2 Microfluidics

Microfluidics refers to devices and methods for controlling and manipulating fluid flow with length scales less than a millimeter. The first microfluidic devices fabricated using microelectronics technology were investigated in the 70's [22–25]. Microfluidic devices are used for various applications such as active/passive valves and micropumps [26, 27], reactors and mixers [28–30], inkjet [31] and pressure flow sensors [32].

In microfluidic systems, the theory of fluid mechanics for macroscopic pipes can be used to calculate liquid flow parameters such as the pressure drop. However, due to the dimensions of the microsystems, not all of macroscopic fluid mechanics can be applied to microfluidic systems [33–36]. Because of its viscous properties, the flow of a fluid inside a channel will be classified either as laminar or turbulent [37, 38]. This will depend on various parameters such as the physical properties, flow rate and geometry of the system. In a laminar flow, the streamlines never intersect. In a turbulent flow, velocity and pressure show random variation with line and space coordinates. The transition to turbulence is when the flow ceases to be laminar to become turbulent.

The parameter which describes the transition is the Reynolds number, *Re*, which is defined by:

$$Re = \frac{vD_h\rho}{\mu} \tag{1.1}$$

where v is the average stream velocity [m·s^{-1}], ρ is the fluid density [kg·m^{-3}], μ is the absolute viscosity [Pa·s], and D_h is the hydraulic diameter. D_h is equal to 4A/P$_w$ where A is the cross sectional area of the channel and P$_w$ is the wetted perimeter of the channel.

Re can be regarded as a ratio of the inertial force to the viscous forces and is a dimensionless parameter. To determine whether a given flow is laminar or turbulent in macroscopic systems, the *Re* is evaluated and compared to the transitional Reynolds number, Re_t, 2300 [39]. In the early 90's, it was demonstrated that the Re_t for macroscopic pipe systems cannot always be used for microfluidic systems to determine the flow regime [33]. However, alternative values or the transitional number were introduced which depend on the ratio between the length of the channel, L, and the hydraulic diameter. According to [33], for $1 < L/D_h < 70$ the transition number is estimated as:

$$Re_t \cong 30\frac{L}{D_h}, 1 < L/D_h < 70 \tag{1.2}$$

Due to the small dimensions of microchannels, the *Re* is usually much less than 100, often less than 1. In this *Re* regime, flow is completely laminar. The transition to turbulent flow generally occurs at *Re* larger than 2000. Laminar flow provides a means by which molecules can be transported in a relatively predictable manner through microchannels. We will see in details in section 2.2.2 how this property of flow will simplify our description of the pressure drop in microchannels.

Table 1.1: Performance comparison for a selection of micropumps. Q_{max} is the value of maximum flow rate achieved by such pumps.

Category	Driver	Working Fluid	Q_{max} [μL·min^{-1}]	Ref.
Displacement	Glass diaphragm	Water	8	[40]
Displacement	PDMS diaphragm	Water	0.1	[41]
Dynamic	EHD	Ethanol	$14\cdot10^3$	[42]
Dynamic	EHD	Water	2	[43]
Dynamic	EO	Tetraborate Buffer	0.2	[44]
Dynamic	EO	Borate Buffer	$33\cdot10^3$	[45]
Dynamic	AC MHD	1M Saline solution	18	[46]
Dynamic	DC MHD	Seawater	63	[47]
Dynamic	Accoustic	Water	0.255	[48]

1.3 Micropumps

In order to pump and precisely control small volumes of sample, micropumps need to be integrated into μTAS. A complete review about micropumps in microscale devices was recently published by D.J. Laser and J.G. Santiago [27]. Micro-fabricated pumps are generally falling into one of two main categories. The *displacement pumps* exert pressure forces on the working fluid through one or more moving boundaries. The *dynamic pumps* continuously add energy to the working fluid in a manner that directly increases either its momentum or its pressure. Table 1.1 compares the performance of a selected sample of micropumps. The magnitude of the generated flow rates is independent of the category, and vary from nL·min^{-1} to mL·min^{-1}.

Displacement pumps

Most of the displacement pumps operate in a periodic manner, incorporating some means of rectifying periodic fluid motion to produce net flow. Such periodic displacement pumps can be further broken down into pumps that are based on reciprocating motion, as of a piston or a diaphragm [41, 49], and pumps that are based on rotary elements such as gears or valves. The majority are reciprocating displacement pumps [40] in which the moving surface is a diaphragm. These are sometimes called *membrane pumps* or *diaphragm pumps*. Another subcategory of displacement pumps are *aperiodic displacement pumps*, the operation of which does not inherently depend on periodic movement of the pressure-exerting boundary. Aperiodic displacement pumps typically pump only a limited volume of working fluid; a syringe pump is a common macroscale example.

Dynamic pumps

Dynamic pumps are based on a direct transformation of non-mechanical or mechanical energy into a continuous fluid movement. A first example are the centrifugal pumps [50]. Those are typically ineffective at low Reynolds numbers and have only been miniaturized to a limited extent. Electrohydrodynamic (EHD) [42, 51], electro-osmotic (EO) [52–57], and magnetohydrodynamic pumps (MHD) [46, 47] use pumping mechanisms in which an electromagnetic field interacts directly with the working fluid [3] to produce pressure and flow. Another example is the acoustic-wave micropump [48].

1.4 Fabrication methods for microfluidic devices

Microfabrication [58] comprises the use of a set of manufacturing tools based on batch processing of thin and thick film commonly used in the electronics industry. The majority of microfluidic devices presented to date rely on such planar fabrication technology which is based on three processes: layer formation, pattern definition and layer removal [59]. Such processes are very critical and necessitate to be handled in a controlled dust-free environment, called cleanroom. At the beginning of microfluidics research in the early 1990s, these techniques were readily available in the field of microfabrication, and were therefore directly adopted for the fabrication of microchannels. Substrates of choice were mono-crystalline silicon, low-alkali glass and fused silica in the form of polished wafers. The wafer surface is covered with an inert material layer, which is subsequently patterned by photolithography. The underlying bulk material can then be etched to form channels, reaction chambers, filters, and the like. After removal of the protective coating used during etching, the still-open microchannels are sealed with a coverplate to form a closed channel network. In most cases, the coverplate has access holes that match up with the ends of the channels to allow filling of the networks with reagents. Since the mid-90s, polymer microfluidic devices have received increasing attention, both because of their low cost and simple fabrication. The development has been driven by the need for inexpensive, rapid prototyping, and disposable microchips for mass markets. On the research end, the quest for rapid-prototyping techniques for laboratory experiments has driven this development. Polymer microfabrication by hot embossing or injection molding allows mass production using a variety of materials with highest precision [60]. Casting and molding of elastomers, especially poly(dimethylsiloxane) (PDMS), has been welcomed by the research community, as it allows rapid replication of microfluidic devices without the requirement of a semiconductor-style cleanroom and hazardous chemistry [61].

1.5 Nuclear Magnetic Resonance (NMR)

The Nuclear Magnetic Resonance (NMR) phenomenon, discovered in 1946, became a standard spectroscopy method in chemistry, physics, and biology. In the early 1970s this physical phenomenon was also used to develop an imaging method for medicine. The aim of this section is to briefly describe the basic phenomena that form the basis of NMR spectroscopy and imaging to help the reader understand the future applications of our µTAS. In addition to this section, the reader is strongly advised to have a look at references [62] and [63].

NMR Spectroscopy

NMR spectrometry exploits the fundamental property of the atomic nucleus that is the nuclear spin I_n. The nuclear magnetic moment m [A·m^2] of a nucleus is related to its angular momentum L [J·s^{-1}] by

$$m = \gamma L \tag{1.3}$$

The ratio γ is called the gyromagnetic ratio [rad·T^{-1}·s^{-1}] and has a different value for each type of nucleus. Due to their natural abundance and large γ, ^{1}H nuclei ($I_n = 1/2$) are extensively used in NMR spectroscopy experiments.

When placed in a static magnetic field B_0, ^{1}H nuclei can adopt one of two spin states corresponding to two possible orientations of the magnetic moment m (parallel or anti-parallel to B_0). These two states are separated by an energy barrier

$$\Delta E = \frac{h\gamma B_0}{2\pi} \tag{1.4}$$

For detection of this transition energy, radiation given by $\Delta E = h\nu$ must be applied, and combining this with Equ. 1.4 gives the fundamental resonance condition for all NMR experiments:

$$\nu_0 = \frac{\gamma B_0}{2\pi} \tag{1.5}$$

The motion of spins in an externally applied magnetic field B_0 is a precession of their magnetic moment m around B_0 at an angular frequency $\omega_0 = -\gamma B_0$ called the Larmor frequency [s^{-1}]. The Larmor frequency corresponds to the resonance frequency of Equ. 1.5. Magnetic moments m of nuclei add up to a macroscopic magnetization M [A·m^{-1}]. At equilibrium, the population difference between spin states corresponds to a bulk magnetization M_0 aligned along B_0.

A very small alternating magnetic field with angular frequency $\omega = \omega_0$ is capable of significantly altering the direction of magnetization. *This effect is the Nuclear Magnetic Resonance (NMR) phenomenon.* The excitation of the spins is given by an applied alternating field $B_{1x}(t) = 2B_1 cos(\omega t)$ perpendicular to B_0 at frequency $\omega = \omega_0$. The field B_1 causes a precession of the magnetization so that after time t, M is at an angle θ with respect to B_0 given by:

$$\theta(t) = \gamma B_1 t \tag{1.6}$$

After a pulse duration τ, the magnetization will return to its equilibrium position aligned along B_0. The NMR signal is obtained by measuring the voltage induced in the detection coil by the rotating magnetization while it returns to its equilibrium position along the axis of B_0. This signal is measured in the time domain as an oscillating, decaying voltage induced in the receiver coil by the magnetization in free precession. This signal is known as the Free Induction Decay (FID), and has a maximum initial amplitude

$$S_0 = \omega_0 M_0 B_1 V_s \tag{1.7}$$

where V_s is the sample volume with uniformly distributed B_1 ($\perp B_0$) and M_0 (same direction as B_0). In most NMR experiments, the time-domain FID is transposed in the frequency domain by way of a Fourier transform. Each peak in the frequency domain will refer to a specific property of the nucleus and its environment, and its position is known as the *chemical shift* δ (in ppm). The chemical shift is a molecular parameter, and depends only on the sample conditions (solvent, concentration, temperature) and not on the spectrometer frequency.

Magnetic Resonance Imaging (MRI)

The imaging technique by magnetic resonance adds spatial encoding to the signal already described for NMR spectroscopy. The spatial encoding of the sample volume is done by the superposition of a linear magnetic field gradient G to the static magnetic field B_0. Nuclear spins at position r will hence resonate at the local Larmor frequency

$$\omega(r) = \gamma(B_0 + G \cdot r) \tag{1.8}$$

The signal contribution from spins occupying a small element of the sample volume dV at position r is proportional to the local spin density $\rho_{spin}(r)$.

The MRI image is obtained by a combination of gradient pulses, RF excitation pulses and data acquisition periods, which together with the order and timing they are applied is known as the *pulse sequence*.

Advantages of NMR analysis

NMR is one of the most powerful chemical analysis techniques. It enables, for example, the identification of components of complex pharmaceutical and natural product mixtures and may also be important in studies of racemization of drug metabolites, a process that often occurs in vivo. The largest challenge to NMR methodology lies in its sensitivity. Compared with other techniques, such as mass spectroscopy, NMR methods for screening mixtures are limited by their relative insensitivity. A boost in sensitivity and screening capacity of the NMR technique is possible by the integration of microcoils in microfluidic devices.

1.6 Research goals of this thesis: an NMR μTAS

This thesis is part of a common FNS project with the group of Prof. Popovic (EPFL-IMM-LMIS3), which is specialized in integrated magnetic sensors. The goal of this collaboration is to explore the integration of Nuclear Magnetic Resonance (NMR) spectroscopy in nL volumes with a microfluidic system for chemical applications. Activities at the EPFL - LMIS focused on the modeling, design, fabrication and evaluation of micro-fabricated probes for NMR detection in μTAS. Our activities at UNINE - SAMLAB focused on the fabrication and optimization of a microfluidic chip-based system compatible with NMR detection.

The research goals of this thesis are to fabricate a microfluidic chip compatible with NMR, to take advantage of the high magnetic field inherent to NMR spectroscopy to pump fluids, and then to choose a chemical demonstrator to evaluate the integration of NMR with the fluidic microsystem.

Bibliography

[1] S.C. Jakeway, A.J. de Mello, and E.L. Russell. Miniaturized total analysis systems for biological analysis. *Fresenius Journal of Analytical Chemistry*, 366:525–539, 2000.

[2] D. Figeys and D. Pinto. Lab-on-a-chip: A revolution in biological and medical sciences. *Analytical Chemistry*, 72:330A–335A, 2000.

[3] G.J.M. Bruin. Recent developments in electrokinetically driven analysis on microfabricated devices. *Electrophoresis*, 21:3931–3951, 2000.

[4] J. Khandurina and A. Guttman. Bioanalysis in microfluidic devices. *Journal of Chromatography A*, 943:159–183, 2002.

[5] E. Verpoorte. Microfluidic chips for clinical and forensic analysis. *Electrophoresis*, 23:677–712, 2002.

[6] B.H. Weigl, R.L. Bardell, and C.R. Cabrera. Lab-on-a-chip for drug development. *Advanced Drug Delivery Reviews*, 55:349–377, 2003.

[7] A. Manz, N. Graber, and H.M. Widmer. Miniaturized total chemical-analysis systems - a novel concept for chemical sensing. *Sensors and Actuators B*, 1:244–248, 1990.

[8] D.R. Reyes, D. Iossifidis, P.-A. Auroux, and A. Manz. Micro Total Analysis Systems. 1. Introduction, Theory, and Technology. *Analytical Chemistry*, 74:2623–2636, 2002.

[9] P.-A. Auroux, D. Iossifidis, D.R. Reyes, and A. Manz. Micro Total Analysis Systems. 2. Analytical standard operations and Applications. *Analytical Chemistry*, 74:2637–2652, 2002.

[10] T. Vilkner, D Janasek, and A. Manz. Micro Total Analysis Systems. Recent developments. *Analytical Chemistry*, 76:3373–3386, 2004.

[11] A. Manz, D.J. Harrison, E.M.J. Verpoorte, J.C. Fettiger, A. Paulus, H. Pauli, and H.M. Widmer. Planar chips technology for miniaturization and integration of separation techniques into monitoring systems - capillary electrophoresis on a chip. *Journal of Chromatography*, 593:253–258, 1992.

[12] K. Seiler, D.J. Harrison, and A. Manz. Planar glass chips for capillary electrophoresis - repetitive sample injection, quantification, and separation efficiency. *Analytical Chemistry*, 65:1481–1488, 1993.

[13] D.J. Harrison, A. Manz, Z.H. Fan, H. Ludi, and H.M. Widmer. Capillary electrophoresis and sample injection systems integrated on a planar glass chip. *Analytical Chemistry*, 64:1926–1932, 1992.

[14] D.J. Harrison, K. Fluri, K. Seiler, Z.H. Fan, C.S. Effenhauser, and A. Manz. Micromachining a miniaturized capillary electrophoresis-based chemical analysis system on a chip. *Science*, 261:895–897, 1993.

[15] C.S. Effenhauser, A. Manz, and H.M. Widmer. Glass chips for high-speed capillary electrophoresis separations with submicrometer plate heights. *Analytical Chemistry*, 65:2637–2642, 1993.

[16] S.C. Jacobson, R. Hergenroder, L.B. Koutny, and J.M. Ramsey. High-speed separations on a chip. *Analytical Chemistry*, 66:1114–1118, 1994.

[17] E. Verpoorte and N.F. de Rooij. Microfluidics meets MEMS. *Proceedings of the IEEE*, 91(6):930–953, 2003.

[18] H. Becker, K. Lowack, and A. Manz. Planar quartz chips with submicron channels for two-dimensional capillary electrophoresis applications. *Journal of Micromechanics and Microengineering*, 8:24–28, 1998.

[19] M. Stjernstrom and J. Roeraade. Method for fabrication of microfluidic systems in glass. *Journal of Micromechanics and Microengineering*, 8:33–38, 1998.

[20] Y. Fintschenko and A. van den Berg. Silicon microtechnology and microstructures in separation science. *Journal of Chromatography A*, 819:3–12, 1998.

[21] K. Hosokawa, T. Fujii, and I. Endo. Handling of picoliter liquid sample in a poly(dimethysiloxane)-based microfluidic device. *Analytical Chemistry*, 71(20):4781–4785, 1999.

[22] J.E. Lilja and S.E. Lennart. Apparatus for sampling, mixing the sample with a reagent and making particularly optical analysis. US patent no 4 088 448, filed 1976.

[23] R. Columbus. Liquid transport device and method. US patent no 4 233 029, filed 1979.

[24] S.C. Terry, J.H. Jerman, and J.B. Angel. A gas chromatographic air analyzer fabricated on a silicon wafer. *IEEE Trans. Electron. Devices*, 26:1880–1886, 1979.

[25] E. Bassous, H.H. Taub, and L. Kuhn. Ink jet printing nozzle arrays etched in silicon. *Applied Physics Letters*, 31:135–137, 1977.

[26] W.K. Schomburg, J. Fahrenberg, D. Maas, and R. Rapp. Active valves and pumps for microfluidics. *Journal of Micromechanics and Microengineering*, 3:216–218, 1993.

[27] D.J. Laser and J. G. Santiago. A review of micropumps. *Journal of Micromechanics and Microengineering*, 14:R35–R64, 2004.

[28] C. Erbacher, F.G. Bessoth, M. Busch, E. Verpoorte, and A. Manz. Towards integrated continuous-flow chemical reactors. *Mikrochimica Acta*, 131:19–24, 1999.

[29] F.G. Bessoth, A.J. deMello, and A. Manz. Microstructure for efficient continuous flow mixing. *Analytical Communications*, 36:213–215, 1999.

[30] N. Lion, T.C. Rohner, L. Dayon, I.L. Arnaud, E. Damoc, N. Youhnovski, Z.-Y. Wu, C. Roussel, J. Josserand, H. Jensen, J.S. Rossier, M. Przybylski, and H.H. Girault. Microfluidics systems in proteomics. *Electrophoresis*, 24:3533–3562, 2003.

[31] C.D. Meinhart and H. Zhang. The flow structure inside a microfabricated inkjet printhead. *Journal of Microelectromechanical Systems*, 9:67–75, 2000.

[32] M. Boillat, B. van der Schoot, P. Arquint, and N.F. de Rooij. Controlled liquid dosing in micro-instruments. In SPIE Conference, editor, *Microfluidic Devices and Systems II*, Santa Clara - California, 1999.

[33] P. Gravesen, O.S. Jensen, and J. Branebjerg. Microfluidics - A review. *Journal of Micromechanics and Microengineering*, 3:168–182, 1993.

[34] P. Tabeling. *Introduction à la microfluidique*. Belin, Paris, 2003.

[35] H.A. Stone, A.D. Stroock, and A. Ajdari. Engineering flows in small devices. *Annual Review of Fluid Mechanics*, 36:381–411, 2004.

[36] D. Sinton. Microscale flow visualization. *Microfluidics and Nanofluidics*, 1:2–21, 2004.

[37] M.C. Potter and D.C. Wiggert. *Mechanics of Fluids*. Second edition, 1997.

[38] A.L. Lydersen. *Fluid Flow and Heat Transfer*. John Wiley and Sons Ltd., 1979.

[39] F.M. White. *Fluid Mechanics, 4th ed.* McGraw-Hill, New York, 1999.

[40] H.T.G. van Lintel, F.C.M. van de Pol, and S. Bouwstra. A piezoelectric micropump based on micromachining of silicon. *Sensors and Actuators*, 15:153–167, 1988.

[41] M.A. Unger, H.-P. Chou, T. Thorsen, A. Scherer, and S.R. Quake. Monolithic microfabricated valves and pumps by multilayer soft lithography. *Science*, 288:113–116, 2000.

[42] A. Richter, K.A. Hofmann, A. Plettner, and H. Sandmaier. The electrohydrodynamic micro flow meter. *IEEE*, pages 935–938, 1991.

[43] G. Fuhr, T. Schnelle T, and B. Wagner. Traveling wave-driven microfabricated electrohydrodynamic pumps for liquids. *Journal of Micromechanics and Microengineering*, 4:217–226, 1994.

[44] P.H. Paul, D.W. Arnold, and D.J. Rakestraw. Electrokinetic generation of high pressures using porous microstructures. In Micro-TAS Conference, editor, *Micro Total Analysis Systems 1998*, Banff - Canada, 1998.

[45] S.H. Yao, D.E. Hertzog, S.L. Zeng, J.C. Mikkelsen, and J.G. Santiago. Porous glass electroosmotic pumps: design and experiments. *Journal of Colloid Interface Science*, 268:143–153, 2003.

[46] A.V. Lemoff and A.P. Lee. An AC magnetohydrodynamic micropump. *Sensors and Actuators B*, 63:178–185, 2000.

[47] J. Jang and S.S. Lee. Theoretical and experimental study of MHD magnetohydrodynamic micropump. *Sensors and Actuators A*, 80:84–89, 2000.

[48] P. Luginbuhl. Microfabricated lamb wave device based on pzt sol-gel thin film for mechanical transport of solid particles and liquids. *Journal of Microelectromechanical Systems*, 6:337–346, 1997.

[49] T. Thorsen, S.J. Maerkl, and S.R. Quake. Microfluidic large-scale integration. *Science*, 298:580–584, 2002.

[50] P. Cooper. *Centrifugal pump theory Pump Handbook*. McGraw-Hill, New York, 2000.

[51] A. Richter and H. Sandmaier. An electrohydrodynamic micropump. *IEEE*, pages 99–104, 1990.

[52] G. Ocvirk, M. Munroe, T. Tang, R. Oleschuk, K. Westra, and D.J. Harrison. Electrokinetic control of fluid flow in native poly(dimethylsiloxane) capillary electrophoresis devices. *Electrophoresis*, 21:107–115, 2000.

[53] A.D. Stroock, S.K. Dertinger, G.M. Whitesides, and A. Ajdari. Patterning flows using grooved surfaces. *Analytical Chemistry*, 74:5306–5312, 2002.

[54] V. Linder. *Polymeric Microfluidic Platforms for Immunodetection*. phd, University of Neuchatel, 2002.

[55] A.D. Stroock and G.M Whitesides. Controlling flows in microchannels with patterned surface charge and topography. *Accounts of Chemical Research*, 36:597–604, 2003.

[56] I. Gitlin, A.D. Stroock, and G.M. Whitesides. Pumping based on transverse electrokinetic effects. *Applied Physics Letters*, 83(7):1486, 2003.

[57] B.J. Kirby and E.F. Hasselbrink Jr. Zeta potential of microfluidic substrates: 1. theory, experimental techniques, and effects on separations. *Electrophoresis*, 25:187–202, 2004.

[58] M.J. Madou. *Fundamentals of microfabrication: the science of miniaturisation*. CRC Press, Boca Raton, Florida, 1997.

[59] J. Lichtenberg. *A Microchip-based Ion Analysis System*. Phd, University of Neuchatel, 2002.

[60] H. Becker and C. Gärtner. Polymer microfabrication methods for microlfuidic analytical applications. *Electrophoresis*, 21:12–26, 2000.

[61] J.C. McDonald, D.C. Duffy, J.R. Anderson, D.T. Chiu, H. Wu, O.J.A. Schueller, and G.M. Whitesides. Fabrication of microfluidic systems in poly(dimethylsiloxane). *Electrophoresis*, 21:27–40, 2000.

[62] C. Massin. *Microfabricated Planar Coils in Nuclear Magnetic Resonance*. Phd, Ecole Polytechnique Fédérale de Lausanne, 2004.

[63] R.J. Abraham, J. Fisher, and P. Loftus. *Introduction to NMR spectroscopy*. John Wiley and Sons Ltd., 1988.

Chapter 2

MHD pumping of electrolytes

In the first section of this chapter, the physics behind the magnetohydrodynamic phenomenon will first be described, then applied to our particular experimental conditions. We will derive from that result that it is crucial to generate a current density of sufficient strength in our microchannels to achieve high pumping efficiency. Next, we will describe how it is possible to generate MHD in microchannels with a DC current in buffered solutions. This chapter will end with a review of the state-of-the-art of MHD micropumps and a discussion about the advantages and limiting factors of MHD pumping.

2.1 The origins of magnetohydrodynamics (MHD)

Magnetohydrodynamics (MHD) is the study of the interaction between magnetic fields and moving, conducting fluids. Magnetic fields influence many natural and man-made flows. They are routinely used in industry to heat, pump, stir and levitate liquid metals. There are three types of magnetic fields; a terrestrial magnetic field which is maintained by fluid motion in the earth's core, a solar magnetic field, which generates sunspots and solar flares, and a galactic field which influences the formation of stars.

The MHD phenomenon was first observed by W. Richie [1] in 1833. The first experiments about magnetic field effects on electrochemical systems date back more than a century ago and have been credited to M. Faraday [2]. However, the development of MHD as an independent scientific discipline started at the first half of the 20th century when astrophysicists realized how ubiquitous magnetic fields and plasmas are throughout the universe. In 1940, H. Alfvén formulated the main principles of MHD, and in 1970 was awarded the Nobel Prize for his pioneering work in MHD. Scientists in several fields are interested in MHD, namely for plasma physics, geophysics, or liquid metal flow engineering [3].

2.2 MHD theory

The governing equations of MHD come from the combination of the theory of electrodynamics and fluid mechanics. They consist simply of Newton's law of motion and the pre-Maxwell forms of the laws of electrodynamics.

2.2.1 From Maxwell's equations to the Lorentz Force

Governing equations of Electrodynamics

We are interested in conducting, non-magnetic, and incompressible liquids. The electromagnetic equations governing MHD for such material properties are described as follows (see [4] for details):

Charge conservation:

$$\overrightarrow{\nabla} \cdot \overrightarrow{J} = -\frac{\partial}{\partial t}\rho_e = 0 \tag{2.1}$$

where J is the current density [A·m^{-2}], and ρ_e the charge density [C·m^{-3}].

Lorentz force in presence of both electrical current and magnetic field:

$$\overrightarrow{F_L} = \overrightarrow{J} \times \overrightarrow{B} \cdot V_D \tag{2.2}$$

where F_L is the Lorentz force [N], B the magnetic flux density [T], and V_D the volume exposed to both J and B. The induced Lorentz force will be maximum when B is orthogonal to J.

J is derived upon Ohm's law:

$$\overrightarrow{J} = \sigma(\overrightarrow{E} + \overrightarrow{v} \times \overrightarrow{B}) \tag{2.3}$$

where σ is the electrical conductivity of the material [S·m^{-1}], E the electric field [V·m^{-1}], and v the velocity of the charged particle [m·s^{-1}].

Governing equations of Fluid Mechanics

In the absence of Lorentz forces, the equation of motion of a small element of fluid as it progresses through a flow field is stated by the Navier-Stokes equation. It comes from the application of the second law of Newton to a small element of fluid of volume δV. The fluid is supposed to be incompressible[1] and Newtonian[2].

Continuity equation:

$$\overrightarrow{\nabla} \cdot \overrightarrow{v} = 0 \tag{2.4}$$

Momentum equation:

$$\frac{D}{Dt}(\overrightarrow{v}) = -\frac{1}{\rho}\overrightarrow{\nabla} P + \eta \nabla^2 \overrightarrow{v} \tag{2.5}$$

where P is the pressure [Pa], ρ is the density [kg·m^{-3}], $\eta = \mu/\rho$ is the kinematic viscosity, μ being the absolute viscosity of the fluid [Pa·s]. The expression $D(.)/Dt$ represents the convective derivative[3]. The boundary condition on v corresponding to equation 2.5 is that $v = 0$ on any stationary solid surface (called also the no-slip condition).

2.2.2 Application to poor conductors

The relative strength of the induced magnetic field is characterized by a dimensionless number [4] called the Magnetic Reynolds number (Rm):

---

[1] Assumption: stream velocity $\ll$ speed of sound

[2] The viscosity of the fluid is constant, and does not depend on the shear rate.

[3] It is the rate of change of a quantity associated with a given element of fluid. Applied to any vector $\overrightarrow{a}$, it will have the following form: $\frac{D}{Dt}(\overrightarrow{a}) = \frac{\partial}{\partial t}(\overrightarrow{a}) + (\overrightarrow{v} \cdot \overrightarrow{\nabla})(\overrightarrow{a})$.

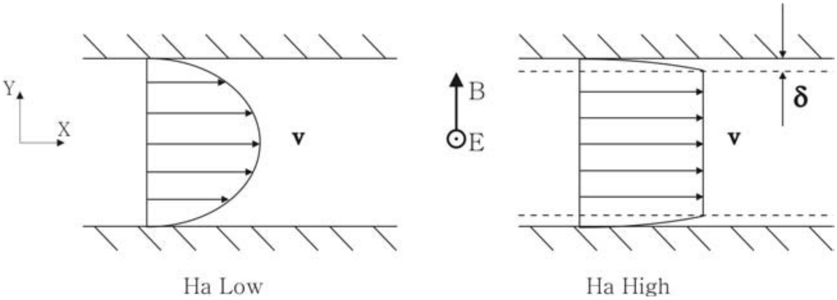

Figure 2.1: Flow profiles at low and large Hartmann numbers.

$$Rm = vl/\lambda \ll 1 \tag{2.6}$$

where l is a characteristic length scale of the flow [m], and λ the magnetic diffusivity [m^2s^{-1}]. Compared to metals or plasma fluids, electrolytes are considered as poor conductors. For such conditions, the Magnetic Reynolds number (*Rm*) of the medium is typically much smaller than 1. In this situation of low *Rm*, the magnetic field B will exert a major influence on the velocity of the charged particles v, but v will not significantly perturb B. In other words, the magnetic field associated with induced currents is negligible compared to the imposed magnetic field.

MHD flow in ducts

When a constant current is injected into a fluid under the influence of a magnetic field, the resulting Lorentz force will, in general, produce motion. *Electromagnetic pumps* were one of the earliest applications of MHD, and were routinely used in metallurgical industries [3]. Those devices consisted of a current perpendicular to a magnetic field, with both fields being perpendicular to the axis of the duct. Assuming the duct filled with a conducting material, the resulting Lorentz force provided the pumping action all along the axis of the duct. MHD flow in ducts was first studied by the engineer J. Hartmann. His work focused on the effects of $\overrightarrow{J} \times \overrightarrow{B}$ on boundary layers. He demonstrated that the flow velocity increases rapidly over a short distance from the wall (see Fig. 2.1). This boundary layer, which has thickness $\sim \delta$ (see [4]), is called a Hartmann layer [4]. The Hartmann number, for a channel of radius r is defined by

$$H_a = r/\delta = B \cdot r \cdot (\sigma/\rho\eta)^{1/2} \tag{2.7}$$

We see that H_a is directly proportional to the conductivity of the fluid.

For H_a close to zero, Hartman flow has a parabolic profile (see Fig. 2.1). Because electrolytes are poor conductors, their corresponding H_a will be close to zero. The MHD flow in a cylindrical pipe is expected to have a parabolic profile.

MHD pumping in microchannels

Due to the small dimensions of microchannels, the Reynolds number (*Re*) will most always be below the transitional Reynolds number (Re_t). In our particular case, we will typically encounter mean flow velocities of 1 mm·sec^{-1} for aqueous buffer solutions in 20 mm long and 75 µm deep semi-circular microchannels. The values for *Re* and Re_t, defined in section 1.2, were calculated to be $Re = 0.15$ with $Re_t = 400$. $Re \ll Re_t$ shows that the flow in our microchannels will always be laminar.

The left part of the fluid mechanics equation 2.5 has the following form:

$$\frac{D}{Dt}(\overrightarrow{v}) = \frac{\partial}{\partial t}\overrightarrow{v} + (\overrightarrow{v} \cdot \overrightarrow{\nabla})(\overrightarrow{v}) \tag{2.8}$$

Because of the laminar flow regime (low *Re*), inertia terms can be neglected. We will have $(\overrightarrow{v} \cdot \overrightarrow{\nabla})(\overrightarrow{v}) = 0$. Equation 2.5 for a low *Re* steady flow ($\frac{\partial}{\partial t}\overrightarrow{v} = 0$) is then:

$$\overrightarrow{\nabla} P = \mu \nabla^2 \overrightarrow{v} \tag{2.9}$$

---

[4] $\delta = (\rho\eta/\sigma B^2)^{1/2}$

The solution of equation 2.9 with the no-slip condition at the walls gives a parabolic flow distribution with a maximum for the velocity at the very middle of the channel. Such flows were studied by G. Hagen and J.L. Poiseuille in 1940 [5], both of whom established the 1-D pressure-drop law:

$$\Delta P = Q \cdot R_{hy} \tag{2.10}$$

where ΔP is the pressure drop in the channel [Pa], Q is the volumetric flow rate [$\mathrm{m}^3 \cdot \mathrm{s}^{-1}$], and R_{hy} is the hydraulic resistance of the channel [$\mathrm{N \cdot s \cdot m^{-5}}$]. A channel of rectangular cross-section will have the following expression for the hydraulic resistance [6, 7]:

$$R_{hy} = \frac{8\mu L(w+h)^2}{w^3 h^3} \tag{2.11}$$

for channels of half-circular cross-section [8]:

$$R_{hy} = \frac{128\mu L}{3\pi h^4} \tag{2.12}$$

and for capillaries of circular cross-section:

$$R_{hy} = \frac{8\mu L}{\pi h^4} \tag{2.13}$$

where w is the channel width, h is the channel height, and L is the total channel length.

MHD flow in a microchannel has a parabolic-shaped profile. The Lorentz force acts on the whole body of the fluid, and generates a body force (which can be seen as a pressure drop) ΔP in the microchannel. This ΔP acting on the cross-sectional area A of the channel by the Lorentz force (Equ. 2.2) is then

$$\Delta P = \frac{F_L}{A} = \frac{J \cdot B \cdot V_D}{A} = \frac{J \cdot B \cdot A \cdot l}{A} = J \cdot B \cdot l \quad (\text{if } \overrightarrow{J} \perp \overrightarrow{B}) \tag{2.14}$$

where l is the channel length on which both perpendicular current and magnetic field are applied[5]. We then equate the expressions 2.10 and 2.14. If no additional pressure gradient is imposed on the channel (e.g. by gravity), we can obtain the following relationships for the volumetric flow rate and average linear flow velocity induced by MHD in microchannels:

$$Q = \frac{J \cdot B \cdot l}{R_{hy}} \tag{2.15}$$

$$v = \frac{J \cdot B \cdot l}{A \cdot R_{hy}} \tag{2.16}$$

As we see in equations 2.15 and 2.16, the flow rate and average flow velocity are proportional to the applied current density and magnetic field, as well as to a geometric constant for the channel.

2.3 Pumping electrolytes with MHD in the DC mode

MHD flow rate is proportional to magnetic field strength and current density. The magnetic field in our case is DC and will have discrete values, depending on the strength of the permanent magnets or on the voltage applied to the NMR coil. The magnetic field will not interact with the ions in the solution if those are not moving (i.e. no current). When a DC current is generated in an ionic solution it will be accompanied by chemical changes at the electrode location. In this section we will describe the chemical and transport processes accompanying a high DC current generation in electrolyte solutions.

2.3.1 High DC current generation in electrolytes

Electrolysis

High DC current generation (i.e. $I \geq 0.1$ mA) in a ionic aqueous solution is always associated with electrolysis. The application of a potential

---

[5] $l \neq L$, the total length of the channel

difference across electrodes in an electrolytic medium will drive chemical changes at the electrode locations. The ions in the solution will carry charges between the electrodes.

When a DC voltage greater than the *electrode potential* (E_p) is applied across platinum electrodes immersed in an aqueous NaCl solution, the following electrochemical reactions will occur [9, 10]:

Anode:

$$2H_2O \rightleftharpoons O_2 + 4H^+ + 4e^- \tag{2.17}$$

Cathode:

$$2H_2O + 2e^- \rightleftharpoons H_2 + 2OH^- \tag{2.18}$$

The positive electrode, called *anode*, will oxidize water and produce oxygen gas. The negative electrode, called *cathode*, will reduce water and produce hydrogen gas. The term *electrolysis*, as well as *electrode*, *anode*, *cathode*, and *electrolyte* were introduced by M. Faraday in 1835 [11]. Other reactions may occur at the electrodes as well, depending on the composition of the electrolyte and the magnitude of the applied voltage. In our case, the oxidation of chloride ($2Cl^- \rightleftharpoons Cl_2 + 2e^-$) will also take place at the anode. The medium around the positive electrode will become more and more acidic, whereas the one around the negative electrode will become alkaline. Gas production at the electrodes by electrolysis is the phenomenon responsible for the formation of bubbles. The rate of bubble generation will be related to the current density.

pH control

The change in pH at the electrode location is a phenomenon that can be controlled. The rate at which the pH changes will depend on the amount of hydroxide and hydronium ions produced at both electrode locations. M. Faraday showed that the number of moles N_x of ion X produced after a time t at a current I is:

$$N_x = \frac{I \cdot t}{a \cdot F} \tag{2.19}$$

where $F = 9.6487 \cdot 10^4$ is the Faraday constant [$\mathrm{C \cdot mol^{-1}}$], and a is the valence of ion X.

In order to regulate the concentration of hydroxide and hydronium ion concentrations, buffer solutions are used. Buffers are defined as *substances which by their presence in solution increase the amount of acid or alkali that must be added to cause unit change in pH* [12]. The intensity of buffer action, that is, the effectiveness with which a solution resists changes in hydrogen ion concentration, is called the *buffer capacity* [13]. In our case, a high buffer capacity is essential to maintain a stable pH in the pump during the course of an experiment.

Choice of electrode

The physical and chemical properties of the electrode material are also of crucial importance, as it will have a great influence on the electrochemical processes at the electrode/solution interface. With some electrodes, a particular electrochemical reaction may occur slowly or not at all; but with another type, the rate of reaction may be increased under the same set of conditions. One of the most widely used electrode material is platinum; this is mostly due to its stable and well characterized electrochemical behavior. For that reason, we decided to use platinum for the work described herein.

Choice of electrolyte solutions

Any conductive solution may be used to generate the current necessary for generating a MHD flow. However, a particular choice of electrolyte solution may be necessary if the μTAS system is sensitive to the side effects of electrolysis. If gas bubble formation has to be avoided, a non-aqueous solution with redox species [14–17] may be chosen. Buffers with high capacity are also of great interest in MHD pumping if one wants to avoid large pH gradients in between the electrodes.

Heat generation

When the temperature rises in the system, the heat will influence, among other things, the sample stability, buffer viscosity, chemical equilibria, pH and the resulting migration time for any given species. *Joule heating* refers to the increase in temperature of a conductor as a result of resistance to an electrical current flowing through it. In capillary electrophoresis systems, the control of this phenomenon is of crucial interest and has been extensively studied. It was found that the magnitude of the capillary temperature, as well as the temperature gradients, are proportional to the power dissipation [18]:

$$Q_d = \frac{U\,I}{L} = E\,I \tag{2.20}$$

where Q_d is the power dissipation [W·m^{-1}], U is the applied voltage [V], I is the current [A], and L is the overall length [m].

In microfluidic systems, Joule heating becomes problematic for Q_d values [19] larger than 3 W·m^{-1} (instead of 1 W·m^{-1} for standard capillaries).

2.3.2 Ion transport and electrokinetic flows

Ion transport

The rate of any transport process is characterized by its *flux*, which is the amount of substance which passes through a unit area during 1 second. In the case of the displacement of charges, this *flux* is the electrical current per unit area, and is called the *current density*. Many phenomena can be at the origin of the displacement of charges.

- Charges can move by diffusion, under the influence of a charge density gradient. This process is governed by Fick's law:

$$\overrightarrow{J_{Fick}} = -D\overrightarrow{\nabla}C \tag{2.21}$$

  where C is the concentration of the ions in the solution [kg·m^{-3}] and

D is the diffusion coefficient[6] [$\mathrm{m}^2 \cdot \mathrm{s}^{-1}$] or diffusivity. D specifies the diffusion rate of the given substance. The minus sign shows that the diffusion flux is oriented from higher to lower concentrations. Adapted to an electrical environment, this law has the following form (both sides of equ. 2.21 were divided by q/m):

$$\overrightarrow{J_D} = -D\overrightarrow{\nabla}\rho_e \tag{2.22}$$

where J_D is the current density originating from diffusion, and ρ_e is the charge density [$\mathrm{C} \cdot \mathrm{m}^{-3}$].

- Charge movement can also be provoked by a body translation (for example a flow). The induced current is then expressed by:

  $$\overrightarrow{J_T} = \rho_e \overrightarrow{v} \tag{2.23}$$

  where v is the velocity of charge translation.

- Charges can also move under the influence of the electric field. In this case, we have the relationship:

  $$\overrightarrow{J_e} = \sigma \overrightarrow{E} \tag{2.24}$$

The total flux of charged substances, or current density J is expressed as the sum of all three contributions we just enumerated which is:

$$\overrightarrow{J} = -D\overrightarrow{\nabla}\rho_e + \rho_e \overrightarrow{v} + \sigma \overrightarrow{E} \tag{2.25}$$

Substituted into Navier-Stokes equation describing the flux of a charged fluid, this expression and the charge conservation equation will give the electrokinetic equation of the charge movement. As it is not the main topic of this thesis, it will not be depicted here.

---

[6] Stokes-Einstein's law describes this coefficient by the theory of Brownian motion, $D = \frac{kT}{6\pi r\mu}$ where k is Boltzmann's constant, T is the absolute temperature [K], r is the ion Stoke's radius [m]

Electrokinetic flow

The transport mechanisms related to the effects of the electric field on a fluid can be divided into three fundamental components: electrophoretic (ep), electro-osmotic (eo), and dielectrophoretic effects [20–23]. Electrophoresis is defined as the motion of charged particles under an applied electric field in a fluid at rest. Electro-osmosis is the induction of motion of an ionic liquid under the effect of an electric field. Dielectrophoresis is the motion of polarizable particles under the influence of a non-uniform electric field. Dielectrophoresis phenomena will not be observable in this work, and will therefore not be treated in this section.

A charged particle in an insulating medium under the influence of the electric field E is subjected to the Coulomb force $F = qE$. In absence of Brownian motion, this particle obeys to equation of motion:

$$q\overrightarrow{E} - \overrightarrow{F_v} = m\frac{d}{dt}\overrightarrow{v} = 0 \tag{2.26}$$

where q [C] is the charge of the ion in the solution. F_v is the viscous force experienced by the moving ion and is given by Stokes law

$$\overrightarrow{F_v} = 6\pi r\mu\overrightarrow{v} \tag{2.27}$$

where r [m] is the ion Stoke's radius. The inertia term in the preceding equation was voluntarily neglected; this is related to Stokes approximation for moving particles at low Reynolds numbers. From those last two equations we deduce the electrophoretic velocity, which is proportional to μ_{ep}, the electrophoretic mobility of the ion. μ_{ep} depends on the chemical nature of the buffer.

$$\overrightarrow{v_{ep}} = \mu_{ep} \cdot \overrightarrow{E} = \frac{q}{6\,\pi\,\mu\,r} \cdot \overrightarrow{E} \tag{2.28}$$

Each ion in the buffer will have a different electrophoretic mobility, depending on both their electric charge and Stokes radius in a solvated medium. Table 2.1 presents examples of radii values [10, 24].

Table 2.1: Stokes radii of selected solvated ions

Ion	radius [Å]
K^+, Cl^-	3
OH^-	3.5
HPO_4^-	4
Na^+	4.5
H^+	9

When a dielectric (like glass) is immersed in an electrolyte, a surface charge appears spontaneously. The mobile charges of the liquid reorganize and form a double layer[7] near the immersed wall. When the electric field is applied in a parallel fashion to the glass capillary, a bulk flow is generated. This electro-osmotic flow is due to the Coulomb force on the mobile part of the electrolyte double layer. In a glass capillary, this layer consists of positive ions which are attracted to the negatively charged capillary wall. The flow of these cations towards the negative electrode causes the whole capillary volume to migrate as a consequence of the viscous drag caused by the movement of the mobile layer. The eo velocity is proportional to μ_{eof}, the eo mobility of the solution in the capillary. μ_{eof} depends on the surface properties of the capillary walls, and on the chemical properties of the solution (buffer pH, ionic strength, etc...).

$$\overrightarrow{v_{eof}} = \mu_{eof} \cdot \overrightarrow{E} = \frac{\varepsilon\,\zeta}{\mu} \cdot \overrightarrow{E} \tag{2.29}$$

where ε [$C \cdot V^{-1} \cdot m^{-1}$] is the dielectric constant of the medium, and ζ [V] is the Zeta potential[8] created at the plane of shear at the channel's wall.

We saw that both eof and ep flows in the microscale are proportional to

---

[7] called the Stern layer

[8] The Zeta potential is the electrical potential at the edge of the Stern layer: $\zeta = \frac{4\pi\rho_e\delta}{\varepsilon}$, where δ is the double layer thickness.

the electric field without any relation to the geometry of the channel (depth of channels for example).

Effect of the Lorentz force on individual moving charges

The expression for the electromagnetic force (the Lorentz force, F_{Li}) on individual moving charge i is expressed by:

$$\overrightarrow{F_{Li}} = q_i \overrightarrow{v_i} \times \overrightarrow{B} \tag{2.30}$$

where q_i and v_i are the charge and velocity of the moving particle i. During electrolysis cations and anions move in opposite directions, so that the signs of q_+v_+ and q_-v_- are both positive by convention (subscripted "+" and "-" denote cations and anions, respectively). As a result, both cations and anions experience their Lorentz forces in the same direction (see Fig. 2.2). The total Lorentz force F_L acting upon a defined volume V_D containing n charge couples (n = n$_+$ + n$_-$) is the sum of the Lorentz forces acting upon all moving ions contained in this volume, and is given by:

$$F_L = (n_+q_+v_+ + n_-q_-v_-) \times B \cdot V_D \tag{2.31}$$

n_+ and n_- are the numbers of cations and anions, respectively. The quantity $(n_+q_+v_+ + n_-q_-v_-)$ is the current density J. Therefore, the equation that

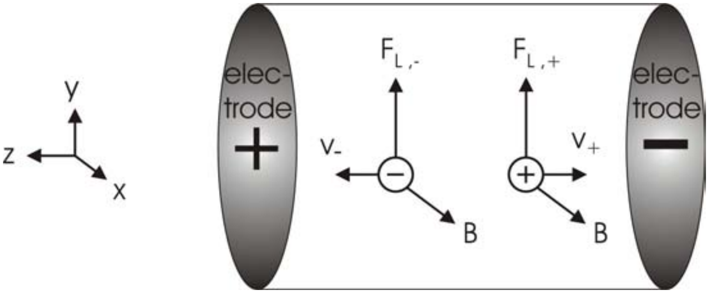

Figure 2.2: Parallel magnetic Lorenz forces on cations and anions migrating towards the negative and the positive electrodes, respectively.

define F_L is identical to that depicted with the macroscopic treatment (see equation 2.2).

2.4 State of the art in MHD micropumps

One of the first demonstrations of MHD pumping of saline solutions (seawater) in microchannels was presented by Jang and Lee in 2000 [25]. The microchannels, made in silicon, were closed, the applied current was DC, and MHD pumping was induced using a permanent DC magnet. The pump was able to produce a maximum flow rate of 63 μL·min^{-1}. However, electrolysis of water led to the formation of gas bubbles in the channel, disrupting the flow. Bau *et al.*. [26, 30–32] studied DC MHD of saline solutions in microchannels made of ceramic tape. Due to gas bubble formation, the microchannels had to be used in an unsealed state[9]. It was also observed that the electrodes, made of gold paste, were consumed very quickly by electrolysis. Redox-based MHD pumping was studied by Leventis *et al.* [14] and more recently by Clark *et al.* [33]. Other groups studied MHD pumping of saline solutions with combined AC magnetic fields and an AC current at high frequencies ($\geq$ 1 kHz) to avoid bubble formation at the electrodes [27–29, 34]. However, MHD pumping in the AC mode leads to low flow rates as a result of the low intensity of the AC magnets. This is because the operation of electromagnets under high frequency and current conditions is limited by induction heating [29] and Eddy current formation [34].

Table 2.2 compares experimental conditions and main properties for a consistent sample of all MHD micropumps published so far. The compared micropumps had channel depths of 3 mm or less, and the pumped solutions were electrolytic solutions. The pumps that had the best performance in term of flow rate and velocity were the ones with maximized J, B and depth of channel (h), and this was achieved by maximizing the channel cross-sectional area (A). On the other hand, the best performances in

---

[9] The device was also left open to facilitate the introduction of fluids and flow visualization, as the tape was not optically transparent

	U (V)	I (mA)	A (mm^2)	A$_J$ (mm^2)	l (mm)	J (A·m^{-2})	B (T)	ΔP$_{MHD}$ (Pa)	v$_{MHD}$ (mm·s^{-1})	Q$_{MHD}$ (µL·min^{-1})
Jang *et al.* [25]	30 DC	1.8	0.4	30	30	60	0.44	1	2.6*	63*
Leventis *et al.* [14]	>1.3 DC	35	18	225	75	155	1.35	16	0.4	$450 \cdot 10^3$
Bau *et al.* [26]	4 DC	15	1.9	292	172	51	0.4	3.5	0.4	45
Lemoff *et al.* [27]	6.6 AC	140	0.2	1.5	4	92105	0.013	5	1.5	18
West *et al.* [28]	5 AC	90	0.2	5	28	17684	0.011	5.5	0.24	3
Eijkel *et al.* [29]	4 AC	40	$6 \cdot 10^{-3}$	2	63	21100	0.1	133	0.04	$14 \cdot 10^{-3}$

Table 2.2: Performance comparison of previously published MHD pumps. All values for voltage (U), current (I), channel cross-sectional area (A), total length of electrodes along the pumping channel (l), MHD flow mean velocity in the pumping channel (v$_{MHD}$) and MHD flow rate (Q$_{MHD}$) were experimental data, and were taken from references [14, 25–29]. Most of values for the electrode cross-sectional area (A$_J$) and current density (J) across the pumping channel had to be calculated. The body force (ΔP$_{MHD}$) generated by the pumps was calculated using relation 2.14. **Both values were taken from experimental measurements. If calculated with relations 2.16 and 2.15, the predicted velocity and flow rate would be 0.16 mm·s^{-1} and 4 µL·min^{-1} respectively.*

terms of generated body force were the pumps with maximized J, B and electrode length (l), and this was achieved by minimizing the electrodes cross-sectional area (A_J).

Applications for MHD pumping reported in the literature include the study of mixing [26, 32, 35], polymerase chain reaction (PCR) [28], separation methods [29, 34], chaotic flow [36], and trace metals analysis [16].

2.5 Advantages of MHD pumping compared to other mechanisms, and limitations

Advantages

Magnetohydrodynamic pumps operate without moving parts, and require only low voltages (less than 10 V) for their actuation. Furthermore, liquid flow does not depend on the chemical nature of the capillary surface unlike in electro-osmotic flow. Forward and reverse flows are possible, with a flow profile similar to that observed for pressure-driven flows. In addition, it can manipulate unprocessed biofluids with wide ranges of properties as long as the solution is at least slightly conductive. For all these reasons, MHD pumping has attracted a growing interest for the handling of conductive fluids in microchannels over the past few years.

Limitations

One of the limitations of MHD pumps are the geometrical constraint associated with the vectorial origin of the Lorentz force (F_L): this force is the body force generating the flow in the MHD pumping channel. For the pumping to occur, F_L is perpendicular to both J and B at the same time, and has to be in the direction of the pumping channel. In an NMR environment, the chip will have to be held horizontally for F_L to be in the plane of the chip (along the pumping channel) with J across the pumping channel. Another limitation is the drastic decrease of the MHD flow rate with the solute ionic concentration. Finally, the change in pH very near to the electrodes, as a consequence of hydrolysis, could also be considered as a limiting factor for MHD pumping as biological specimens are quite sensitive to pH.

Bibliography

[1] W. Ritchie. Experimental researches in electro-magnetism and magneto-electricity. *Philosophical Transactions of the Royal Society of London*, 123:313–321, 1833.

[2] M. Faraday. *Diary*, volume IV 288. London, 1833.

[3] R.S. Tessier and M.-J. Baker. *Handbook of electromagnetic pump technology*. Elsevier Science Publishing Co., 1987.

[4] P.A. Davidson. *An introduction to MHD*. Cambridge University Press, 2001.

[5] F.M. White. *Fluid Mechanics, 4th ed.* McGraw-Hill, New York, 1999.

[6] W.J. Beek and K.M.K. Muttzall. *Transport Phenomena*. John Wiley and Sons Ltd., 1975.

[7] P. Gravesen, O.S. Jensen, and J. Branebjerg. Microfluidics - A review. *Journal of Micromechanics and Microengineering*, 3:168–182, 1993.

[8] E. Oosterbroek. *Modeling, design and realization of microfluidics components*. PhD thesis, University of Twente, 1999.

[9] J. Koryta. *Ions, Electrodes, and Membranes*. John Wiley and Sons Ltd., 1982.

[10] J. Koryta. *Principles of electrochemistry*. John Wiley and Sons Ltd., 1987.

[11] M. Faraday. *Experimental Researches in Electricity*, volume 7th Series. London, 1834.

[12] D.D. Van Slyke. On the measurement of buffer values and on the relationship of buffer value to the dissociation constant of the buffer and the concentration and reaction of the buffer solution. *Journal of Biological Chemistry*, 52:525–570, 1922.

[13] R.G. Bates. *determination of pH*. John Wiley and Sons Ltd., 1973.

[14] N. Leventis and X. Gao. Magnetohydrodynamic electrochemistry in the field of Nd-Fe-B magnets. Theory, experiment, and application in self-powered flow delivery systems. *Analytical Chemistry*, 73:3981–3992, 2001.

[15] E.A. Clark, P.U. Arumugam, and I. Fritsch. Control of fluid flow using redox magnetohydrodynamics for chip-based microfluidics and analytical applications. In Inc. The Electrochemical Society, editor, *206th meeting*, 2004.

[16] E.A. Clark and I. Fritsch. Anodic stripping voltametry enhancement by redox magnetohydrodynamics. *Analytical Chemistry*, 76:2415–2418, 2004.

[17] J.S. Wilkes, M.L. Williams, and R.L. Musselman. Electrochemical magnetohydrodynamic pumping of ionic liquids. *Electrochemistry*, 8:742–744, 2005.

[18] R.J. Nelson, A. Paulus, A.S. Cohen, A. Guttman, and B.L. Karger. Use of Peltier thermoelectric devices to control column temperature in high-performance capillary electrophoresis. *Journal of Chromatography*, 480:111–127, 1989.

[19] A.M. Garcýa Campana, W.R.G. Baeyens, H.Y. Aboul-Enein, and X. Zhang. Miniaturization of capillary electrophoresis systems using micromachining techniques. *Journal of Microcolumn Separations*, 10(4):339–355, 1998.

[20] P.D. Grossman and J.C. Colburn. *Capillary Electrophoresis "Theory and Practice"*. Academic Press, San Diego, CA, 1992.

[21] A. Manz, C.S. Effenhauser, N. Burggraft, D.J. Harrison, K. Seiler, and K. Fluri. Electroosmotic pumping and electrophoretic separations for miniaturized chemical analysis systems. *Journal of Micromechanics and Microengineering*, 4:257–265, 1994.

[22] Baker. *Capillary Electrophoresis*. 1995.

[23] H. Girault. *Electrochimie physique et analytique*. Presses Polytechniques et Universitaires Romandes, 2001.

[24] J.M. Bockris and A.K.N. Reddy. *Modern electrochemistry*, volume 1. Plenum Press, 1970.

[25] J. Jang and S.S. Lee. Theoretical and experimental study of MHD magnetohydrodynamic micropump. *Sensors and Actuators A*, 80:84–89, 2000.

[26] H.H. Bau, J. Zhong, and M. Yi. A minute magnetohydrodynamic (MHD) mixer. *Sensors and Actuators B*, 79:207–215, 2001.

[27] A.V. Lemoff and A.P. Lee. An AC magnetohydrodynamic micropump. *Sensors and Actuators B*, 63:178–185, 2000.

[28] J. West, B. Karamata, B. Lillis, J.P. Gleeson, J. Alderman, J.K. Collins, W. Lane, A. Mathewson, and H. Berney. Application of magnetohydrodynamic actuation to continuous flow chemistry. *Lab On a Chip*, 2:224–230, 2002.

[29] J.C.T. Eijkel, C. Dalton, C.J. Hayden, J.P.H. Burt, and A. Manz. A circular ac magnetohydrodynamic micropump for chromatographic applications. *Sensors and Actuators B*, 92:215–221, 2003.

[30] J. Zhong, M. Yi, and H.H. Bau. Magneto hydrodynamic (MHD) pump fabricated with ceramic tapes. *Sensors and Actuators A*, 96:59–66, 2002.

[31] H.H. Bau, J. Zhu, S. Qian, and Y. Xiang. A magnetohydrodynamically controlled fluidic network. *Sensors and Actuators B*, 88:205–216, 2003.

[32] S. Qian and H.H. Bau. Magneto-hydrodynamic stirrer for stationary and moving fluids. *Sensors and Actuators B*, 106:859–870, 2005.

[33] P.U. Arumugam, E.A. Clark, and I. Fritsch. Use of paired, bonded NdFeB magnets in redox magnetohydrodynamics. *Analytical Chemistry*, 77:1167–1171, 2005.

[34] J.B. Bao and D.J. Harrison. Fabrication of microchips for running liquid chomatography by magnetohydrodynamic flow. In *7th International Conference on Miniaturized Chemical and Biochemical Analysis Systems*, pages 407–410, Squaw Valley, California, USA, 2003.

[35] J. West, J.P. Gleeson, J. Alderman, J.K. Collins, and H. Berney. Structuring laminar flows using annular magnetohydrodynamic actuation. *Sensors and Actuators B*, 96:190–199, 2003.

[36] Y. Xiang and H.H. Bau. Complex magnetohydrodynamic low-reynolds-number flows. *Physical Review E*, 68:016312, 2003.

Chapter 3

DC MHD pump developments

The evolution of our experimental research in DC MHD pumping will be presented in this chapter. Experimental conditions are described first. These conditions changed as we gained a better understanding of the many phenomena associated with DC MHD in electrolyte environments. Three generations of microfluidic chips have been designed and tested. The MHD phenomenon was studied in the devices with electrolytic solutions of high ionic strength. The electrode and channel layout improved with each generation. The common parameters for all experiments included a static magnetic field (permanent magnet) and a DC voltage applied between two electrodes. The main parameters responsible for MHD flow are the magnetic field strength and the electrical current between the electrodes (expressed in equation 2.16). In our case, the magnetic field is a permanent magnet with a fixed field strength (between 0.2 and 0.4T). Therefore, the current is the only parameter that can be modulated in our experiments. We focused on designing microfluidic channels with integrated electrodes which could generate a high current density inside the channel.

3.1 Experimental conditions

3.1.1 Electrolyte properties

Saline solutions

The electrolytes used for the first experiments (described in the following sections) were NaCl and KCl in DI water. Their concentration varied from 0.01 M to 1 M. The most frequently used concentration was 0.1 M. The resistivity of these solutions were measured to be $5 \cdot 10^4$ Ω·m for DI water, 0.69 Ω·m for 0.1 M KCl, and 0.12 Ω·m for 1 M NaCl. The initial pH of saline solutions was also measured. The pH of the solutions was varied by adding drops of 0.1 M NaOH. This resulted in pH ranges around 9 - 10. The values for the absolute viscosity were taken from [1]. They are based on the values of aqueous solutions of NaCl at 20°C. The absolute viscosity is $1.095 \cdot 10^{-3}$ $N \cdot m^{-2} \cdot s$ for 1 M NaCl, and $1.008 \cdot 10^{-3}$ $N \cdot m^{-2} \cdot s$ for 0.1 M NaCl. Polystyrene beads are diluted in the saline solution for the observation of the flow . Three different kinds of beads were used: the 2 to 6 µm diameter carboxylate-modified beads and 1 µm diameter amine-modified beads came from Polysciences Europe GMBH (Germany) and the 2.5 µm diameter AlignFlow beads came from Invitrogen AG (Switzerland).

Buffer solutions

In the experiments described in chapters 4 and 6, buffered solutions were preferred, as they enabled a better control on the pH of the solution between the electrodes [2]. Citrate-phosphate buffer was chosen for the experiments, because it works in a wide range of pH (from 2 to 8) with the possibility of adjusting the ionic strength between 0.25 M to 1 M. Buffer solutions of varying pH but constant ionic strength have been described by Elving *et al.* [3]. The buffer compositions were selected from the McIlvaine formulas [4], and the desired ionic strength is maintained by the addition of potassium chloride. Details about the proportion of all three specific species as a function of the desired pH and ionic strength is found in Appendix D.

3.1.2 Magnet properties

For all experiments in our laboratory we used rare earth NdFeB permanent magnets. They come from two different providers, namely Maurer Magnetic AG (Switzerland) and Forcefield (CO, USA). With the help of K. Ehrmann and C. Massin from the LMIS3 laboratory at EPFL, we first performed an estimation of the intensity of the magnetic field (B) and its direction in the microchannel using the finite element software Maxwell 3D (Ansoft corp, PA, USA). An example of the magnitude and shape of B, as a function of the channel's distance to the center of the magnet, is shown in Fig. 3.1. As a result, we could predict the variation of the intensity of the field (from 0.25 to 0.4 T) as a function of the distance between the microchannel and the surface of the magnet (from 500 µm to 5 mm). The dimensions of the magnets varied in thickness (from 5 mm to 28 mm) and in width (from 10 to 50 mm diameter). The direction of the magnetic field was very uniform in the center of the magnet's surface (see Fig. 3.1). In the experiments, magnets with the wider diameters[1] were preferred as they provided the most uniform magnetic field perpendicular to the plane of the chip.

The intensity of the field for each magnet was confirmed by measurements with a 3-axis magnetic-field transducer (model 3MR-1C, Sentron AG, Switzerland). Special care was taken to position the Hall sensor at the exact height corresponding to the channel position where pumping occurred. This measurement of the accurate magnetic field intensity in the channel enabled us to compare our measurements with the expected velocity calculated from theory (see equation 2.16).

3.1.3 Experimental methods

An example for a typical DC MHD experimental setup is shown in Fig. 3.2. In the first set of experiments, a HP E3617A (Duebendorf, Switzerland) voltage source was used for the experiments in the DC mode. The current compliance of the source was limited to 100 mA. The source was

---

[1] Diameter of the magnets bigger than the outer dimensions of the chip.

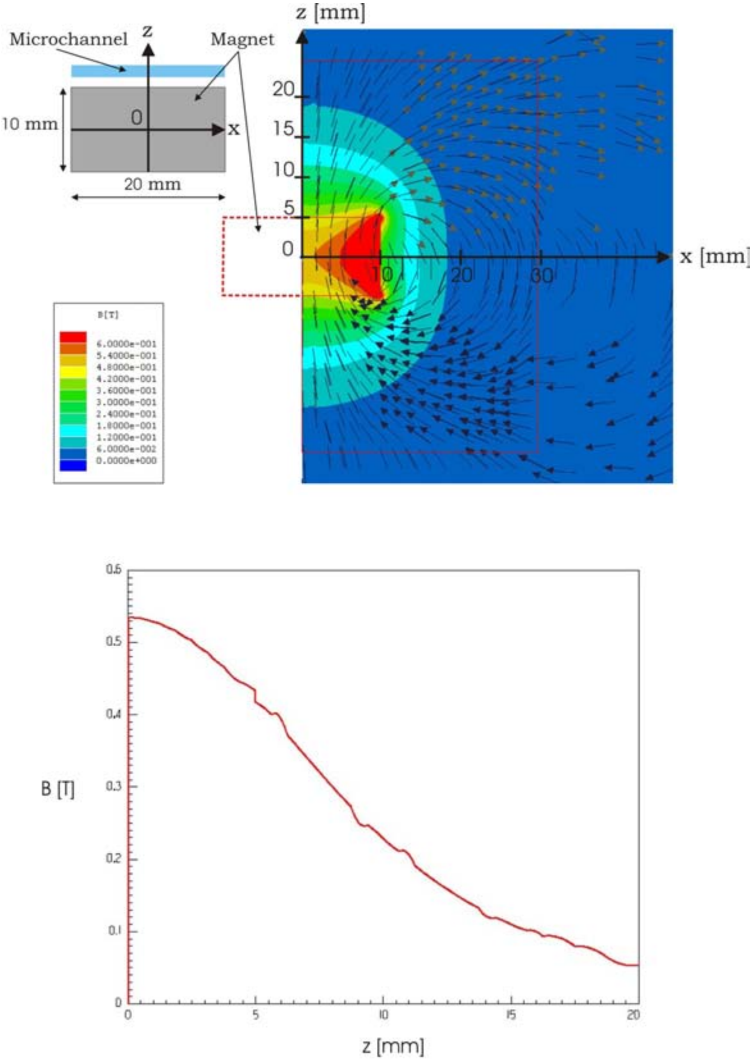

Figure 3.1: (Top) Magnet shape and magnetic field direction. (Bottom) Magnitude of magnetic field B along the z axis (from center of magnet).

able to generate DC voltages up to 60 V, which is large enough for our experiments. The current generated in the channel was measured in series with a high impedance ampmeter from Keithley Instruments S.A. (Zurich, Switzerland). A constant voltage (0 - 60 V) was applied across two electrodes. Most of the experiments used pure platinum electrodes for the generation of ionic current, but some measurements were also taken with silver/silver-chloride electrodes. The constant voltage generated a constant current across the electrodes. The current range was set between 0.6 to 5 mA, depending on the experiment. Note that the current was not completely constant, as it depended also on the chemical environment around the electrodes. However, the standard deviation of the current generated across the channel was also measured. In the later experiments (described in Ch. 6), a constant current was applied across two Pt electrodes with a Keithley 2400 source meter, the compliance of the source was set to 4 mA, and the corresponding voltage didn't exceed 10 V.

We characterized the MHD flow by observing the movement of polystyrene beads in the solution. We used a stereoscopic microscope (Leica AG, Glattbrugg, Switzerland) which was connected to a JVC digital camera (Spitzer Electronics AG, Oberwill, Switzerland) for visual observation. The linear flow velocity was determined by measuring the time required for beads to travel a distance between two defined points in the pumping channel. For our measurements, we selected the fastest moving beads to determine experimentally the maximum velocity for each condition. For a parabolic flow profile, those beads will be located in the middle of the channel. The maximum velocity was calculated by averaging the velocity of the 10 fastest moving beads from a population of 50 beads. Errors for the measurement were based on the standard deviation calculated for the 10 data points.

3.2 MHD in a PDMS T-Channel

Our first MHD flow study consisted of a simple microchannel design, fabricated by rapid-prototyping of poly(dimethylsiloxane) (PDMS) elastomer material. Design considerations included: ***1)*** ease of chip manufacture ***2)***

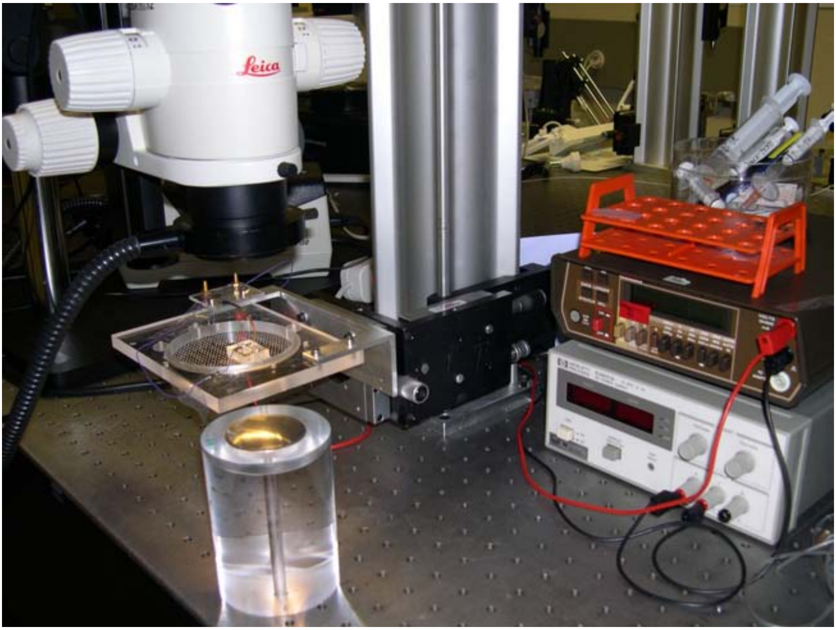

Figure 3.2: View of the experimental setup

use of a constant, homogeneous magnetic field ***3)*** placement of the electrodes in the outer reservoirs of the device. For ease of chip manufacturing, we used PDMS. The use of a constant magnetic field ensured experimental conditions resembling those inside the strong magnet used for the NMR analysis at EPFL. The generation of gas bubbles in the microchannel was prevented by placing the electrodes in the outer reservoirs.

Fabrication

Channels were fabricated in PDMS using a silicon master, and sealed with a glass wafer. We applied a DC voltage along the side-channel, which was filled with a conducting electrolyte and perpendicular to the main channel (see Fig. 3.3). The ionic transport lead to the formation of a current. Therefore, in the presence of a magnetic field, we expect to observe an

MHD-related flow in the main channel.

Experiments

Channel dimensions varied from 50 to 260 µm in depth, and from 50 to 500 µm in width. The length of the side channel set the distance separating the electrodes and was constant, with a value of 8 mm. The length of the main channel varied from 8 mm to 8 cm. Note that standard channels dimensions for all the final experiments were 260 µm in depth, 300 µm in width, and both 8 mm length. DC voltage varied from 0 to 30 V, with a source-limited current of 0.1 A. Current was generated by platinum (Pt) wire electrodes placed in the reservoirs at the entrance of the side-channel. The two electrodes were always separated by a 8 mm long channel. The electrode area, a parameter necessary for current density calculations, is (for this specific geometry) the cross-sectional area of the side-channel, which is 0.08 mm^2. For MHD observations, the magnet was positioned below the channels, in contact with the glass coverplate. The 500 µm thick coverplate fixed the distance between the magnet and the ions in the solution. In case of 260 µm deep channels, the distance between the surface of the magnet and the middle of the channel was 630 µm, leading to a magnetic field intensity of 0.4 T in the microchannel.

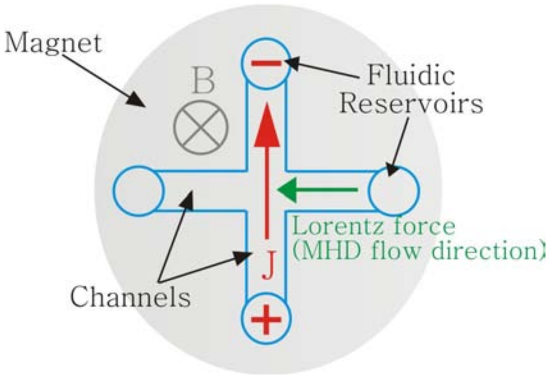

Figure 3.3: Principle of use of the first MHD design

Current generation in the side-channel

We characterized the ohmic behavior of the solution by measuring the current generated across the side-channel as a function of the DC voltage intensity (see Fig. 3.4 for an example). The most stable and high current intensities were obtained for voltages of 20 V. The standard current value was 0.5 mA for 0.1 M KCl and 20 V. This corresponds to a calculated current density of 6410 $A \cdot m^{-2}$ for side-channels with 0.08 mm^2 cross-section.

For saline solutions, we found that the higher the ionic strength, the higher the recorded current for a given voltage. However, at the same time, we observed that the higher the ionic strength, the more bubbles were generated for the same given voltage. We found that saline solutions of 0.1 M had the most stable electrochemical behavior; they achieved the optimum current/voltage quality ratio with minimum gas bubble formation.

MHD observations

The fluorescence microscope pictures in Fig. 3.5 show the movement of polystyrene beads under the influence of electric and magnetic fields. A clear change of the flow profile is observed when the magnetic field was present. The vertical channel in Fig. 3.5 is the side-channel over which the voltage is applied. The horizontal channel is the main channel on which the Lorentz Force should act. Note that no movement in the main channel is observed when only the magnetic field is applied.

The measurement of bead velocity under the influence of MHD was made difficult by the presence of the strong electrokinetic flow in the side-channel. We made visual estimations of bead velocity, that was 0.1 $mm \cdot s^{-1}$ for 0.1 M KCl with $0.3 \times 0.26 \times 8$ mm^3 channels with a current density of 6410 $A \cdot m^{-2}$ ($I = 0.5$ mA).

We calculated the MHD velocity corresponding to our specific experimental conditions and chip geometry with the help of equation 2.16 and the expression of the hydraulic resistance for rectangular channels:

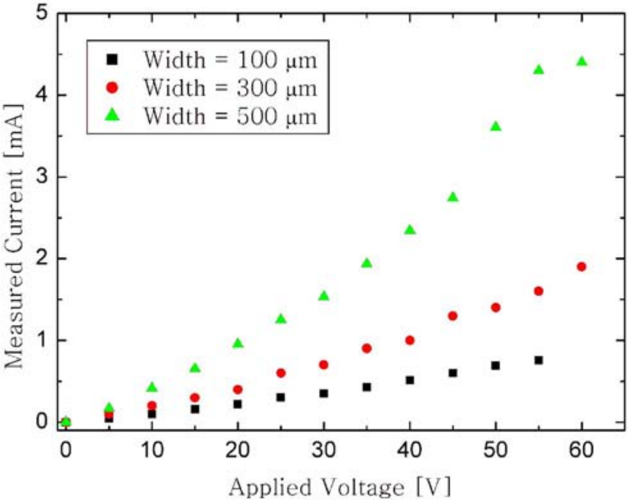

Figure 3.4: Measured current as function of channel width and applied voltage. The channels were 50 μm deep with 1 M NaCl solution.

$$v_{MHD} = J \cdot B \cdot \frac{w^3 h^2}{8\mu L (w+h)^2} \tag{3.1}$$

where w ($= l$) and h are the channel and side channel's width and height, L is the total length of the channel, and μ is the absolute viscosity of the solution in the channel. The calculated MHD speed for such experimental conditions, using Equation 3.1 was 0.2 mm·s^{-1}. We see that the measured MHD velocity is half the calculated one. This is due to a MHD flow perturbation by the strong electrokinetic flow in the side-channel.

The ionic current generates unwanted high and uncontrollable electrokinetic flow from the side channel to the main channel, thereby not allowing a clear visualization of the MHD pumping. Therefore, we designed a new microfluidic device to avoid such unwanted and uncontrollable flows that arise from the side channels.

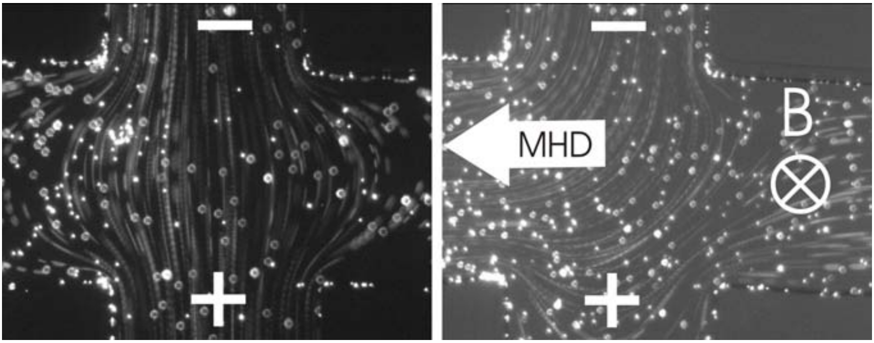

Figure 3.5: (Left) Flow directions in presence of electric field alone. Beads are seen to move from top to bottom, following the electric field lines. (Right) Flow directions in presence of both electric and magnetic fields. Beads are seen to move also from right to left, showing a change in behavior when the magnetic field is added to the electric field.

3.3 PDMS channel on top of platinum electrodes

This second generation of microfluidic devices was designed and fabricated without side channels to avoid the unwanted electrokinetic flow that disturbed the MHD flow in our previous chip.

Fabrication

Top and side views of the device are shown in Fig. 3.6. We used PDMS material for the channels, and we patterned the electrodes directly on the glass wafer that was used for PDMS sealing. We used platinum instead of silver/silver chloride for the micromachined electrodes, as a standard procedure to deposit silver was not available in the cleanroom. We encountered problems aligning the PDMS channels to the electrodes. We observed a change in the dimensions of the PDMS channel (clear decrease) after it was peeled from the silicon master. Only straight channels that were twice as wide (200 µm) as the space between the electrodes (100 µm) could be aligned. Another design with circular electrodes and channels could not be aligned properly due to this change in PDMS dimensions (compared with electrode design) and was thus not evaluated.

Experiments

The channels were 50 µm deep and 200 µm wide. The total length of the channels was 20 mm. The electrodes were made of platinum on top of an adhesion layer of titanium. Electrodes were 100 nm thick, 100 µm wide each, 100 µm apart, for a total length of 20 mm. Since the channel was wider than the space between the electrodes, it left a significant electrode area in contact with the solution on both sides. This area is the product of the mean electrode width inside the channel (50 µm) by the total length of the electrodes (20 mm): that is 1 mm^2. DC voltage varied from 0 to 4 V. Gas bubbles were generated within the channel above 2.5 V. Those bubbles forced the solution out of the microchannel, not allowing higher voltages. As for the first experiment, the DC magnet was placed below the channels in contact with the coverplate. The intensity of the magnetic field in the

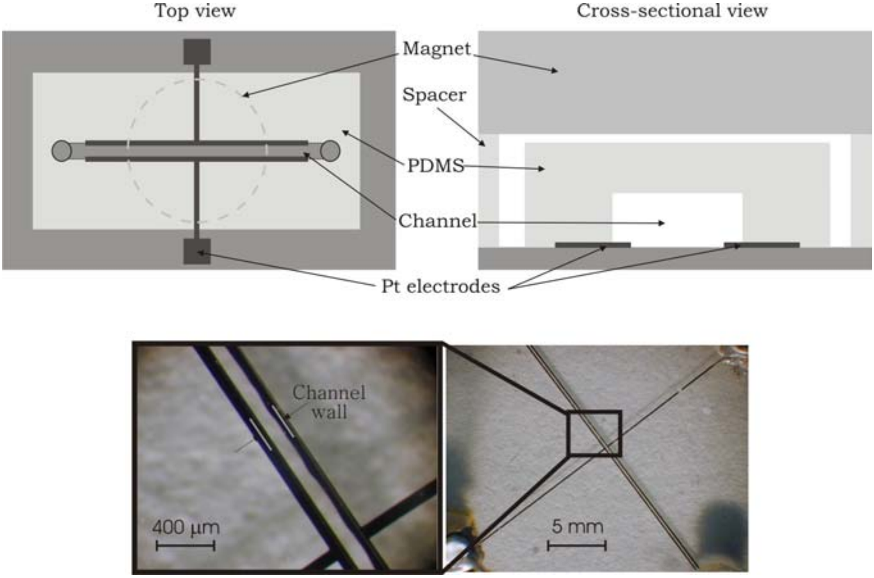

Figure 3.6: (Top) Top and cross-sectional sketches of the PDMS channel on top of the Pt electrodes. (Bottom) Top view of the PDMS channel aligned on the electrodes.

channel was 0.4 T. Solutions of 1 M NaCl and 100 mM NaOH were used for the experiments.

Current generation

We characterized the ohmic behavior of the solutions, by observation of the current generated as a function of the applied DC voltage (see Fig. 3.7). The most stable and high current intensities were obtained for voltages of 2.5V.
The standard current value was 47 μA for 1 M NaCl and 2.5 V. This corresponded to a calculated current density of 47 A·m^{-2}. We measured the current as a function of the chemical composition of the electrolyte inside the channel. The current measured is clearly dependent on the nature of the electrolyte between the electrodes (see Fig. 3.7).

MHD observations

The expected MHD velocity was calculated from Equation 2.16. For such experimental conditions, the MHD velocity follows the relation:

$$v_{MHD} = J \cdot B \cdot \frac{l}{L} \frac{w^2 h^2}{8\mu (w+h)^2} \tag{3.2}$$

where w and h are the channel's width and height (resp.), l and L are the total length of the electrodes and channel (resp.). Using equation 3.2, the expected velocity was calculated to be 3.8 μm·s^{-1} for applied current density of 47 A·m^{-2}, 0.4 T magnetic field, and 1 M NaCl.

We did not observe any MHD-related movement from the first MHD experiments with this chip. No bead movement due to MHD could be observed. This may be from the lack of uniformity in the electrode area, which is due to the difficulty to align the electrodes with the channels.

We designed and fabricated a third device based on the 2nd generation. We integrated the channels and electrodes on the same Pyrex wafer to avoid the alignment problem. Pyrex was chosen as the substrate, because it will be the material needed for the final experiments in the NMR setup.

3.4 Glass channel with electrodes on the inner wall

We used glass as the material for the third device generation. We integrated the electrodes in the channels. Because the current generated is proportional to the electrode surface, we designed a device with a large electrode area (see Fig. 3.8).

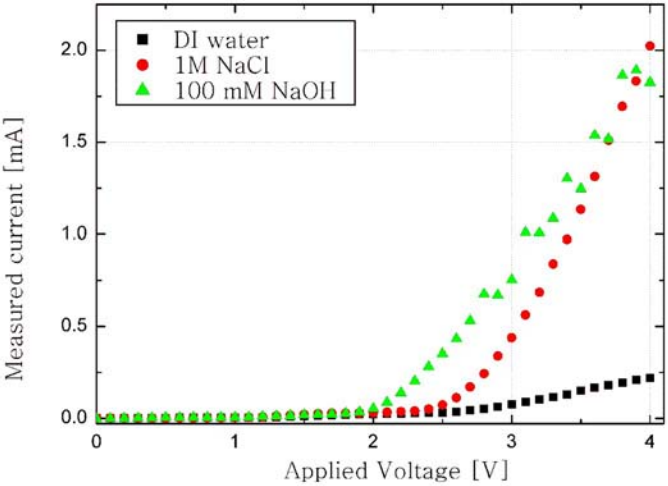

Figure 3.7: Measured current as function of electrolyte nature and applied voltage. In this case, three electrolytes are compared, namely 1 M NaCl, 100 mM NaOH, and DI water.

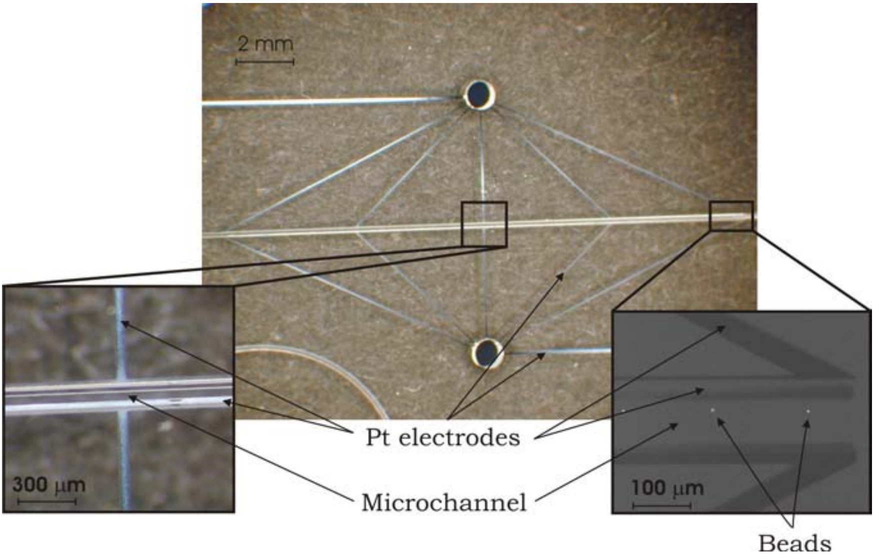

Figure 3.8: Top view of a glass channel with the Pt electrodes on the walls of the channel. The channels presented here are 150 μm wide.

Fabrication

To fabricate this microfluidic device, the channels were first etched in glass. Then the platinum electrodes were deposited on the wall of the channels by a lift-off approach (see Fig. 3.9 for details about the fabrication process).

Experiments

The channels were 75 µm deep. Two channels widths were fabricated, namely 150 and 1000 µm. The total length of the channels were 40 mm and 120 mm. The electrodes were made of platinum (on top of an adhesion layer of titanium), and followed the channel's walls (see Fig. 3.10 for a close-up view of the inside of the channel). Electrodes were 20 mm long, 60 µm wide, and about 80 µm to 1000 µm apart (depending on the width of the channel). Electrode area was 1.2 mm^2. DC voltage varied from 0 to 2V, as gas bubbles were generated after 2 V. As for the other experiments, the DC magnet was placed below the channels in contact with the wafer. The expected intensity of the magnetic field was also around 0.4 T. The electrolyte solution chosen for the experiments was 0.1 M KCl in DI water.

Current generation

The maximum measured current in the channel, before bubble generation, was 10.5 µA for $U_{DC} = 2$ V. This corresponds to a calculated current density of 9 $A \cdot m^{-2}$. This very low value for the generated current intensity is due to polarization effects at the electrode-electrolyte interface. If the voltage applied exceeded a certain threshold, water electrolysis occurred between the electrodes, leading to bubble formation inside the channel.

MHD observations

We calculated the expected MHD velocity with Equation 2.16. For such experimental conditions and chip geometry (half-circular glass channel), the expected MHD velocity follows the relation:

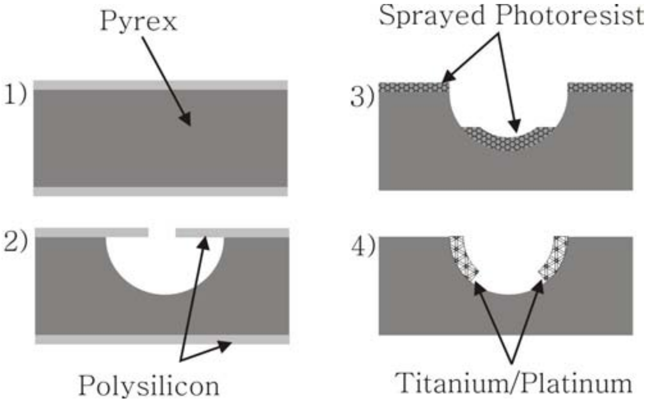

Figure 3.9: Schematic overview of the fabrication of the third generation device: *1)* Start with Pyrex-glass wafer with 400 nm of polysilicon. *2)* Photolithography, RIE etching of polysilicon mask, and deep etching with 20% HF to form the glass channels. *3)* Removal of polysilicon, spray deposition of photoresist, and photolithography using the alignment marks. *4)* Evaporation of metals (200 Å Ti + 1000 Å Pt) on the substrate, followed by lift-off of the metals with acetone and ultra-sound.

$$v_{MHD} = J \cdot B \cdot \frac{l}{L} \frac{3h^2}{64\mu} \tag{3.3}$$

where h is the channel height, l and L are the total length of the electrodes and channel, respectively. With the help of Equation 3.3 for an applied current density of 9 A·m^{-2}, 0.4 T magnetic field, and 0.1 M KCl a maximum flow velocity of 0.5 µm·s^{-1} is expected, which is too low to be observed.

Water electrolysis is an unwanted electrochemical phenomenon. It will deteriorate the electrode surfaces, and the generated bubbles will force the liquid out of the channels. Due to this electrolysis problem, it was not possible to generate a current of sufficient strength to actually observe any flow due to MHD in those channels.

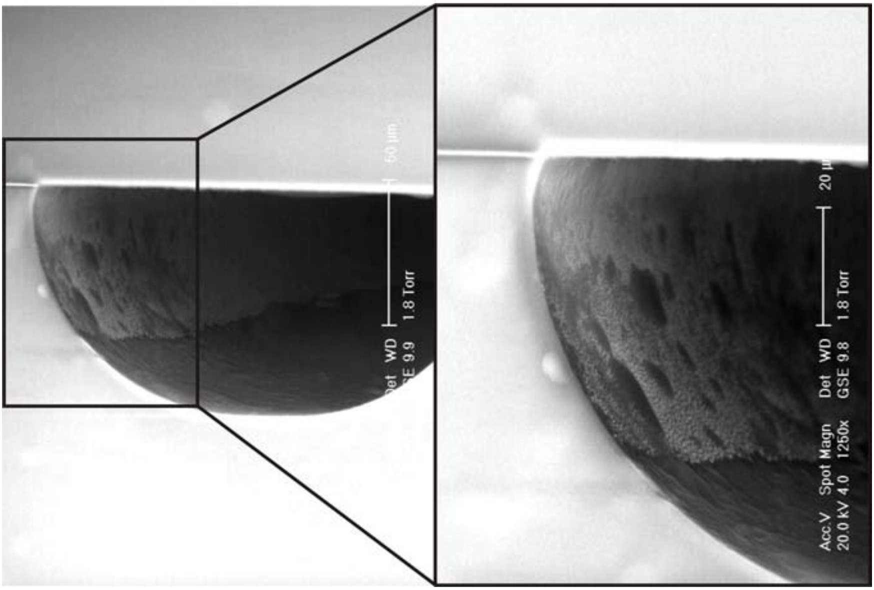

Figure 3.10: eSEM pictures of a channel cross-section

AC Current generation

In order to obtain a better understanding of the device, we switched to AC voltage, which is typically used in electrochemistry to avoid polarization effects and bubble formation. We found that the optimum working frequency was 7-10 kHz (see Fig 3.11).

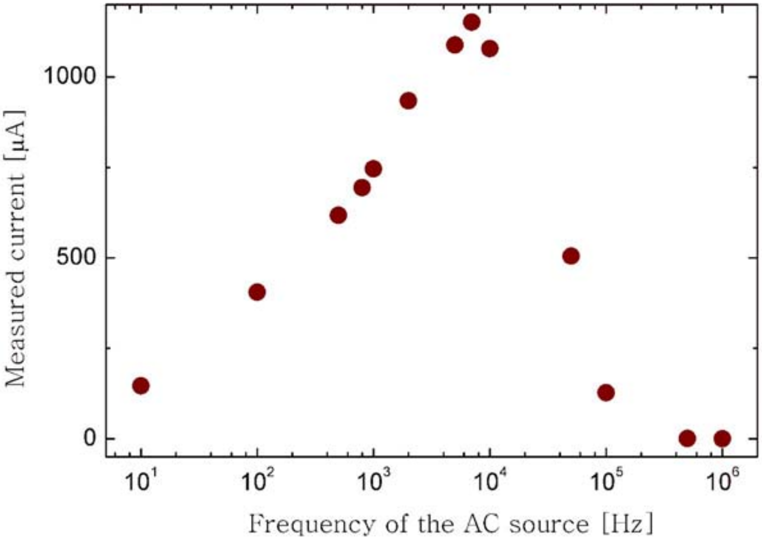

Figure 3.11: Current frequency spectra for an applied RMS voltage of 2 V (0.1 M KCl, 1 mm wide channels).

We could achieve a 150 fold higher current density J_{RMS} = 1333 A·m^{-2} (I_{RMS} = 1.6 mA at U_{RMS} = 2 V and f = 10 kHz) between the electrodes inside the channel compared with the DC mode for the same voltage. The maximum AC current density was 6667 A·m^{-2} (I_{RMS} = 8 mA for 0.1M KCl, U_{RMS} = 14 V and f = 7 kHz). With the help of Equation 3.3, the expected velocities were: v_{MHD} = 70 µm·s^{-1} for applied current density of 1333 A·m^{-2} and v_{MHD} = 0.35 mm·s^{-1} for applied current density of 6667 A·m^{-2} for a 0.4 T

Table 3.1: Comparison of current density and MHD flow velocity for the 3 different designs at maximum voltage and B = 0.4 T (the AC current was measured at f = 10 kHz). The expected body force (ΔP_{MHD}) generated by the pumps was calculated thanks to relation 2.14.

	1^{st} Design	2^{nd} Design	3^{rd} Design	
	DC	DC	DC	AC
Max. Voltage [V]	20	2.5	2	14
Electrode distance [µm]	8000	100	80	80
Electrode area [mm^2]	0.08	1	1.2	1.2
KCl concentration [M]	0.1	1	0.1	0.1
Max. Current [µA]	500	47	10.5	8000
Max. Current density [$A \cdot m^{-2}$]	6410	47	9	6667
Length of electrodes (l) [mm]	0.3	20	20	20
Expected v_{MHD} [$mm \cdot s^{-1}$]	0.2	$4 \cdot 10^{-3}$	$5 \cdot 10^{-4}$	0.35
Measured v_{MHD} [$mm \cdot s^{-1}$]	0.1	*na*	*na*	*na*
Expected ΔP_{MHD} [Pa]	0.8	0.4	0.1	53

magnetic field strength, and 0.1 M KCl electrolyte solution.

We didn't perform MHD pumping experiments in the AC mode, since it was not the final aim of this thesis. But this design is seen to be perfect to achieve AC MHD pumping with microchannels made in glass.

3.5 Summary

This study of MHD pumps with electrodes located in direct contact with the pumping channel has enabled us to have a preliminary understanding of the MHD phenomenon in an electrolyte environment. Table 3.1 shows a comparison of the electrical properties and expected MHD flow velocities for each of them.

Experimental observations of the MHD phenomenon in electrolyte environments was possible only with the first generation of MHD chip (see section 3.2). However, we encountered difficulties to observe a proper MHD pumping in a single managed direction due to the channel geometry (cross intersection). The second and third designs demonstrated the possibility to integrate electrodes with a large area inside the pumping channel, but the threshold voltage before the generation of electrolysis bubbles at the electrode/electrolyte interface limited their applicability. The maximum current density generated by the chips was not sufficient to observe any MHD related flow.

All three studies demonstrated that high current densities (500 $A \cdot m^{-2}$ or more) in the DC mode required voltages greater than 2V, that is above the threshold for electrolysis of aqueous solutions. The following chapter shows how it is possible to generate an MHD flow with voltages leading to electrolysis, but without any perturbation due to electrokinetic flow from the side channel or bubble formation.

Bibliography

[1] D.R. Lide. *C.R.C. Handbook of Chemistry and Physics*. 76th edition, 1995.

[2] R.G. Bates. *determination of pH*. John Wiley and Sons Ltd., 1973.

[3] P.J. Elving, J.M. Markowitz, and I. Rosenthal. Preparation of buffer systems of constant ionic strength. *Analytical Chemistry*, 28:1179–1180, 1956.

[4] T.C. McIlvaine. A buffer solution for colorimetric comparison. *Journal of Biological Chemistry*, 49:183, 1921.

Chapter 4

A high current density DC MHD micropump

This chapter is adapted from:

A high current density DC magnetohydrodynamic (MHD) micropump

Alexandra Homsy, Sander Koster, Jan C.T. Eijkel, Albert van den Berg, F. Lucklum, E. Verpoorte, and Nico F. de Rooij, Lab On a Chip, Volume 5, 2005, pp. 466-471.

A high flow rate DC magnetohydrodynamic (MHD) micropump

Alexandra Homsy, Sander Koster, Jan C.T. Eijkel, Albert van den Berg, E. Verpoorte, and Nico F. de Rooij, Presented at the Micro-TAS 2004 Conference, Malmo, Sweden, Proceedings pp. 372-374, Sept. 26-30, 2004.

This chapter describes the working principle of a DC magnetohydrodynamic (MHD) micropump that can be operated at high DC current densities (J) in 75-µm-deep microfluidic channels without introducing gas bubbles into the pumping channel. The main design feature for current generation is a micromachined frit-like structure that connects the pumping channel to side reservoirs, where platinum electrodes are located. Current densities up to 4000 A·m^{-2} could be obtained without noticeable Joule heating in the system. The pump performance was studied as a function of current density and magnetic field intensity, as well as buffer ionic strength and pH. Bead maximum velocities of up to 1 mm·s^{-1} (0.3 µL·min^{-1}) were observed in buffered solutions using a 0.4 T NdFeB permanent magnet, at an applied current density of 4000 A·m^{-2}. This pump is intended for transport of electrolyte solutions having a relatively high ionic strength (0.5 - 1 M) in a DC magnetic field environment. The MHD micropump presented here is made in glass, and is operated in the DC mode. Gas bubble formation due to DC operation does not influence the performance of the pump since the bubbles are generated outside the pumping channel. This pump is intended to be integrated together with planar NMR coils in a microfluidic system for NMR analysis [1]. Ultimately, the pump will take advantage of the high DC magnetic field (7 T) necessary for NMR analysis to pump and manipulate the fluids in the chip. In the NMR environment, a minimum 16-fold increase in volumetric flow rate for a given applied current density is expected. The application of this pump for the study of biological samples in a miniaturized total analysis system (µTAS) with integrated NMR detection is foreseen.

4.1 New design concept

The first generation of MHD chips (see Section 3.2) enabled the generation of high DC current across electrodes connected by one deep side-channel without introducing gas bubbles in the pumping channel. However, the electrokinetic flow of buffer between the electrodes significantly disturbed the MHD flow itself. All the designs of MHD micropumps presented in the literature (and in previous chapters) have integrated the electrodes di-

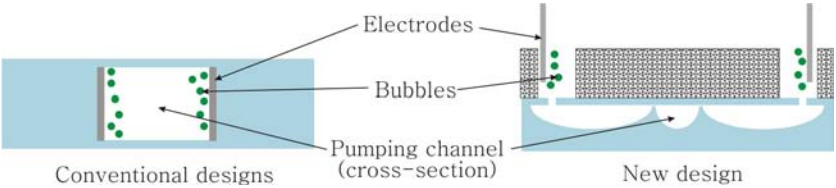

Figure 4.1: Schematic diagram comparing electrode location and chip design for previous MHD pump designs (left) and the new concept (right).

rectly into the pumping channel for current generation. When aqueous solutions are actuated with a DC voltage source, bubble formation around the electrodes (due to water electrolysis) is unavoidable[1]. In order to avoid disruption of flow due to bubble formation in DC operation, we designed two micromachined frit-like structures which connect the pumping channel to adjacent side reservoirs. The electrodes are actually located in these side reservoirs, and are thus physically separated from the main channel in which flow is generated. In this way, bubbles formed at the electrodes never enter the main channel, escaping instead through open reservoirs to the atmosphere. A comparison of the present design concept with that of previously published MHD pumps is shown schematically in Fig. 4.1.

The idea for the adopted design is based on [2], where a similar geometry was used to perform free-flow electrophoresis on silicon chips. A high ionic current with a very low volumetric flow rate can be generated over the main channel across a network of very *shallow* frit-like structures (these will be referred to as "side channels" from now on). When this ionic current is coupled to a perpendicular magnetic field, a body force is generated in the perpendicular direction, all along the pumping channel. With this new design concept, we have been able to generate a current density in the pumping channel that is 50 times higher, in channels with heights 4 times smaller, than that reported by others in closed channels [3].

---

[1] The only solution to avoid bubble generation at the electrode surface in these cases would be to choose an appropriate selection of electrolytes and electrode material (redox species) yielding a non-gaseous product in the electrode reaction.

4.2 Experimental Methods

4.2.1 Micropump fabrication

Pyrex 7740 wafers (Sensor Prep Services Inc.) were used as substrates for the fabrication of the MHD pump. As the MHD flow rate is proportional to the current density (J), the chip was designed to generate a high J across the channel pumping area, without introducing bubbles into the channel. Details of the chip design can be seen in Fig. 4.2. Along both sides of the main channel (22 mm x 150 µm x 75 µm), arrays of 800 perpendicular side channels (10 µm x 10 µm x 100 nm) were etched. These channels connected the main channel to the side-reservoirs (16 mm x 2.5 mm x 75 µm), in which the platinum electrodes were inserted.

Both main channel and side channels are processed on the same Pyrex wafer by a two-step photolithography process in our cleanroom facility. The 75-µm-deep main channel and reservoirs were etched first with 20 % HF, using polysilicon (2 depositions at 2000 Å each) as an etch mask. Then, polysilicon was removed in a 60°C KOH etch bath, and AZ4562 photoresist was sprayed (Airbrush Rotring CH) on top of the wafer. A photolithography mask with the side channel openings was then aligned to the wafer with the help of a mask aligner (Electronic Vision AL6-2, Schaerding, Austria). After UV exposure and development, the photoresist served as an etch mask for the buffered HF etch (BE 7-1 NC1 from Laporte Electronics) performed to obtain the shallow 100-nm-deep side channels. The channels were then sealed by fusion bonding to a Pyrex wafer coverplate with drilled holes to introduce fluids to the main channel and side reservoirs. A piece of 5-mm-thick polydimethylsiloxane (PDMS - Sylgard 184 from Dow Corning, Distrelec AG, Switzerland) was reversibly sealed to the top of the chip to provide the outer liquid reservoirs (see Fig. 4.3). A pair of holes (4 mm diameter) in the PDMS layer was aligned over the microchannel inlet and outlet, and platinum wire electrodes were placed in a wide opening (5 x 5 x 5 mm^3) positioned over the side reservoirs.

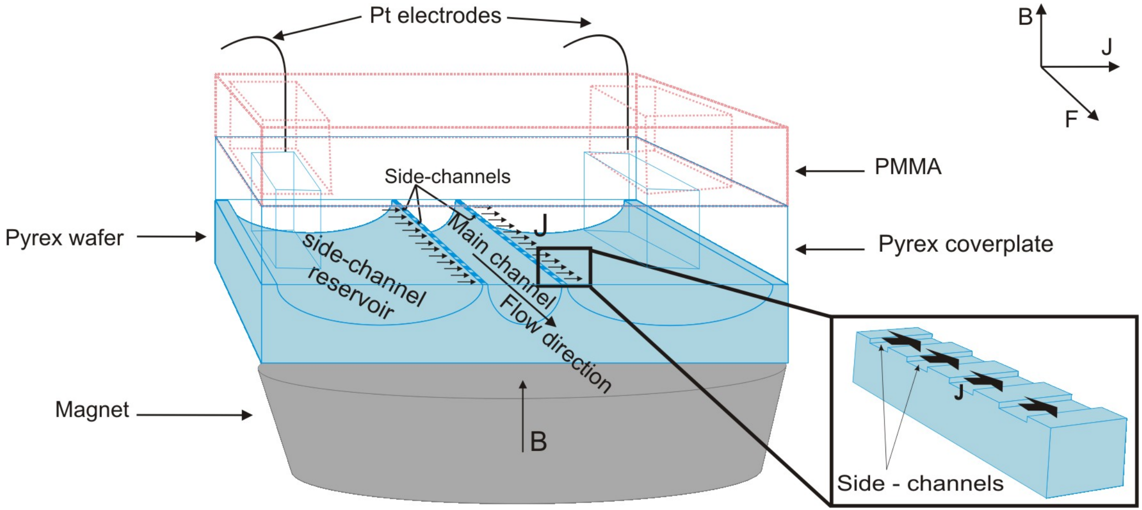

Figure 4.2: Schematic cross-sectional view of the pumping area. The main channel is 22 mm long, 150 µm wide and 75 µm deep. A 16-mm-long segment of the channel was used as the MHD pump. The side channels are 100 nm deep, 10 µm wide and 10 µm long.

4.2.2 Pumping experiments

Citrate-phosphate buffer (53 mM citrate, 207 mM phosphate) with a pH varying from 3 to 7 was chosen for these experiments. KCl was added to the buffer to increase the ionic strength of the solution to fixed values of 0.5 M and 1 M. Fluid velocity was observed using a stereoscopic microscope (Leica MZ12) connected to a digital camera (JVC TK-C1380). A 10× magnification was used. Polystyrene beads (Polysciences, carboxylate-modified microspheres, 2.55% in water) with a diameter of 6 μm were diluted 500 times in the buffer for flow visualization. The linear flow velocity was determined by measuring the time required for beads to travel between two defined points in the pumping channel. Only beads having a maximum velocity (i.e. beads located in the middle of the channel) were considered. The error associated with the measurement was calculated for 10 beads in a total sample of 50 beads per observation. A constant voltage (0 - 60 V) was applied across two platinum electrodes by a DC power supply (HP E3617A). A multimeter (Keithley 175) was used to monitor the current. All measurements were performed under conditions of constant current, which ranged between 0.6 mA and 5 mA, depending on the experiment. A NdFeB rare earth permanent magnet (Forcefield, USA) was placed under the device. Three magnets, having three different magnetic field intensities (namely 0.22, 0.32 and 0.42 T) were used during the measurements. The dimensions of the magnets (50 mm diameter) were larger than the outer dimensions of the chip. The magnet was placed so that it was almost in contact with the chip, in order to assure good homogeneity of the magnetic field in the channel. The magnetic field intensities were measured with a 3-axis magnetic-field transducer (model 3MR-1C, Sentron AG Switzerland).

4.3 Results and discussion

The MHD device presented in Fig. 4.3 has a total of 4 reservoirs. Two are the side reservoirs, where the Pt electrodes were positioned. The two other reservoirs, perpendicular to the sidechannel reservoirs, were connected to the inlet and outlet of the main channel where the pumping was induced.

Filling of the device with buffer began by filling the main channel, followed by the side reservoirs. The side channels were filled automatically by capillary action when liquid was introduced to the main channel. No problems related to the trapping of air bubbles were encountered when side channels were filled. For flow visualization, the main channel was filled with the buffer containing 6 µm polystyrene beads.

When the DC voltage was applied between the platinum electrodes, a net electric current in the mA range was measured, increasing linearly with the voltage. We used a buffered solution to avoid large pH changes around the electrodes. Gas bubbles that formed around the platinum elec-

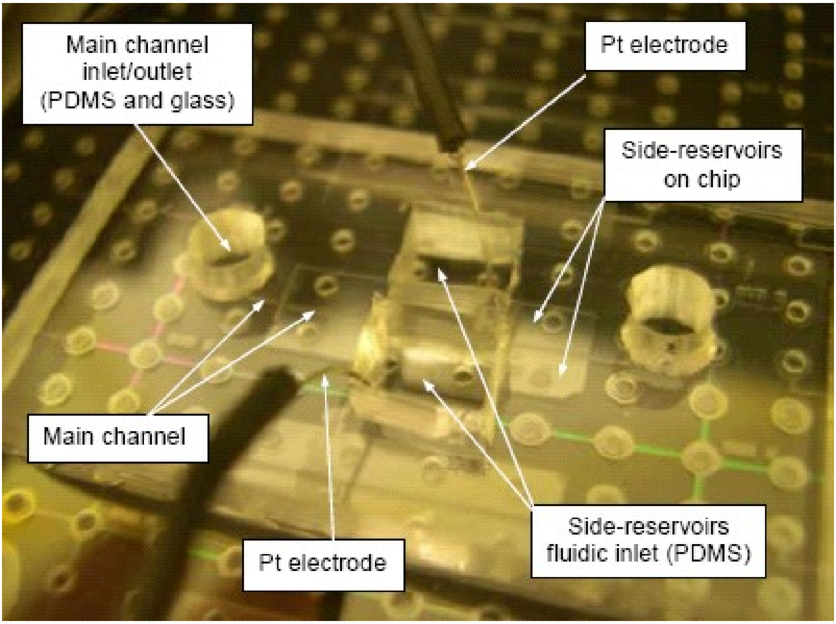

Figure 4.3: View of the chip with PDMS on top for the inlet/outlet reservoirs as well as electrode reservoirs. The Pyrex coverplate bonded on top of the processed wafer contains a standard grid of holes for generic use in microdevice fabrication. In our case, chip operation relies on only 10 of these holes.

trodes could easily escape through the large holes in the PDMS. Gas bubbles were never seen entering the side reservoirs (and therefore the side channels). Bead movement was not observed when only an electrical field or a magnetic field was applied at a buffer ionic strength between 0.5 and 1 M. However, when the current was applied across the channel together with a perpendicularly applied magnetic field, beads began to move above a current density threshold of 500 A$\cdot$m^{-2} (corresponding to a voltage $\geq$ 3.5 V). Beads located in the center of the channel were seen to move faster than the beads on the sides close to the channel walls, which is typical behavior for flows with a parabolic profile. Fig. 4.4 shows the maximum bead velocity in the main channel as a function of J for 3 different magnetic field intensities. The bead velocity was seen to increase with B. Measurements with more values of B would be needed to confirm the linear behavior with increasing B. This observation is of interest, as we intend to integrate this pumping method into a chip for integrated NMR analysis using a 7 T magnet [1]. The expected velocity at 7 T is therefore also shown in Fig. 4.4. Assuming that flow velocity varies linearly with B (as predicted by Equ. 2.16), we expect a minimum 16-fold increase in bead velocity for a given current density value in a 7 T NMR environment. In other words, much lower actuation voltage would be required to obtain a given velocity.

The bead velocity was also seen to increase with J. Maximum observed velocities were 1 mm$\cdot$s^{-1} for a magnetic field intensity of 0.42 T and a current density of 4000 A$\cdot$m^{-2}. Measured velocities were on the same order of magnitude as theory. However, measured velocities were less than expected from theory for low J values, while in the higher current density range, beads exhibited velocities higher than theory. The main sources for these deviations are believed to come from the back flow induced by hydrostatic pressure (at low J), and Joule heating (at high J). The relative contributions from these effects will depend on the total pressure induced by MHD and on the power dissipation capability of the chip.

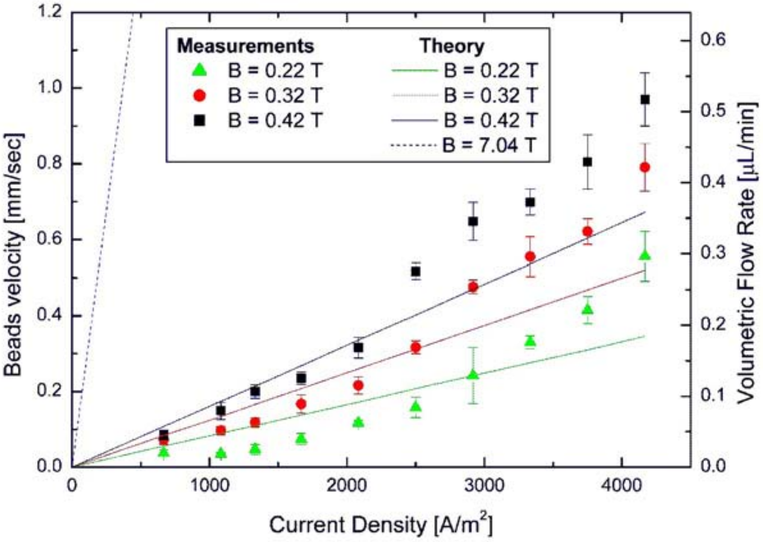

Figure 4.4: Maximum velocity of 6 μm carboxylate-modified polystyrene beads as a function of applied current density for 3 different magnetic field intensities in a citrate phosphate buffer of pH = 5 (207 mM Phosphate, 53 mM Citrate), with 744 mM KCl added to increase the ionic strength of the buffer. Error bars indicate the standard deviation for 10 beads of maximum velocity in a total sample of 50 beads per measurement. The theoretical curves were calculated using Equation 2.16.

4.3.1 Flow limitation due to back pressure

Equation 2.14 describes the theoretical pressure generated by MHD. A flow in the direction opposite to MHD was often observed when measurements were stopped. Back pressure resulting from this flow will depend on the total measurement time, as this determines the total liquid volume transported from one reservoir to the other. Height differences of liquid between inlet and outlet reservoirs can result when significant amounts of liquid have been pumped, with more liquid in the outlet reservoir than in the inlet reservoir. This can result in a hydrostatic pressure difference, or back pressure, acting against the MHD flow. The back pressure was measured at the end of each MHD experiment by observing the velocity of the beads traveling in the opposite direction after a total measurement time, t. The pressure of the backflow was estimated with the help of Equations 2.10, 2.14 and 2.12.

It is obvious that a more accurate method to determine the back pressure would involve integration of a pressure sensor into the chip. As velocities are additive, the measured bead velocity will be the velocity induced by MHD minus the velocity gradually induced by the back pressure. In terms of pressure, the total measured pressure (ΔP_{TOT}) will be equal to the pressure induced only by MHD (ΔP_{MHD}) minus the back pressure (ΔP_{BAK}):

$$\Delta P_{TOT} = \Delta P_{MHD} - \Delta P_{BAK} \tag{4.1}$$

Table 4.1 compares the back pressure with the measured pressure, and the pressure expected from MHD pumping (for a 1 M buffer solution of pH = 5, and magnet field strength of 0.4 T). It can be concluded that back pressure plays a significant role in the total pressure of the system (up to 22% of total measured pressure in this specific case), but it is not large enough to stop MHD flow under a reasonable total measurement time.

4.3.2 Joule heating and power dissipation

At high current densities, the flow velocity was observed to be higher than that calculated. One explanation is that the temperature in the main channel began to rise because of Joule heating occurring in the side channel area.

Table 4.1: Comparison of the pressure generated and of the calculated power dissipation Q_d in the pump as a function of applied current density. Each measurement was performed for a time, t. The pumped solution was a 1 M citrate-phosphate buffer of pH = 5; magnetic field intensity of 0.4 T.

U (V)	J ($A\cdot m^{-2}$)	t (min)	ΔP_{TOT} (Pa)	ΔP_{BAK} (Pa)	ΔP_{MHD} (Pa)	$\Delta P_{\mathrm{MHD\ THEO}}$ (Pa)	Q_d ($W\cdot m^{-1}$)
5	494	28	5	0	5	3	0.1
10	1725	25	8	1	9	11	1.0
15	2549	21	15	3	19	16	2.5
20	3620	10	28	1	29	23	4.9

Above a certain threshold, the temperature will decrease the viscosity of the pumped solution, leading to an increase in flow velocity. Figure 4.5 shows the Ohm plot measured under conditions corresponding to the measurements of Fig. 4.4. The current density begins to deviate from linearity after 2500 $A\cdot m^{-2}$. This shows that Joule heating may affect our measurements of MHD bead velocities above this current density threshold for an applied voltage of 12 V with such a buffer solution. The last column of Table 4.1 shows the power dissipation (Q_d) along the side channels arrays for the same experimental conditions as in Fig. 4.4.

Power dissipation is widely used as an indicator for temperature increases due to Joule heating (see section 2.3.1) in discussions about efficiency in electrophoresis separations [4]. Applied to our specific geometry, this indicator is estimated as follows:

$$Q_d = \frac{(U-2)\cdot I}{l_{cap}} \tag{4.2}$$

where l_{cap} is the total length of the side channels[2] [m], U is the voltage ap-

---

[2] This value is the sum of the lengths (10 μm) of all the 800 sidechannels located on both sides of the main channel.

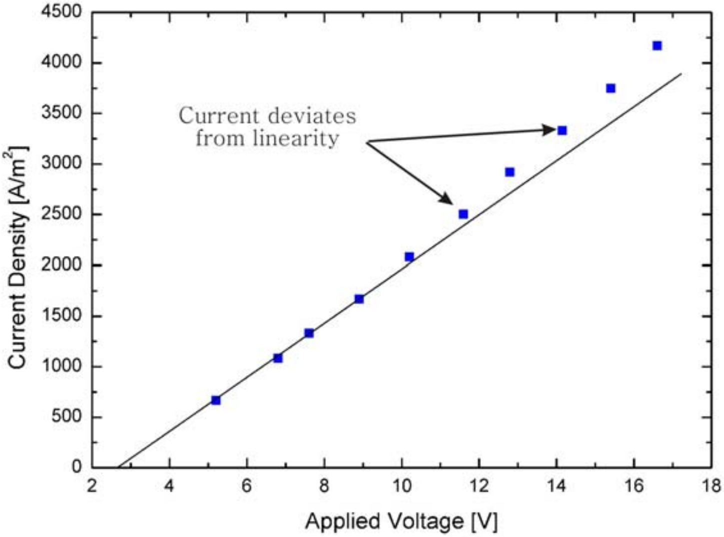

Figure 4.5: Current-Voltage behavior of the chip during the velocity experiments depicted in Fig. 4.4.

plied across the system [V], and I is the current [A] across the side channels. In microfluidic systems, Joule heating was observed to occur for Q_d values [5] larger than 3 W·m^{-1} (instead of 1 W·m^{-1} for standard capillaries). With our specific geometry, the power dissipation threshold corresponding to the beginning of Joule heating is seen at 2.5 W·m^{-1}. This threshold is reached if the applied voltage is higher than 12 V in 1 M buffer solutions.

4.3.3 MHD flow dependence on buffer ionic strength and pH

Table 4.2 shows values of the measured maximum bead velocities at a mid-range current density for various pH and ionic strengths of the buffer. The last column of the table shows the theoretical maximum velocity (calculated from Equation 2.16) for the corresponding experimental parameters. A strong dependence of bead velocity on both current density and magnetic flux density is observed for all buffer conditions. Comparing values at a fixed ionic strength but different B shows in fact that there is very little, if any, variation of bead velocity as a function of pH at a given ionic strength and B. The beads used for the velocity measurements were carboxylate-coated. The pKa of carboxyl groups has a mean value of 4.9 [6]. The beads which gave the most reproducible measurements were the ones handled at pH $\leq$ pKa. By comparing the theoretical and measured velocity values, we see that the results are of the same order of magnitude, and follow the same main variations as a function of the magnetic field.

At lower ionic strengths (0.01 - 0.1 M), a flow in the J direction was observed, adversely affecting MHD flow in the main channel. This flow is most likely electro-osmosis, originating in the side channel arrays[3]. Efforts are currently focusing on improvement of the chip design and implementation of surface chemistry to reduce electro-osmotic flow, in order to decrease these effects. Once the issue of unwanted electroosmotic flow has been addressed, our MHD pump (in contrast with electroosmotic pumps) will be suitable for use with solutions of relatively high ionic strengths ($\geq$

---

[3] Those effects lead to a non wanted high volumetric flow across the side channels, which stops the MHD flow in the perpendicular direction.

Table 4.2: Comparison between theoretical maximum MHD flow velocity and measured maximum bead velocities (mm$\cdot$s^{-1}). For a current density of 2083 A $\cdot$m^{-2}, and citrate phosphate buffer with KCl added for fixed ionic strength

Ionic Strength 0.5 M	Observed velocity pH=3	Observed velocity pH=5	Calculated velocity
0.22T	0.20±0.01	0.19±0.01	0.17
0.42T	0.28±0.02	0.33±0.02	0.34

Ionic Strength 1 M	Obs. velocity pH=3	Obs. velocity pH=5	Obs. velocity pH=7	Calculated velocity
0.22T	0.10±0.02	0.12±0.01	0.12±0.02	0.17
0.32T	0.20±0.02	0.22±0.02	0.22±0.01	0.26
0.42T	0.31±0.02	0.32±0.03	0.28±0.01	0.34

0.1 M). This could prove advantageous for physiological applications requiring higher buffer concentrations.

4.4 Conclusion

We have demonstrated a novel concept for a DC MHD micropump that allows pumping with a maximum velocity of up to 1 mm$\cdot$s^{-1} (0.3 µl$\cdot$min^{-1}) in 75-µm-deep glass microchannels with a 0.42 T permanent magnet. The chip design permitted the use of DC current without gas bubble perturbation in the pumping channel, by using a micromachined frit-like structure to provide electrical contact between the main channel and side reservoirs, where the electrodes were located. Future work with these devices will include a study of MHD flow in the high DC magnetic field of the NMR instrumentation, and its integration into a µTAS for on-chip NMR analysis. Such a µTAS will enable online monitoring of chemical reactions, and analysis of biomolecules in aqueous phase.

Bibliography

[1] C. Massin, F. Vincent, A. Homsy, K. Ehrmann, G. Boero, P.-A. Besse, A. Daridon, E. Verpoorte, N.F. de Rooij, and R.S. Popovic. Planar microcoil-based microfluidic NMR probes. *Journal of Magnetic Resonance*, 164:242–255, 2003.

[2] D.E. Raymond, A. Manz, and H.M. Widmer. Continuous sample pretreatment using a free-flow electrophoresis device integrated onto a silicon chip. *Analytical Chemistry*, 66:2858–2865, 1994.

[3] J. Jang and S.S. Lee. Theoretical and experimental study of MHD magnetohydrodynamic micropump. *Sensors and Actuators A*, 80:84–89, 2000.

[4] R.J. Nelson, A. Paulus, A.S. Cohen, A. Guttman, and B.L. Karger. Use of Peltier thermoelectric devices to control column temperature in high-performance capillary electrophoresis. *Journal of Chromatography*, 480:111–127, 1989.

[5] A.M. Garcýa Campana, W.R.G. Baeyens, H.Y. Aboul-Enein, and X. Zhang. Miniaturization of capillary electrophoresis systems using micromachining techniques. *Journal of Microcolumn Separations*, 10(4):339–355, 1998.

[6] S.H. Behrens and D.V. Grier. The charge of glass and silica surfaces. *Journal of Chemical Physics*, 115(14):6716, 2001.

Chapter 5

Electrical description of the pump

This chapter, complementary to Chapter 4, will present an electrical model specific to our pump geometry. As we used charged beads for flow velocity measurements, both beads and ions in the solutions were subjected to MHD, electroosmosis (eo) and electrophoresis (ep). Eo and ep give rise to a flow perpendicular to MHD. The understanding of all the electrical field processes is important for the interpretation of our flow observations. The model we present in this chapter will help us predict and quantify the effect of the transverse electrokinetic flow. These secondary flows may be the cause for the perturbation of MHD pumping at low ionic strength and even for the loss of sample species from the main channel.

5.1 Model description

We used a simple resistor model to explain the electrical behavior of our pump. When a voltage is applied along a channel filled with a fluid, the electrical resistance is by definition:

$$R = \varrho \cdot \frac{d}{A} \tag{5.1}$$

where ϱ is the measured resistivity of the solution [$\Omega \cdot$m], d is the length of the channel [m] with a cross-sectional area A [m^2]. Figure 5.1 shows the equivalent electrical scheme of the pump. Assuming that this equivalent scheme is an approximation, we can use it to describe the impedance of the pump at low and higher DC voltages. At low voltages (i.e. in the mV range) the electrical behavior of the pump is capacitive (with a capacitance C_{dl}) whereas at higher voltages it is faradic. The high DC current generation condition for the pump involves application of voltages higher than 5 V. In this range[1], the electrical behavior of the pump will always be resistive. If we apply the well-known Kirchhoff rules associated with Ohm's law to our circuit, the total voltage U applied to the system will be:

$$\begin{aligned} U &= U_i - U_f = U_i \quad (\text{if } \mathrm{U}_f = 0) \\ &= \Delta U_{cha} + 2\Delta U_{res} + 2\Delta U_{sid} \\ &= R_{tot} \cdot I \end{aligned} \tag{5.2}$$

where:

$$R_{tot} = R_{cha} + 2R_{res} + 2R_{sid} \tag{5.3}$$

R_{sid} is the total electrical resistance of the side-channels in parallel, and if we have n side channels of same resistance R_i:

$$\frac{1}{R_{sid}} = \sum_{i=1}^{n} \frac{1}{R_i} = \frac{n}{R_i} \tag{5.4}$$

The current density J across an area A_J is related to the current:

$$J = \frac{I}{A_J} \tag{5.5}$$

The above expressions allow us to define the desired geometric parameters of the pump such as the total number of side-channels as well as their length and width. The MHD flow rate is directly proportional to J in the main channel. The value for J generated in the main channel should be as high

---

[1] An obvious second condition is the absence of Joule heating (see sections 2.3.1 and 4.3.2)

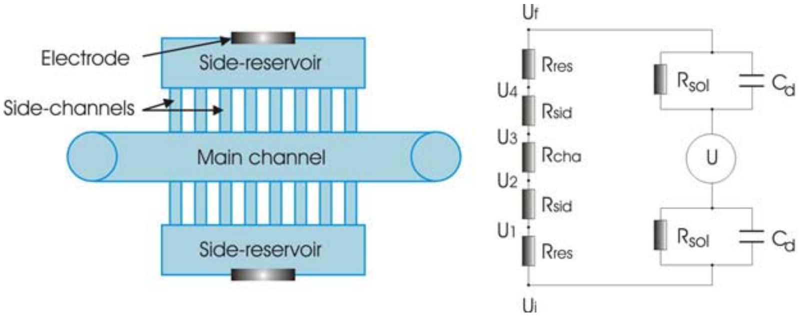

Figure 5.1: Schematic top view of the pump and equivalent electrical scheme. Each channel geometry has a different electrical resistance: R_{res} is the resistance of the side-reservoir area, R_{cha} is the resistance of the main channel, and R_{sid} is the resistance of all side-channels in parallel in between one side-reservoir and the main channel. The electrical resistance of the buffer R_{sol} in parallel with the capacitance C_{dl} represents the electrodes. C_{dl}, the double layer capacitance, stands for the polarization of the electrodes at the electrode-electrolyte interface.

as possible with a corresponding voltage as low as possible. Since the intent of the side channels is to have a very high hydraulic resistance, the depth is fixed to be as shallow as possible (100 nm). With such a small depth, about 98% of the applied voltage will drop on both sides of the pumping channel, at the location of the side-channels. With the parameters of our pump geometry, the electrical resistance of one array of side-channels is expressed as follows:

$$R_{sid} = \frac{R_i}{n} = \frac{\varrho}{n} \cdot \frac{d_s}{h_s\, w_s} \tag{5.6}$$

where d_s (10 µm) is the length, w_s (10 µm) is the width, and h_s (100 nm) is the depth of the n (800) side-channels. The main channel has a depth h (75 µm), a width d (150 µm), and a length l (1.6 cm, along which the current is applied).

$$R_{cha} = \varrho \cdot \frac{d}{h\, l} \tag{5.7}$$

$$\frac{R_{sid}}{R_{cha}} = \frac{d_s}{n\, h_s\, w_s} \cdot \frac{h\, l}{d} = 100 \tag{5.8}$$

We see that the electrical resistance of the array of side channels is 100 times higher than of the main channel, this confirms that the majority of the voltage will drop over the array of side-channels.

Electric field

Another important parameter in our system is the intensity of the electric field at various locations in the pump. Obviously, E across the side-channels is much higher than in the main channel. A large E value would be a problem for MHD flow, as it would induce perpendicular flows through electrokinetics (see section 2.3.2).

The electric field across the main channel (E_{cha}) is expressed as:

$$E_{cha} = \frac{\Delta U}{d} = \frac{U_3 - U_2}{d} = \frac{R_{cha} \cdot I}{d} = \frac{\varrho}{h \cdot l} \cdot I \tag{5.9}$$

The electric field across one array of side-channels (E_{sid}) is:

$$E_{sid} = \frac{U_2 - U_1}{d_s} = \frac{R_s\, I}{d_s} = \frac{\varrho}{n} \cdot \frac{I}{h_s\, w_s} \tag{5.10}$$

To compare E_{sid} with E_{cha}, we take the ratio of the two expressions as a function of I:

$$\frac{E_{sid}}{E_{cha}} = \frac{h\, l}{n\, h_s\, w_s} \tag{5.11}$$

And applied to our specific pump geometry,

$$\frac{E_{sid}}{E_{cha}} = \frac{75 \cdot 10^{-6} \cdot 1.6 \cdot 10^{-2}}{800 \cdot 100 \cdot 10^{-9} \cdot 10 \cdot 10^{-6}} = 1500 \tag{5.12}$$

We notice that the electric field in the side channels is 1500 times more intense than the one in the main channel.

Electrokinetic flows

The effects of an applied electric field on a fluid are described in paragraph 2.3.2. It is important to note that electrokinetic (ek) flows are proportional to the electric field despite the geometry of the microchannel (ie. the depth of side channels). This means that above a certain eof velocity threshold, the MHD flow in the pumping channel is likely to be perturbed by the perpendicular ek flows originating from the side channels. The ek flows that perturb MHD pumping are the ones generated by the electric field in the main channel (E_{cha}).

The expression for the MHD velocity is compared with the bulk ek flow velocity of eof. We first express equation 2.16 as a function of our specific geometry, and then replace J by 2.24 to extract the dependence on E_{cha}.

$$v_{MHD} = \frac{3\, h^2}{64\, \mu}\, \frac{l}{L}\, J \cdot B = \frac{3\, h^2}{64\, \mu}\, \frac{l}{L}\, \frac{B}{\varrho}\, E_{cha} \tag{5.13}$$

The viscosity μ and electric field E_{cha} were eliminated by expressing the ratio of v_{MHD} over the eo flow velocity expressed in chapter 2.3.2:

$$\frac{v_{MHD}}{v_{eo}} = \frac{3\,h^2}{64}\,\frac{l}{L}\,\frac{B}{\varrho}\,\frac{1}{\varepsilon\,\zeta} \tag{5.14}$$

The ratio $\frac{v_{MHD}}{v_{eo}}$ is inversely proportional to ζ and ϱ. The zeta potential [1, 2] should therefore be minimized in order to avoid perturbations of MHD flow due to eof. High ionic strength solutions, having smaller resistivity are also likely to allow the ratio to be higher.

5.2 Resistance measurements

The voltage - current measurements of the pump for 3 different buffer ionic strengths are shown in Fig. 5.2. Each of the three plots show both linear and non-linear parts. The boundary between the linear and the non-linear part depends on the ionic strength of the buffer. In the particular case of figure 5.2, the voltage threshold between both parts will be 35 V for 0.25 M, 17 V for 0.5 M, and 12 V for 1 M ionic strengths. Note that Ohm's law is applicable to the linear part. However, above a certain current-voltage threshold, a non-linear behavior is observed which is probably caused by a decreasing electrical resistance due to Joule heating.

The measured electrical resistances of the pump filled with buffer of different ionic strengths are compared in Table 5.1. The two last columns compare the calculated total electrical resistance of the pump and the measurements. The resistance for an applied voltage around 10 V was measured, and this was still in the linear part of the current-voltage plot of the pump. The ratio of calculated vs. measured electrical resistances of the system is about the same for all three ionic strengths and equals 1.4. Our electrical model of the pump gives us an estimation of the total electrical resistance that is 50% less than what was measured. This is most likely due to imperfections of the resultant side-channels geometry after the microfabrication steps.

Above the ohmic behavior threshold, which is different for each ionic strength, the measured resistance diminishes with increasing voltage. This

Table 5.1: Comparison of the electrical resistance measured for 3 different buffer ionic strengths with the one calculated from our model (R_{calc}, Equ. 5.7). The pumped solution was a citrate-phosphate buffer of pH = 5, the applied voltage is around 10 V.

	U [V]	I [mA]	R_{mes} [kΩ]	R_{calc} [kΩ]	$\frac{R_{mes}}{R_{calc}}$
0.25 M	10	0.2	52.9	35.9	1.5
0.5 M	10.3	1.3	7.9	6.4	1.2
1 M	10.9	2.5	4.4	3.2	1.4

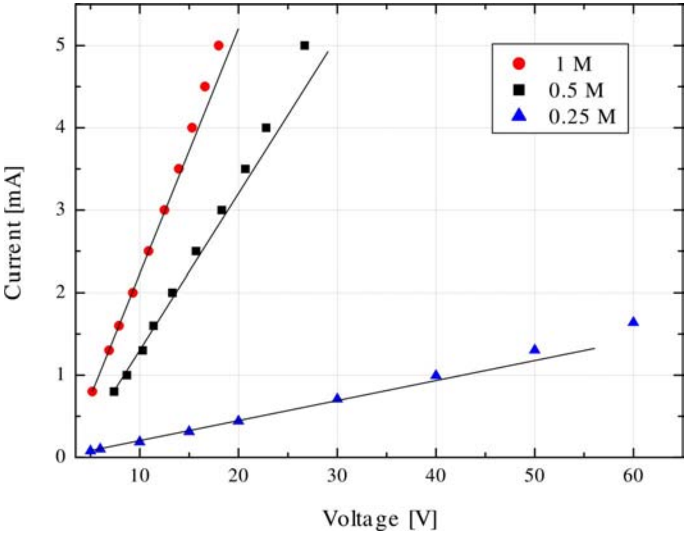

Figure 5.2: Measured current as function of citrate-phosphate buffers ionic strength and applied voltage for the new pump. The straight lines are linear fits. (pH = 5, KCl was added for increased ionic strength to 0.5 and 1 M)

phenomenon happens in our pump for voltages higher than 12 V under all experimental conditions investigated in this work, and is related to Joule heating.

5.3 Flow observations

We used carboxylate coated latex beads in a citrate - phosphate buffer solution of pH = 5 (see section 4.2.2) to observe the flow in the main channel. The pump showed two distinct behaviors when *voltage only* was applied across the main channel, depending on the ionic strength of the buffer. At *low ionic strength* (i.e. 0.25 M or less) the beads were seen to be stacked against the side-channel walls. This bead migration against the side channel wall was noticed when only DC voltage was applied. The electrokinetic flow across the side channels seemed to be high enough to perturb our pump, as no bead flow due to MHD was observed in the main channel when the additional magnetic field was applied. At *high ionic strength* (i.e. 0.5 M or more) no flow perpendicular to the main channel direction was noticed when only a DC voltage was applied. When *B* was added, MHD pumping of beads was observed along the main channel.

Low ionic strength

We performed only few measurements with low ionic strength citrate-phosphate buffers ($I_{str} \leq 0.25$ M). Under those conditions, MHD observation experiments were not possible. In order to analyze this problem, we measured the current for a given voltage (Fig. 5.2), as well as conductivity of the buffer. As discussed in the preceding section, this perturbation is believed to be caused by ek flows.

The expected velocity for MHD and corresponding perpendicular electroosmotic flow velocity were calculated and compared for a buffer of pH = 5 under the influence of an applied voltage of 10 V (I = 0.19 mA) and a magnetic field of 0.4 T. The current density in the main channel will be:

$$J = \frac{I}{h\,l} = 167\ \mathrm{A} \cdot \mathrm{m}^{-1} \tag{5.15}$$

MHD velocity in a half-circular channel:

$$v_{MHD} = \frac{3\,h^2}{64\,\mu}\,\frac{l}{L}\,J \cdot B = 13.4\ \mu\mathrm{m} \cdot \mathrm{s}^{-1} \tag{5.16}$$

where L (22 mm) is the total length of the main channel, and μ ($1.1 \cdot 10^{-3}$ [Pa·s]) is the absolute viscosity of the buffer. Electric field in the main channel:

$$E_{cha} = \frac{\varrho}{h\,l} \cdot I = 204\ \ \mathrm{V} \cdot \mathrm{m}^{-1} \tag{5.17}$$

The glass channel walls in a 0.25 M buffer environment have an estimated zeta potential of 20 mV [1–3]. The ratio of MHD to eo velocity is therefore:

$$\frac{v_{MHD}}{v_{eo}} = \frac{3\,h^2}{64}\,\frac{l}{L}\,\frac{B}{\varrho}\,\frac{1}{\varepsilon\,\zeta} = 5 \tag{5.18}$$

In a 0.25 M buffer, the eof flow velocity will be 5 times less than MHD. We see that the expected electrokinetic flow velocity is very close to the one from MHD. Those calculations are summarized in Table 5.2. The eo flow under such conditions is believed to be so high that it prevented the observation of MHD flow with our bead technique.

High ionic strength

At high ionic strength we observed MHD flow in the main channel, and we did not notice any perturbation from the side channels. In order to complete our understanding of the electrokinetic phenomena, we compared the expected MHD flow velocities with the eo velocity for every ionic strength of our buffer in Table 5.2. Under high ionic strength conditions, we noticed that MHD flow is at least 28 times faster than eo flow.

Table 5.2: Comparison of calculated eof and MHD flow velocities in the main channel for an applied voltage of 10 V and 0.42 T magnet strength. The pumped solution was a citrate-phosphate buffer of pH = 5.

	ϱ ($\Omega\cdot$m)	I (mA)	J_{main} ($A\cdot m^{-2}$)	v_{MHD} ($\mu m\cdot s^{-1}$)	E_{main} ($V\cdot m^{-1}$)	v_{eof} ($\mu m\cdot s^{-1}$)	$\frac{v_{MHD}}{v_{eof}}$
0.25 M	1.2	0.2	167	13.4	204	2.6	5
0.5 M	0.2	1.3	1083	87.3	238	3.0	28
1 M	0.1	2.5	2083	167.8	229	2.9	55

Influence of transverse electrokinetic flows

In the preceding sections we noticed that the flow originating from eo was on the same order of magnitude as MHD. At low ionic strength, under the influence of an electric current, the beads were pulled against the side-channel wall. At high ionic strength, this behavior was not observed when only current was applied. Under MHD flow measurements (at high ionic strength) a proportion of flowing beads stopped their course on the side channel walls. The beads, which are negatively charged (carboxy groups), were always seen to be attracted to the side-channels wall on the same side as the anode, the positive electrode. By labeling the buffer flowing in the main channel with amaranth (a red dye, see section 6.1.2), we also observed that the color of the transparent buffer in the side reservoirs (anode side) began to turn red at the entrance of the side channels within a few minutes. Since amaranth has a negative charge it also moved towards the anode. Electroosmotic flow is a bulk flow, and is directed towards the cathode in glass channels. This observed movement of beads and amaranth towards the anode is due to the ep mobility of the beads (or dye) being much larger than eo flow across the side channels.

We believe that our MHD observations were always the superimposition of electrokinetic flows (eo+ ep) together with MHD (see Fig. 5.3). At low ionic strength (when MHD $\approx$ eo + ep) the addition of the three vectors lead to a velocity vector following the direction of the side channels. At high

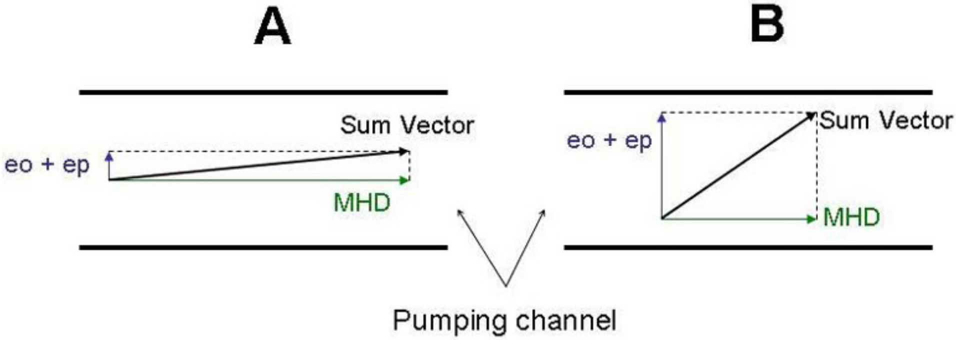

Figure 5.3: Vectors representing eo, ep and MHD movement and their sum vector for the cases that: A) MHD $\gg$ (ep + eo) B) MHD $\approx$ (ep + eo).

ionic strength MHD velocity will be high enough for the vector sum to be in the pumping direction. As an example, if we compare our calculations of velocities at low ionic strength (0.25 M), we see that eo flow is similar in magnitude to MHD (only 5 times lower than MHD). No specific experiments were conducted to determine what is the concentration threshold at which MHD pumping is less perturbed by ek flows. But in order to get rid of eo completely, one could think of treating the surface of the channels with an uncharged molecule (a sugar molecule for example) as uncharged molecules should drop the zeta potential at the channel walls (in best cases, down to zero).

The sample ions present in the main channel will disappear in the reservoirs via the connecting side channels, and be *replaced* by ions from the opposite side reservoir. Note that if this mixing behavior between the sample ions in the main channel and the ions in the side reservoirs is unwanted, one could think of placing the MHD pump downstream of the experiment.

5.4 Summary

We described the electric working principles of our pump with a simple model that is similar to electrical resistance measurements. This model enabled us to also calculate the expected electroosmotic flow induced by an electric field in the main channel. Eo velocity was compared with the expected MHD velocity to explore the limitations of our pump in terms of the inevitable electrokinetic flows that disturbed MHD flow. Treating the surface of the channel with uncharged molecules should drop the electroosmotic flow, and placing the MHD pump downstream of the microfluidic system should prevent any unwanted mixing of ions from the side reservoirs with sample ions in the channel.

Bibliography

[1] C. Schwer and E. Kenndler. Electrophoresis in fused-silica capillaries: The influence of organic solvents on the electroosmotic velocity and the ZETA potential. *Analytical Chemistry*, 63:1801 – 1807, 1991. exp. det. of pK fused silica.

[2] Y. Gu and D. Li. The Zeta-potential of glass surface in contact with aqueous solutions. *Journal of Colloid and Interface Science*, 226:328–339, 2000.

[3] B.J. Kirby and E.F. Hasselbrink Jr. Zeta potential of microfluidic substrates: 1. theory, experimental techniques, and effects on separations. *Electrophoresis*, 25:187–202, 2004.

Chapter 6

MHD pumping in NMR environments

In this chapter, we present our DC magnetohydrodynamic (MHD) pump as a component of a nuclear magnetic resonance (NMR) microfluidic chip. This is the first time that MHD pumping in an NMR environment has been observed and demonstrated. The design of the chip was changed from straight to U-shaped channel (with same total length) to reduce the overall dimensions of the pump, and thus to facilitate its integration in the NMR measurement system. This chip generates a maximum flow rate of 1.5 $\mu L \cdot min^{-1}$ (2.8 $mm \cdot s^{-1}$ in the microchannel) for an applied voltage of 19 V (1600 $A \cdot m^{-2}$ with 1M buffer) in a 7 T NMR superconductive magnet. We developed a simple method to measure flow rate inside the bulky NMR magnet by monitoring the displacement of a liquid-liquid interface of two immiscible liquids in an off-chip capillary. Flow rate measurements of beads and liquid-liquid interface as a function of both current and magnetic field intensity of permanent magnets were compared, and showed equivalent results. This allowed us to characterize and compare the flow rate generated by the micropump using a permanent magnet (B_1 = 0.33 T) with the NMR superconductive magnet (B_0 = 7.05 T). We observed a 21-fold increase in flow rate corresponding to the ratio of the magnetic field intensities (B_0/B_1 = 21) in accordance with the theoretical flow dependence on the magnetic field intensity. The final aim is to integrate MHD pumps together with planar NMR coils in a microfluidic system for NMR analysis [1]. The work presented in this section includes the results obtained by Mr. Frieder Lucklum [2] during his internship under our supervision.

6.1 Experimental methods

The design and working principle of this DC MHD pump, as well as the standard working buffers, has been described in Chapter 4 and in [3].

6.1.1 Micropump fabrication

In order to reduce the dimensions of the pump, we introduced small modifications to the process described in section 4.2.1. We processed two complementary sets of Pyrex wafers in our cleanroom facility. The first set of wafers includes the microchannel, and the second the holes for fluidic access to the side-reservoirs. The design and fabrication process for the two sets of wafers are shown in Fig. 6.1. Before step 1, we dipped both sets[1] in 50% HF for 25 min. The result was through holes: 700 µm diameter holes in the first set for bottom access to the microchannel, and rectangular shaped holes in the second set for fluidic access from the top to the side-reservoirs. The first set of wafers was then processed as previously described in section 4.2.1.

The main channel (16 mm × 150 µm × 75 µm) is now U-shaped to make the overall dimensions of the pump smaller. A total number of 785 side-channels were etched across the main channel. The side-channels widths and spacing were 10 µm, the depth 100 nm, and their length varied from 10 to 100 µm. The side-reservoirs were 75 µm deep and their detailed dimensions are shown in Fig. 6.2. We initially planned a final step with evaporation of platinum electrodes on the bottom of the side reservoirs. This step was temporarily halted due to two major technology problem related

---

[1] with structured 400 nm polysilicon and 1.8 µm of AZ1518 photoresist as an etch mask

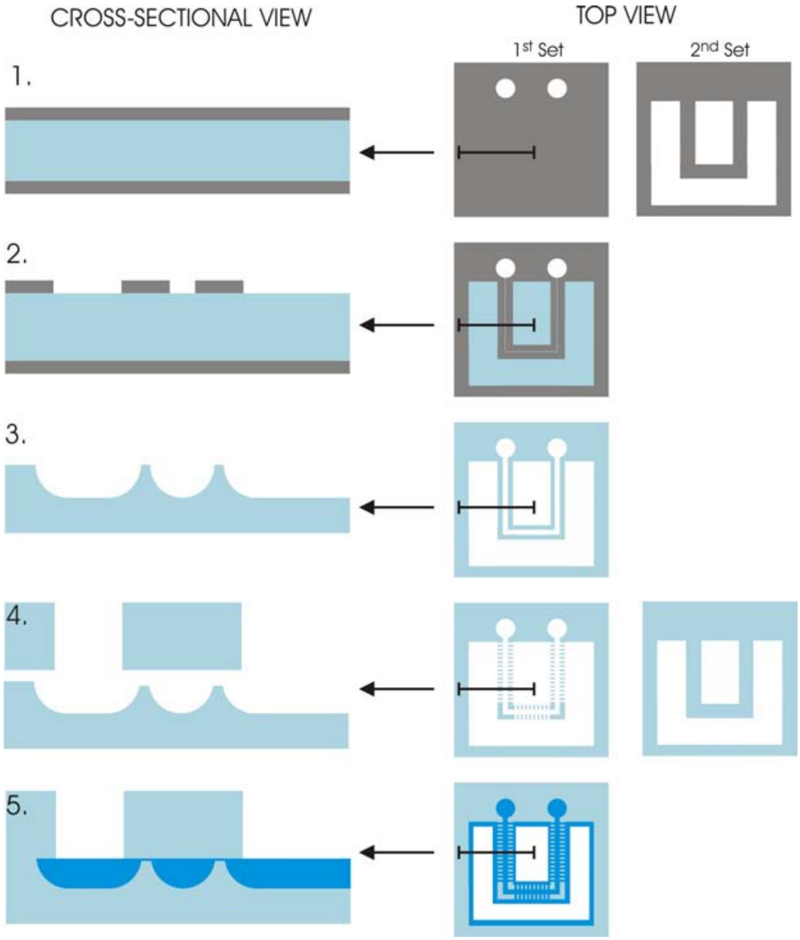

Figure 6.1: Microfabrication steps for the micropump. 1. Start with Pyrex wafers coated with 400 nm CVD polysilicon. 2. Photolithography followed by RIE etching to define the channel and the side-reservoirs location. 3. Deep 20% HF etch: defines the length of the side-channels. Polysilicon removal with KOH. 4. Photolithography with spray photoresist followed by BHF etch of the shallow side-channels; alignment of the wafer with a Pyrex coverplate. 5. Fusion bonding of both Pyrex wafers at 650˚C.

to electrical contact[2] and fusion bonding efficiency.

For pump encapsulation and fluidic connection of the holder with outer capillaries, we chose non-ferromagnetic material [3]. In other words, the material was chosen so that there was no interaction with the strong magnetic field of the NMR superconductive magnet. We chose PMMA material for the encapsulation of the pump. Figure 6.3 shows a picture of the holder. We present a three dimensional view and detailed dimensions of the holder in appendix B. We employed small O-rings for the fluidic sealing at the bottom chip-holder interface. We assembled the top and bottom part of the holder with screws made in copper. We integrated the platinum wire electrodes on the top part of the holder. A thin sheet of latex[4] provided a proper sealing between the chip and top part of the holder. The top part also served as a reservoir for ionic current generation. We connected the holder with outside capillaries with 062 Minstac fittings (The Lee Company, Westbrook, CT, USA).

6.1.2 Experimental setup

We used the same citrate phosphate buffers as those in chapter 4. The buffers composition were 53 mM citrate (pH = 6), with 207 mM phosphate for 0.25 M buffer, and with 244 mM or 744 mM KCl in addition to reach ionic strengths of 0.5 M or 1 M respectively. For each buffer concentration, we measured the pH and conductivity with electrodes from ThermoOrion company (Beverly, MA, USA). We saturated the buffer with amaranth, a red-colored salt, to bring visual contrast for flow observations. Table 6.1 shows the measured properties of the buffer solutions. Polystyrene beads (carboxylate-modified microspheres, 2.55% in water, from Polysciences Europe GMBH, Germany) with a diameter of 6 µm were diluted 500 times

---

[2] The metal lines were disrupted at the edge of the channel, where the channel side-wall is nearly vertical.

[3] See appendix C for a discussion about magnetic classification of materials.

[4] The sheet of latex was manufactured by pouring first a monolayer of liquid latex (XUR® liquid latex, Michael Schermons, Berlin, Germany) on a flat surface, letting it dry, and then cutting a piece having the shape of the parts to seal together.

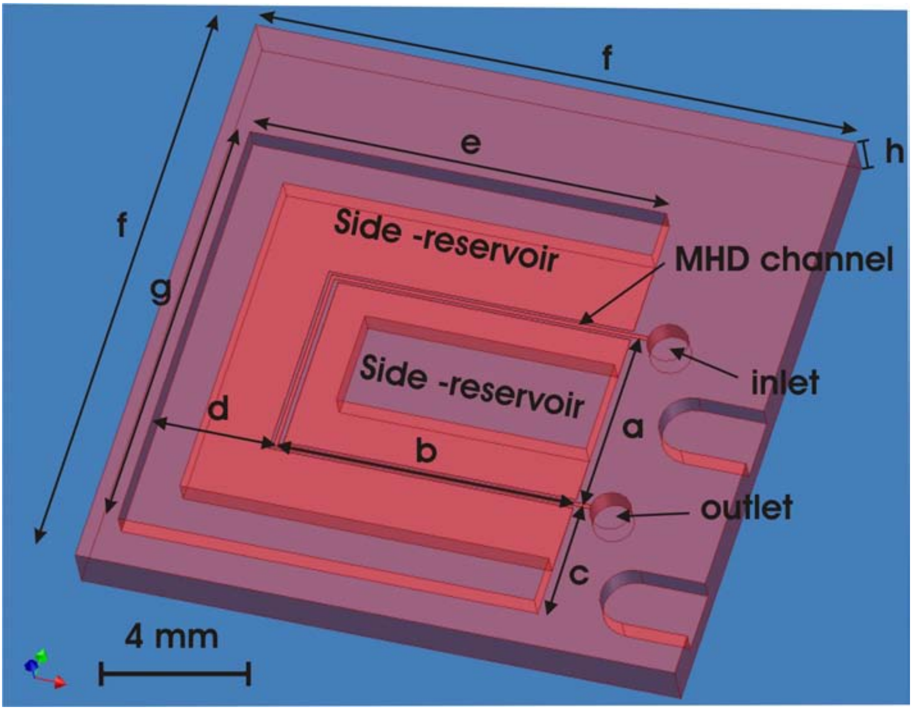

Figure 6.2: Three dimensional drawing of the MHD pump (Drawing courtesy of F. Lucklum). The dimensions of the chip and side reservoirs were: a = 4 mm, b = 6 mm, c = 2.45 mm, d = 2.4 mm, e = 8.4 mm, f = 12.65 mm, g = 8.95 mm, h = 1 mm. We measured the dimensions on a processed chip, with a precision of ± 0.05 mm.

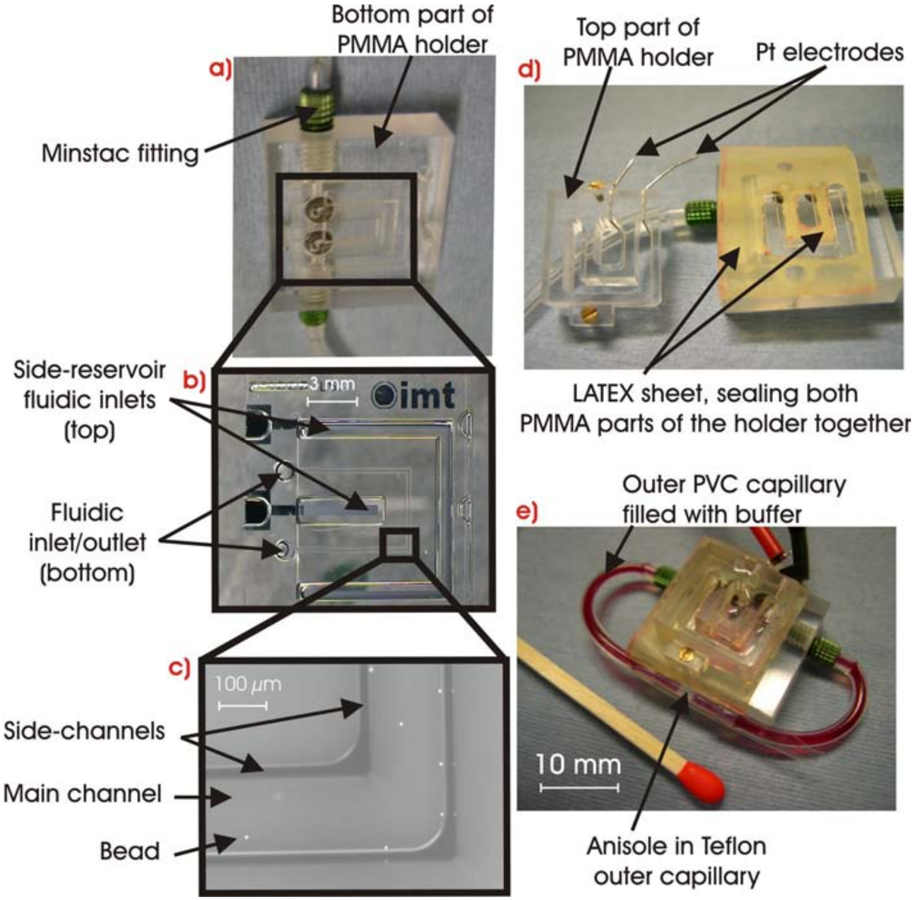

Figure 6.3: (a) View of the chip on top of the O-rings on holder. (b) View of the chip with integrated platinum electrodes on the bottom of the side-reservoirs (c) Close-up view of a channel with flowing beads inside. (d) View of the chip with the latex sealing before closing the holder. (e) View of the encapsulated chip filled with amaranth-colored buffer. The anisole bubble is the transparent plug in between buffer seen on the outer capillary in front of the holder.

Table 6.1: Electric and chemical properties of the buffers used [4]

	Conductivity [mS·cm^{-1}]	Resistivity [Ω·m]	pH
0.25 M Buffer	21.4	0.47	6.3
0.5 M Buffer	44.9	0.22	6.0
1 M Buffer	88.3	0.11	5.8
1 M Buffer + Amaranth	87.8	0.11	5.9

in the buffer for flow visualization. A constant current (0 - 5 mA) was applied across the two Pt electrodes with a 2400 source meter from Keithley Instruments S.A. (Zurich, Switzerland), the compliance of the source was set to 100 V.

We utilized NdFeB rare earth magnets (Forcefield, CO, USA) of varied magnetic field strength for the pumping experiments on top of permanent magnets. We chose magnet diameters of 50 mm (diameter larger than the chip dimensions, see Fig. 6.4) and designed the chip holder as thin as possible to ensure good homogeneity of the magnetic field in the microchannel. The magnetic field intensities were measured with a 3- axis magnetic-field transducer (model 3MR-1C, Sentron AG, Switzerland). For those measurements, we positioned the Hall sensor at the exact height corresponding to the microchannel position. Therefore, we measured two different magnetic field intensities of B_1 = 0.33 and B_2 = 0.38 T. We performed the experiments within the NMR superconductive magnet in collaboration with Klaus Ehrmann of the LMIS3 laboratory in EPFL. This magnet was part of a 300 mHz NMR spectrometer setup (DRX 300, Bruker Biospin AG, Switzerland). The intensity of the static magnetic field generated inside the bulky NMR superconductive magnet was calculated to be 7.05 T. The working space inside this magnet was limited: it has a cylinder volume of 40 mm diameter, and experiments had to be conducted at a specific height position

Table 6.2: Physical properties of anisole and aqueous solutions

	Viscosity [mPa·s^{-1}]	Relative density	Solubility in water	Surface tension [nN·m^{-1}]
Anisole	1.06	0.99	poor	35.1
Water	0.89	1	high	71.99
1 M Buffer	1.09	1	high	$\leq$ 71.99

where the field is uniform[5]. We also designed a custom holder for the experiments inside the NMR magnet to allow the MHD pump to be positioned in the homogeneous field region, and to contact the Pt electrodes with the current source outside of the NMR instrument (see Fig. 6.5).

6.1.3 Flow measurement methods

We conducted the flow measurements in a closed loop fashion by connecting the inlet and the outlet of the PMMA holder with an off-chip PVC capillary (inner diameter of 1 mm). We measured the flow velocity with the same bead technique as described in section 3.1.3.

In the bulky B_0, we developed an indirect measurement method to observe MHD flow rate, as optical characterization was not possible in such an apparatus. We measured the lateral displacement of an Anisole-bubble interface in between the amaranth-colored buffer. We chose anisole for its immiscible properties with water, and because it has the same viscosity and density as water (see Table 6.2). The surface tension of anisole[6], however, differed significantly from aqueous solutions. We measured the anisole plug displacement in a Teflon capillary (5 cm long, inner diameter of 0.81 mm) connected in between the outer PVC capillaries. The flow rate in the

---

[5] This distance was approx. h = 270 mm from the bottom entrance of the NMR cylinder.

[6] Anisole wets the Teflon capillary wall better than water.

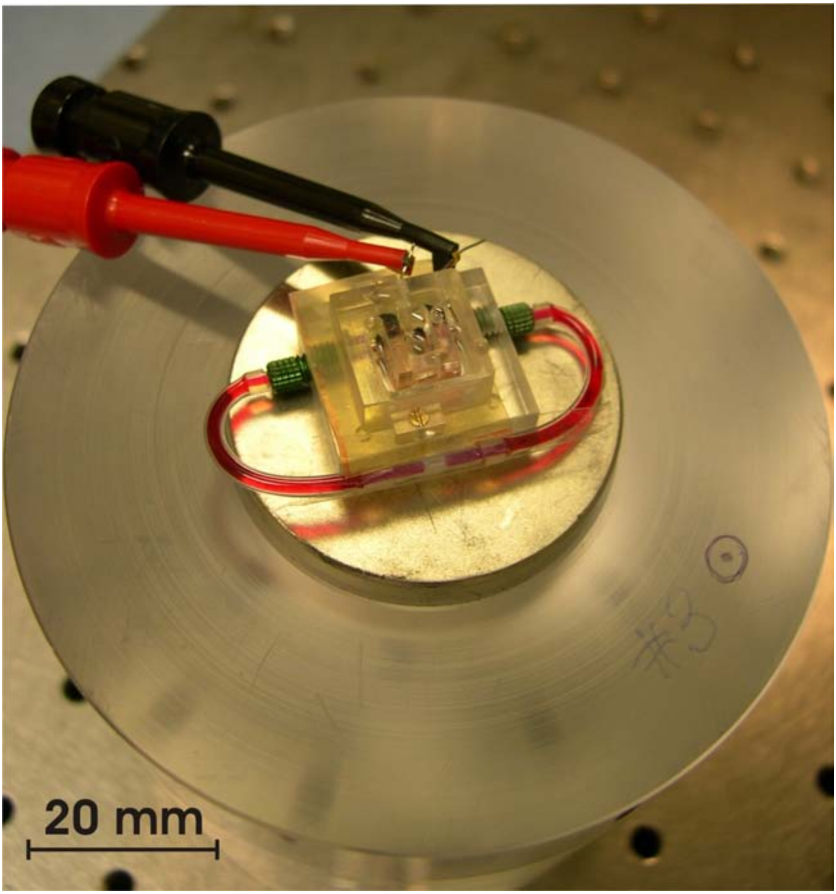

Figure 6.4: View of the chip holder for measurement on top of a 40 mm diameter NdFeB permanent magnet (with 1.5 cm long Teflon flow measurement capillary).

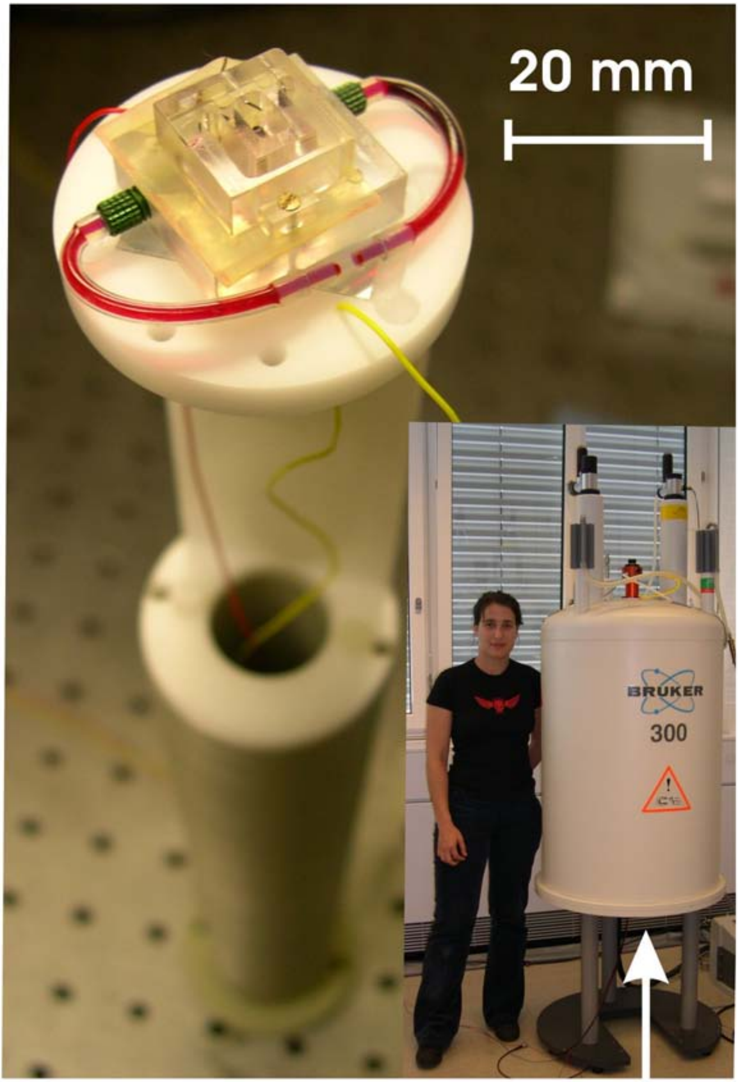

Figure 6.5: View of the chip holder for measurement inside the bulky superconductive magnet (with 1.5 cm long Teflon flow measurement capillary). A picture of the NMR superconductive magnet is seen on the right. The holder is inserted into the NMR magnet from the bottom, as the white arrow indicates.

whole microfluidic system (Q) is directly proportional to the lateral displacement (dh) of the plug. For a given measurement time dt we will have:

$$Q = \frac{dh}{dt} \cdot \pi r_{\mathrm{CAP}}^{2} \tag{6.1}$$

where r_{CAP} is the radius of the teflon capillary used for the flow rate measurement. The continuity of the system implies that the flow rate is the same in the measuring capillary as it is in the microchannel (only the velocities differ), we used equation 2.15 (for half circular channels[7]) for comparison with theory. We estimated the error on the displacement measurement to be half of the smallest graduation of our scale meter; the error was thus 0.25 mm.

6.2 Results and discussion

Fig. 6.4 shows a close-up top view of the encapsulated chip. The top reservoirs are filled with the buffer. When both side-reservoirs and main channel of the chip are filled, the ionic current can be generated between the electrodes.

6.2.1 Electrical characterization

We first characterized the current-voltage behavior of the chip as a function of the conductivity of the solutions and the geometry of the side-channels.

Ionic strength

The upper panel of Fig. 6.6 shows the current-voltage behavior for a micropump with 20 μm long side-channels, filled with buffers of selected conductivities. We see that the higher the concentration, the higher the current for a fixed voltage. The current increases linearly with the voltage until a certain point where the linearity is lost. Above this threshold, the temperature of the solution begins to rise: Joule heating begins. The voltage

---

[7] $Q = \frac{3\pi}{128\mu}\frac{l}{L} \cdot h^4 \cdot J \cdot B$

threshold is different for each solution, it is higher for the less concentrated buffers.

Side-channel length

When a given voltage is applied across the side-channels, the electrical resistance of the pump will depend on the dimensions of the side-channels. More specifically, the longer the side-channels, the higher the electrical resistance and therefore the less the current intensity in the main channel. We designed the new pump with 4 different side-channel lengths, namely 10, 20, 50 and 100 µm. The aim of the side-channels is to produce a DC ionic current as high as possible in the main channel for a given DC voltage without any bubble formation or Joule heating in the main channel. The bottom panel of Fig. 6.6 shows the current-voltage behavior of micropumps with 3 different side-channel lengths for a buffer solution of 1 M ionic strength. We see that, for the same buffer conductivity, the shorter the side-channel length, the higher the current for a given voltage. The voltage threshold of the linear range is also different for each geometry. The voltage threshold is higher for the longest side-channels geometries. The slope of the current-voltage curve in the linear range corresponds to the measurement of the electrical resistance of the pump. As expected from Equation 5.6 (expressed from our electrical model presented in Chapter 5), the resistance is proportional to side-channel length. The 10 µm long side-channels should then show the best electrical behavior. Although the chips with the best bonding reproducibility were the 100 µm long channels, we performed the experiments with MHD pumps of 20 and 50 µm side-channels geometry. The current generated by the 100 µm long side-channels was too small to achieve any noticeable MHD pumping with the permanent magnets. We also could not test MHD pumps with 10 µm long side-channels as none of them did bond properly after the fusion bonding microfabrication step[8].

---

[8] The available surface was too small to allow sufficient adhesion for proper bonding

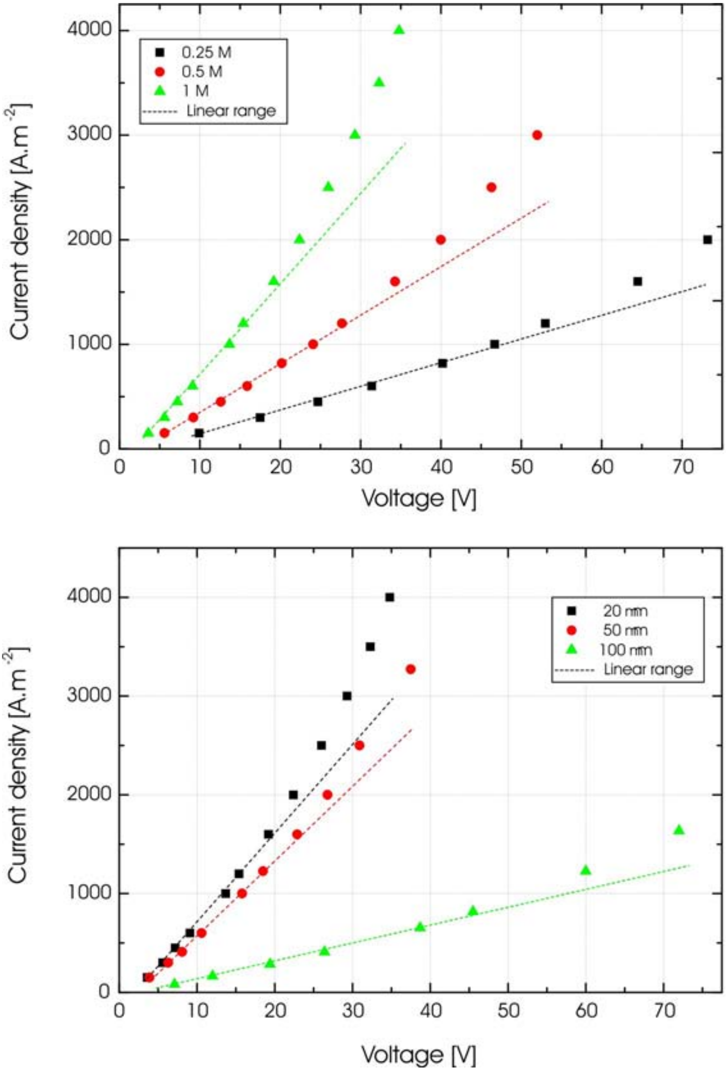

Figure 6.6: Characterization of the new chip with current-voltage curves. The deviation on the voltage measurement corresponds to 1% of each data value. The data linear fit is represented by the dotted lines. [Top] Chip behavior as a function of the ionic strength of the buffer (chip with 20 µm long side-channels). [Bottom] Chip behavior as a function of the length of the side-channels (chip filled with 1 M buffer).

Table 6.3: Comparison of the Joule heating thresholds as a function: (*1*) Of side-channel lengths with 1 M buffer solution in the pumps; (*2*) Of buffer ionic strengths in a pump with 20 µm long side-channels .

(*1*)	U [V]	J_{max} [A·m^{-2}]	Q_{diss} [W·m^{-1}]
20 µm	19	1600	2.1
50 µm	23	1600	2.6
100 µm	45.5	818	2.7

(*2*)	U [V]	J_{max} [A·m^{-2}]	Q_{diss} [W·m^{-1}]
0.25 M	47	1000	3.4
0.5 M	28	1200	2.4
1 M	19	1600	2.1

Joule heating

In Fig. 6.6 the Joule heating threshold has been determined for all three side-channel lengths (20, 50, and 100 µm) with a 1 M buffer, as well as for all three buffer concentrations (0.25, 0.5, and 1 M) in a pump with 20 µm long side-channels. Table 6.3 summarizes those values. The Joule heating threshold occurs when the voltage - current behavior of the pump ceases to be linear. At this point, the system begins to heat up, and the increase in temperature changes the physical behavior of the pumped fluid (see 2.3.1 for details). For each of these thresholds, we also calculated the corresponding power dissipation (Q_{diss}) using equation 4.2. Corresponding Q_{diss} vary from 2.1 to 3.4 W·m^{-1}. The applied voltage should therefore not be higher than 19 V for MHD pumping of a 1 M solution with the 20 µm long side-channel geometry, and 23 V for 1 M solution with 50 µm long side-channels.

Bubble generation

Another limiting factor that may affect our system in terms of duration of a single experiment is the rate of bubble generation around the Pt electrodes. We observed that after a certain time (30-60 min), the bubbles around the electrodes in the outer reservoir (on top of the holder) do not escape in the air, but stay in the space between the electrode, the PMMA reservoir and the buffer solution. This insulating gaseous spacing between the electrode and the buffer gradually decreases current generation between the electrodes (for a fixed voltage). This is so far the only time-limiting factor encountered with our pumping system, and it is easily avoided by decreasing the operating current density. This time limitation prevented us to perform flow rate measurements at high current density (> 500 A·m^{-2}) for durations longer than 30 min.

6.2.2 Characterization of the new flow rate measurement method

Inside the superconductive magnet, the flow rate was characterized by tracking the displacement of a liquid-liquid interface within a teflon capillary connected in a closed-loop fashion with the pump. Various interfaces were tested, the most reproducible results could be achieved by introducing a "bubble" of Anisole in the buffer solution. Anisole is a derivative of benzene, with similar viscosity and density as water. We conducted the flow rate measurements as follows. First the anisole plug was introduced in between the colored buffer in the teflon external capillary. A state of equilibrium was achieved when no movement of the plug was noticed. This equilibrium was reached after a mean waiting time of 30 min. Then the chip was fixed on top of the NMR chip holder (see Fig. 6.5) and inserted inside the NMR magnet. The measurement time began and ended when the current source was switched on and off, respectively. The plug position was recorded immediately after the current was switched off and the holder removed from the NMR magnet. As seen in the top panel of Fig. 6.7, the plug's displacement is a linear function of the measurement time, as expected by the theory.

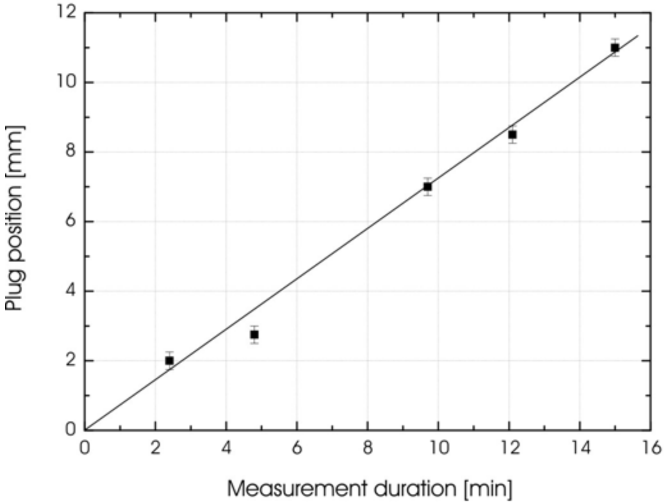

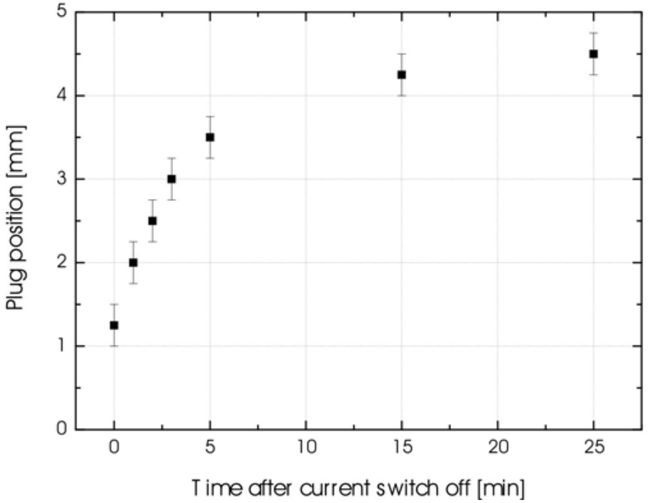

Figure 6.7: Evolution of the plug position. [Top] As a function of the total measurement time (20 µm long side-channels, 1M Buffer, J = 450 A·m^{-2}, U = 6 V, 5 cm long Teflon capillary). [Bottom] As a function of the waiting time after the end of measurement (50 µm long side-channels, 1M Buffer, J = 610 A·m^{-2}, U = 10 V, 1.5 cm long Teflon capillary).

Backflow

The time gap between the current switch-off and the plug position measurement was less than 5 seconds. This remark is important because we noticed a movement of the plug in the direction opposite to MHD pumping after each measurement. This reverse movement usually didn't exceed 10% of the total measurement[9], but in the case of a short measurement capillary (1.5 cm long, as depicted in Fig. 6.5) it could exceed 50%. This high reverse flow was measured for the 1.5 cm long capillary as a function of the elapsed time after measurement, and its evolution is seen in the bottom panel of Fig. 6.7. We see that the backflow is very fast within the first 5 minutes, and that it levels off after a waiting time of 15 min. This displacement in the reverse direction was also recorded 15 min after each measurement.

Equivalence with bead measurement technique

In order to validate the new flow measurement technique, we compared the ratios Q_x/B_x at a given current density. Theory says that Q_x/B_x should be constant when J is constant. For J = 650 A·m^{-2}, we had the following observations:

$$\frac{Q_{B_1}}{B_1} = 8.48 \cdot 10^{-2}\ \mu\text{L} \cdot \text{min}^{-1} \cdot \text{T}^{-1} \quad , \quad \frac{Q_{B_2}}{B_2} = 8.42 \cdot 10^{-2}\ \mu\text{L} \cdot \text{min}^{-1} \cdot \text{T}^{-1} \tag{6.2}$$

$$\text{and} \quad \frac{Q_{B_0}}{B_0} = 8.58 \cdot 10^{-2}\ \mu\text{L} \cdot \text{min}^{-1}\text{T}^{-1} \tag{6.3}$$

where Q_{B_1} and Q_{B_2} were flow rates measured with the bead velocity technique and permanent magnets B_1 and B_2, and Q_{B_0} was the flow rate measured with the liquid-liquid interface technique in the NMR magnet of magnetic field intensity B_0. We see that all three ratios gave the same value (within 2 %), showing that both measurement techniques are comparable.

---

[9] for long Teflon measurement capillaries of typically 5 cm long

6.2.3 Measurements with permanent magnets

In small B environments, i.e. when the MHD pump was characterized with permanent magnets, the flow rate was measured by means of bead velocity and anisole-bubble displacement. We did our measurements with MHD pumps having 20 µm long side-channels, and 1 M buffer as the pumped solution. The maximum flow rates, corresponding to an applied current density of 650 A·m^{-2}, were respectively 0.028 and 0.032 µL·min^{-1} for magnetic field intensities of respectively B_1 = 0.33 and B_2 0.38 T. The bead velocity as a function of the applied current density for two different permanent magnets can be seen in Fig. 6.8. We see that the measured flow is proportional to the applied current and that it follows theory.

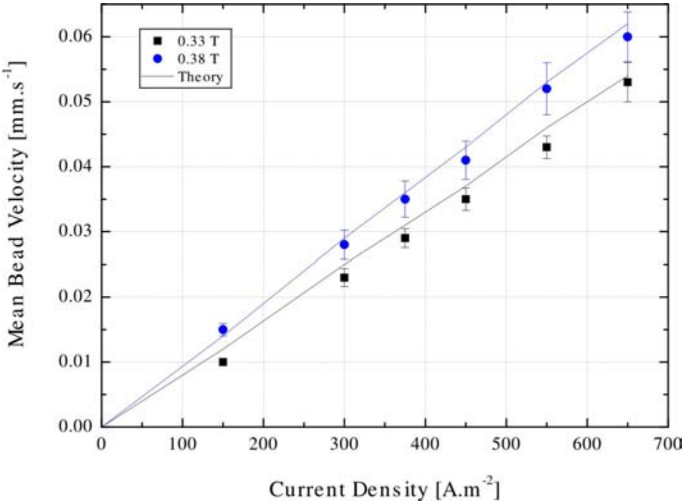

Figure 6.8: MHD Flow mean velocity as a function of current density (for 2 different magnetic field intensities, 20 µm long side-channels, and without anisole). Error bars indicate the standard deviation for 10 beads in a total sample of 50 beads per measurement. The straight line is the theoretical mean velocity, calculated using equation 2.16.

This measurement was only possible if the fluidic system was closed by connecting the inlet and outlet with outside capillaries in a closed-loop fashion. In fact, the flow rate generated by MHD in small B environments seemed to be too weak to dispense any movement in an open system. This closed-loop fashion enabled us to get rid of the unnecessary backpressure due to of hydrostatic and capillary forces. To understand the influence of hydrostatic pressure on the performances of the pump, we calculate the maximum body force generated by our pump for a current density of 650 A·m^{-2} and a permanent magnetic field of 0.38 T we will have (thanks to equation 2.14):

$$\Delta P = J \cdot B \cdot l = 650 \times 0.38 \times 16 \cdot 10^{-3} = 4 \text{ Pa} \tag{6.4}$$

This expression for the body force generated by our pump does not account for the influence of gravity. The hydrostatic pressure drop generated by gravity is proportional to the height difference (Δh) between two points so that:

$$\Delta P = \rho \cdot g \cdot \Delta h \tag{6.5}$$

where ρ is the fluid density, and g ($\approx$ 9.8 m·s^{-2}) is the gravity constant. If we calculate the threshold for Δh at which the hydrostatic pressure drop of our buffer equals the maximum MHD body force we obtain:

$$\Delta P = 4 = \rho \cdot g \cdot \Delta h \tag{6.6}$$

$$\Delta h = \frac{4}{10^3 \cdot 9.8} = 4.1 \cdot 10^{-4} \text{ m} = 0.4 \text{ mm} \tag{6.7}$$

This means that if we try to measure the flow rate of our micropump by leaving the inlet and outlet open with a height difference higher than 0.4 mm (which is easily achievable) we will be unable to observe any movement induced by the MHD phenomenon only. The closed loop configuration of the system enabled us to cancel out the flow perturbation due to hydrostatic pressure.

Note that the bead flow measurements were not performed simultaneously with anisole bubble displacement. At low current densities (less than

500 A·m^{-2}), the measured flow rates with the anisole interface technique were at least half those calculated from theory, and the less the current, the more the gap between theoretical flow rate and measurements. In fact the anisole bubble seemed to introduce a resistance to the flow for low current densities. This resistance was not observed when the beads only were present. Moreover, the equivalence of those two flow measurement methods with permanent magnets was only observed for high current densities (higher than 500 A·m^{-2}). Therefore we state that the bead measurement technique is a suitable technique for low flow rates measurements, whereas the anisole bubble displacement is best for high flow rates observations.

6.2.4 Measurements in NMR superconductive magnet

Preliminary results of MHD pumping in NMR environments with our previous MHD pump (described in chapter 4) were conducted by Frieder Lucklum. The MHD pumping was successful, and results are described in detail in his internship report [2].

In the NMR environment we characterized the flow with two different side-channel lengths for the MHD pump geometry (namely 20 and 50 µm long) and 1 M buffer as the pumped solution. We measured the displacement of the anisole plug as a function of the applied current. In any case, we compared the measurements with theory. Every pump gave equivalent results, namely very good aggreement with theory. An example of the evolution of the flow rate in the NMR magnet as a function of current density for a pump with 20 µm long side-channels is shown in Fig. 6.9. We see that the measured flow rate depends on the applied J and increases with it in a linear fashion, as for flow with permanent magnet actuation. For low values of current, the measured flow rate is lower than our calculations, but corresponds again for $J \geq 450$ A·m^{-2}. This phenomenon at low J is believed to be related to capillary pressure issues. The results presented in expressions 6.2 and 6.3 can also be used to show that the volumetric flow rate scales

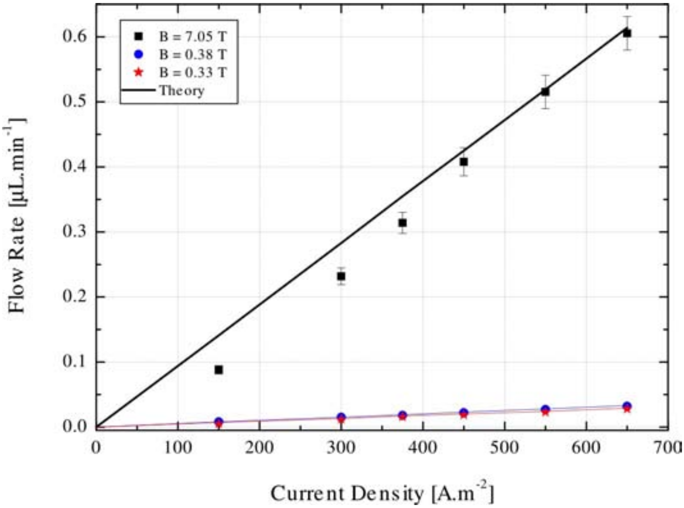

Figure 6.9: MHD Flow rate as a function of current density (for 3 different magnetic field intensities, and 20 µm long side-channels). Error bars indicate the systematic error of the scale-measurement method. The straight line is the theoretical flow rate, calculated using equation 2.15.

with the magnetic field:

$$\frac{Q_{B_0}}{Q_{B_1}} = \frac{0.605}{0.028} = 21.6 \quad and \quad \frac{B_0}{B_1} = \frac{7.05}{0.33} = 21.4 \tag{6.8}$$

$$\frac{Q_{B_0}}{Q_{B_2}} = \frac{0.605}{0.032} = 18.9 \quad and \quad \frac{B_0}{B_2} = \frac{7.05}{0.38} = 18.5 \tag{6.9}$$

The change from the permanent magnets (B_1, B_2) to the NMR magnet (B_0) increased the field strength by a factor of 18.5 and 21.4 respectively. The MHD measurements (at a fixed current density of 650 A·m^{-2}) showed an increase in the flow rate by a factor of 18.9 and 21.6 respectively. As the flow rates at a fixed current density for the same chip geometry are directly proportional to the magnetic field strength (see expression 2.15), the equivalence of the ratios proved the flow rate dependance on B.

The maximum body force generated by our pump for a current density of 1600 A·m^{-2} and a NMR magnetic field of 7.05 T is:

$$\Delta P = J \cdot B \cdot l = 1600 \times 7.05 \times 16 \cdot 10^{-3} = 180.5 \text{ Pa} \tag{6.10}$$

which corresponds to a height difference (see equ. 6.5) of:

$$\Delta h = \frac{180.5}{10^3 \cdot 9.8} = 1.8 \cdot 10^{-2} \text{ m} = 18 \text{ mm} \tag{6.11}$$

So far, the only MHD pump that generated a MHD body force of more than 100 Pa was fabricated by Eijkel *et al.* [5]. Combining an AC magnetic field of 0.1 T, an AC current density of 21100 A·m^{-2}, on a total electrode length of 63 mm, they generated a maximum body force of 133 Pa.

With regard of these results, we see that MHD pumping in an NMR environment has been successfully achieved. The pumping flow rate is rather low, with a maximum of 1.5 µL·min^{-1} for an applied current of 1600 A·m^{-2} (corresponding voltage of 19 V for 20 µm long side-channels). This low flow rate may be problematic if one wants to monitor a chemical reaction with fast kinetics. In this case, the pump should be integrated together with the NMR detection coils on one single chip so that the distance between the pumping/mixing part and the NMR analysis microcoils is minimized. It was not possible in our case to integrate the pump and the NMR coils on one single chip because of geometrical issues: the NMR microfluidic chip has to stand in a plane parallel to B_0, whereas the MHD chip has to stand perpendicular to B_0.

6.3 Summary

We developed a simple method of flow rate measurement inside the bulky NMR magnet, and we successfully achieved MHD pumping inside an NMR environment in accordance with MHD theory. The flow characterization method with immiscible fluids is suitable for high flow rates observation (namely for $J \geq 500$ A·m^{-2}), whereas the bead velocity method is best for lower flow rate characterization on top of permanent magnets. The pumping flow rate is rather low, with a maximum of 1.5 µL·min^{-1} (high flow velocity of 2.8 mm·s^{-1} in the microchannel) for an applied current of 1600 A·m^{-2} in the 7 T NMR superconductive magnet. Future work with these devices include the integration of this MHD pump into a µTAS for NMR analysis. The envisioned applications are online monitoring of a chemical reaction with our pump also used as the mixer, and non-destructive MHD flow characterization by NMR microcoils.

Bibliography

[1] C. Massin, F. Vincent, A. Homsy, K. Ehrmann, G. Boero, P.-A. Besse, A. Daridon, E. Verpoorte, N.F. de Rooij, and R.S. Popovic. Planar microcoil-based microfluidic NMR probes. *Journal of Magnetic Resonance*, 164:242–255, 2003.

[2] F. Lucklum. *MHD pump integration into NMR environment*. Internship report, University of Neuchatel, 2005.

[3] A. Homsy, S. Koster, J.C.T. Eijkel, A. van den Berg, F. Lucklum, E. Verpoorte, and N.F. de Rooij. A high current density DC magnetohydrodynamic (MHD) micropump. *Lab On a Chip*, 5:466–471, 2005.

[4] D.R. Lide. *C.R.C. Handbook of Chemistry and Physics*. 76th edition, 1995.

[5] J.C.T. Eijkel, C. Dalton, C.J. Hayden, J.P.H. Burt, and A. Manz. A circular ac magnetohydrodynamic micropump for chromatographic applications. *Sensors and Actuators B*, 92:215–221, 2003.

Chapter 7

Integration of Nuclear Magnetic Resonance detection with microfluidics and MHD pumping

This chapter describes the integration of NMR detection with microfluidics and MHD pumping. We first present the technological challenges associated with integrating NMR coils with a glass microfabricated microfluidic chip. The second section describes preliminary experiments where we combined MHD pumping with NMR detection. The two last sections describe feasibility studies for applications involving the integration of NMR detection together with MHD pumping. The NMR phenomenon, basic theory and applications have been introduced in section 1.5.

7.1 Fabrication of microchannels compatible with NMR

The largest challenge associated with NMR methodology is the sensitivity of detection. To maximize sensitivity, it is important that the microfluidic structures are designed in such a way that optimum homogeneity and

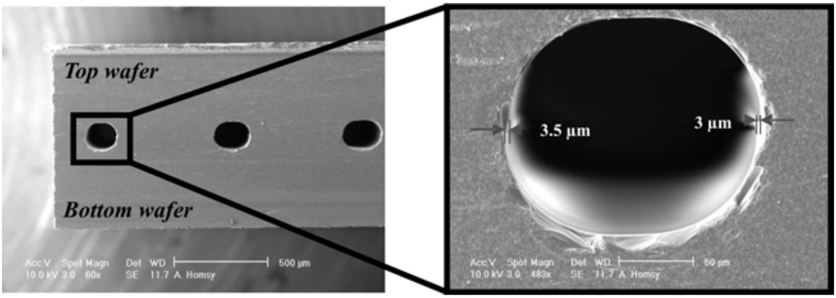

Figure 7.1: Cross-sectional eSEM view of channels of symmetric cross-section

strength of the magnetic field is achieved in the detection volume. Both theoretical considerations and simulations performed at the EPFL for this project indicate that the magnetic field homogeneity should be better maintained in microchannels and cuvettes with symmetrical cross-sections. We used Pyrex-glass wafers as a substrate for the microfluidics devices. Pyrex channels were etched isotropically in liquid HF to form a rotated-D-shaped cross-section. Then, two Pyrex wafers with complementary etched channels were aligned and bonded to obtain the final symmetric cross-section (see Fig. 7.1). Next, the NMR probes were microfabricated on top of the device by our partners at EPFL - LMIS3 [1–3]. Figure 7.2 shows a schematic view of the fabrication of the chip as well as pictures of the NMR probe integrated on top of the microchannels.

7.2 Combining MHD pumping with NMR detection

In order to combine MHD pumping with NMR detection, the position of the channels with respect to the static magnetic field B_0 of the NMR spectroscopy apparatus is of great importance: best pumping efficiency is achieved when B_0 is perpendicular to both the pumping channel and the current density across the channel. In the NMR spectrometer, B_0 is vertical, which means that our chip must be positioned horizontally to generate

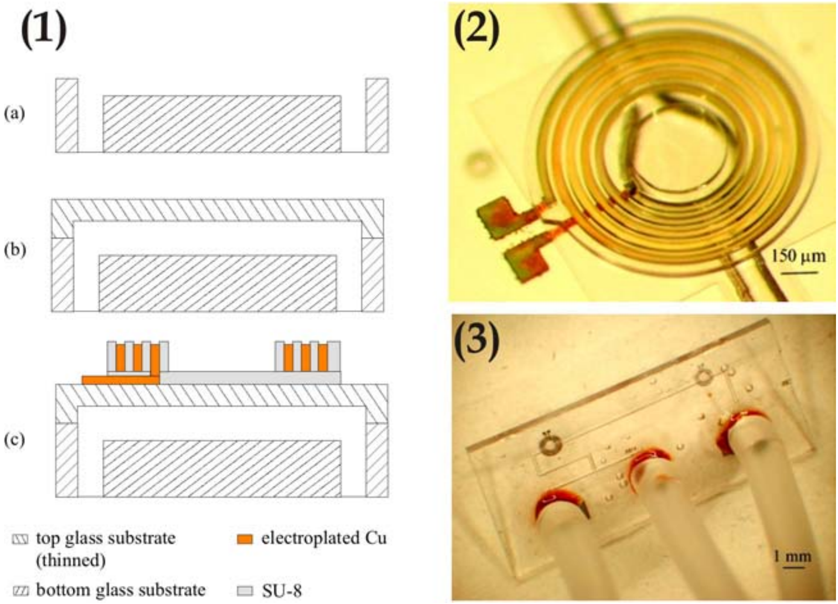

Figure 7.2: Planar NMR probe integrated on top of microchannels. **(1)** Simplified fabrication process of planar microcoils on a glass substrate with integrated channels. (a) Access holes and half channels are etched in the bottom substrate. (b) Half channels are etched in the top substrate, which is then fusion bonded to the bottom substrate. The top wafer is thinned down to a total thickness of 140 µm by polishing (75 µm chamber and channels, 65 µm membrane). (c) The planar coils are microfabricated using a patterned SU-8 layer as a mold for Cu electroplating. **(2)** Photo of a 5-turn, 500 µm inner diameter, electroplated coil on a glass substrate with integrated microfluidics. The sample chamber underneath the coil has a 500 µm diameter and 150 µm depth, resulting in an approximate sample volume of 30 nanoliters. **(3)** Monolithic NMR chip with integrated coils and microfluidic channels. Sample is injected trough connection tubes attached on the backside of the chip. The planar coil, which is on the opposite side of the chip, is electrically contacted using wire bonding. (All sketches and comments courtesy of C. Massin and F. Vincent, EPFL)

MHD pumping in the channel. However, the NMR chips have an integrated planar coil on top of microchannels, which generates an alternating field B_1 perpendicular to the plane of the chip. Therefore, if an NMR experiment is held with such a chip, the coil must generate a B_1 perpendicular to B_0 (see section 1.5). This means that the NMR chip has to be held vertically. This major geometry issue made it challenging to integrate both NMR and MHD functionalities in one single planar chip. One way to integrate NMR and MHD into one chip would be to fabricate a planar NMR coil that generates a B_1 in the same plane as the chip. This technology is possible for planar NMR coils [4] but was not readily available, and such developments are beyond the scope of this project.

Connecting two microfluidic chips

Since MHD integration with NMR in one single chip was not an attractive option in our lab, we decided to connect one vertical NMR microfluidic chip to our horizontal MHD pump in a closed loop fashion with the help of external PVC capillaries. We connected our pump to one of two existing NMR microfluidic chips. The first NMR chip was fabricated from Pyrex; the corresponding sample volume under the NMR coil being 540 nL. The second NMR chip was made of SU-8, and the sample volume under the NMR coil was 26 nL. We chose the SU-8 chip as a smaller volume was more appropriate to maximize the pumping velocity under the coil.

We considered two experimental concepts to characterize MHD pumping by the NMR chip. The *first concept* involved the introduction of the buffer/anisole/buffer interface in the NMR channel. The NMR coils monitor the entrance of one liquid into the NMR detection zone and the removal of the other. If several NMR acquisitions are performed during the liquid exchange, the spectra should show peaks of both liquids with changing signal strength. The *second concept* involved NMR monitoring of buffer alone[1] as a function of the applied MHD flow rate. The NMR signal will

---

[1] in the SU-8 channel

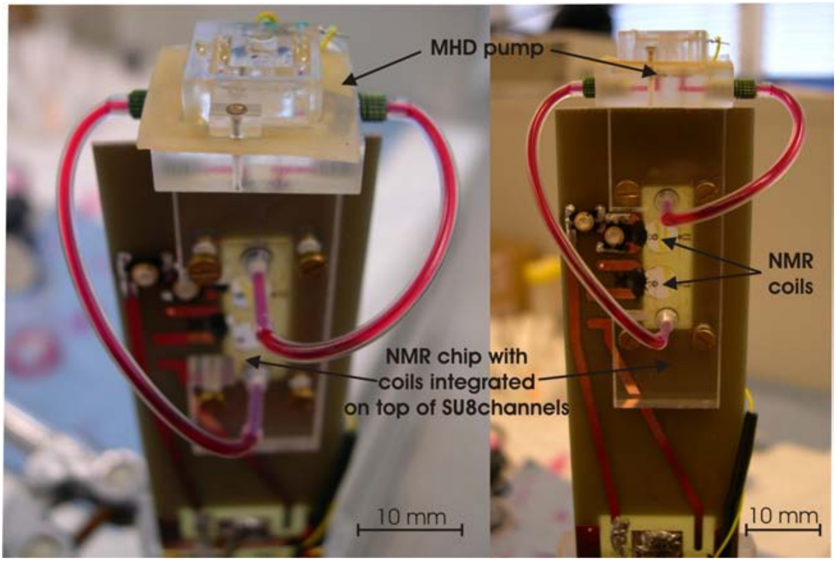

Figure 7.3: View of the chip holder for combined MHD pumping with NMR measurement inside the bulky superconductive magnet. The two microfluidic chips were connected together with outside PVC capillaries in a closed loop fashion. The NMR chip was fabricated from SU-8 channels and contained integrated NMR coils. The microchannel was 22 mm long, 360 µm wide and 65 µm deep. The coils integrated on top (and on the bottom) of the SU-8 channel covered 1100 µm of the length of the channel, corresponding to a sample analysis volume of $1100 \times 360 \times 65$ µm^3 (26 nL) under the coil. This NMR chip was developed, fabricated and handled by K. Ehrmann.

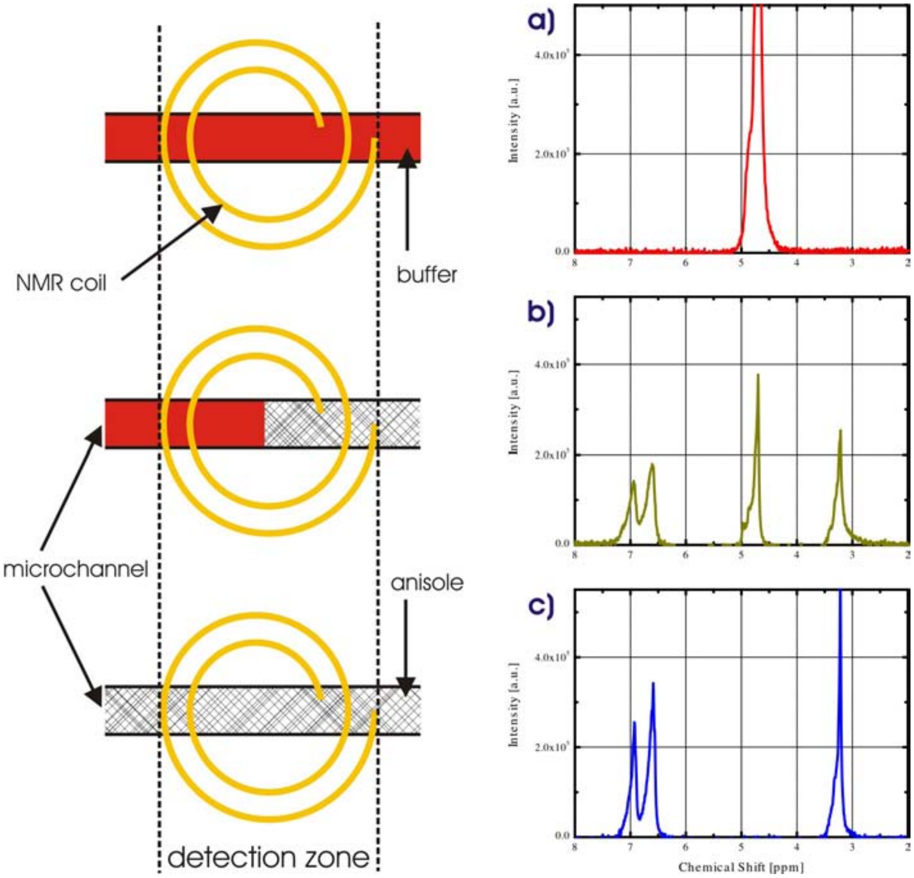

Figure 7.4: NMR spectrums acquired by K. Ehrmann with the SU-8 NMR chip connected to our MHD pump. The analyzed substances under the NMR coil were respectively: **a)** buffer alone, **b)** buffer + anisole, and **c)** anisole alone.

be at a maximum if the molecules excited do not leave the volume under the coil between excitation and detection. The NMR signal will be at a minimum if the molecules are fast enough to travel the whole volume under the coil between excitation and detection, leaving no NMR signal to be detected. A change in the peak intensity of water molecules will be observed as a function of the applied MHD flow rate if the flow velocity in the NMR channel varies between those two boundary conditions.

We chose the first concept because the expected maximum flow velocity under the coil was too slow to lead to any decrease in NMR spectrum intensity. All experiments were done in collaboration with K. Ehrmann (LMIS3 - EPFL). Fig. 7.3 shows a picture of the fluidic connection. The NMR microfluidic chip was developed by K. Ehrmann [5], and the geometry of the SU-8 channels was rectangular. Before the pumping experiments, we measured NMR reference spectrums of both chemicals in the SU-8 channels. The spectrums of anisole and buffer didn't overlap at all (see Fig. 7.4). Therefore, our simple technique should show if a movement of the buffer/anisole/buffer is taking place in the SU-8 microchannels. A body force of 180.5 Pa was imposed by the pump on the microfluidic system (J = 1600 A·m^{-2}). The flow rate Q in the microfluidic system is related to the pressure drop ΔP by Poiseuille law:

$$\Delta P = Q(R_{hy\ MHD} + R_{hy\ NMR}) \tag{7.1}$$

where $R_{hy\ MHD}$ is the hydraulic resistance of the half-circular MHD pumping channel (see Equ. 2.12) and $R_{hy\ NMR}$ is the hydraulic resistance of the rectangular SU-8 channels (see Equ. 2.11). The flow rate generated by the pump in this system will be 1.3 times less than what is generated by the pump alone. The flow rate in the system[2] is then 1.12 µL·min^{-1}, corresponding to an expected flow velocity in the SU-8 channel around 0.8 mm·s^{-1}. A liquid at the entrance of the SU-8 channel moving with a velocity of 0.8 mm·s^{-1} should cross the whole length in a little more than 27 seconds.

---

[2] The flow rate corresponding to 1600 A·m^{-2} for the pump alone is 1.5 µL·min^{-1}.

We could not measure any change of NMR spectrum between anisole and buffer when MHD pumping was actuated together with NMR detection. We discovered that the problem stemmed from the entrance of the SU-8 microchannel. After few fruitless attempts to analyze the problem, we observed that the SU-8 wall collapsed at the location of the fluidic connection. Since it was the only SU-8 chip available, we could not continue our MHD flow NMR analysis at this point of time. In fact, this SU-8 NMR chip was first designed to perform static NMR analysis. We believe that MHD flow measurements with interconnected NMR chips is possible, but the pump should be connected either to a new batch of low volume Pyrex NMR channels or with improved fluidic connection with the SU-8 channels.

Summary

MHD pumping combined with NMR detection has not been validated yet, but should be feasible by interconnecting two microchips[3]. In order to perform this measurement, a new cycle of chip designs is envisioned. The fast (but not so useful) solution would be to improve the fluidic connection between the chips by choosing tougher materials like Pyrex for the NMR chip or by adapting a gentle sealing to the inlet of the SU-8 channel. The second solution would be to develop a planar chip with integrated MHD pump and NMR coils. The timescale of this last solution would be longer than the first one, but the envisioned applications are more promising, as developed in the next section.

---

[3] The hydraulic resistance of the connected NMR chip must be equal of smaller than the one of the pump.

7.3 Perspectives on MHD-NMR applications

7.3.1 Chemical reaction actuated by MHD and monitored by NMR

One possible application of MHD-NMR devices is to use the MHD pump integrated in an NMR microfluidic chip[4] to enable dynamic monitoring of a chemical reaction [6], to monitor the interaction between two molecules [7, 8], or to observe conformation changes of macromolecules [9]. The MHD pump would play the role of the chemical reaction initiator, by initiating the mixing of the two chemical species. Two mixing methods are envisioned.

One method would place the MHD pump at the end of the microfluidic network (just before the outlet), two inlets channels leading to a single channel would allow both chemicals to enter the fluidic network, and to mix by diffusion. This kind of mixing method has already proven to be efficient, and enabled mixing times from 30 min down to 2 s [6], depending on the flow rate (defined by an off-chip syringe pump). In their experiments, it was important to set the intensity of the flow rate *not too high* (from 0.1 to 4 $\mu L \cdot min^{-1}$), to make sure the excited volume of the sample wasn't removed from the detection region before NMR signal acquisition was completed. With an MHD pump integrated in the microfluidic network, the flow rate will be controlled on-chip, and will correspond to the range of flow rate of interest (the maximum flow rate achieved by our last design of MHD pump geometry was 1.5 $\mu L \cdot min^{-1}$).

Another method would use our specific MHD pump geometry as the mixer for a chemical reaction, or as a method to change the solvent composition from a solution with suspended macromolecules (like proteins [9]). The way to use the pump as a mixer is to fill the pumping channel with one species and to fill the side reservoirs with the other. The mixing efficiency will depend on the ionic strength of the species (especially in the side reser-

---

[4] The NMR excitation will be achieved by an integrated planar coil that generates a magnetic field in the same plane as the chip, like in ref [4].

voirs). The mixing behavior of our MHD pump hasn't been studied in details[5], but it could be another application for our specific MHD design.

7.3.2 On-chip MHD flow monitoring by MRI

The ability to measure a flow by magnetic resonance imaging (MRI) was studied by Caprihan *et al.* [10], they demonstrated that it was possible to obtain a velocity profile of the material under flow. Very recently, Goloshevsky *et al.* [11] observed a two-dimensional flow profile by MRI in a capillary using two planar biaxial gradient coils incorporated with a planar Helmholtz RF NMR coil [12]. The envisioned application was to measure the viscosity of the fluid with the help of a non-invasive and non-destructive mode of operation. The measured variable is the velocity of the molecules in the capillary. Goloshevsky *et al.* measured velocities from 0.45 to 2.57 $\mathrm{mm \cdot s^{-1}}$ (with 0.05 $\mathrm{mm \cdot s^{-1}}$ resolution) for applied flow rates from 47 to 236 $\mathrm{\mu L \cdot min^{-1}}$ in 1.4 mm diameter capillaries. Attention was paid to the flow rate (generated by very precise syringe pumps) so that the flow wasn't too fast for the excited spins to leave the RF coil before being detected.

With such a measurement method it would be possible to observe and characterize the profile of MHD flows. MHD pumps with their high performances at relatively low flow rates could be a candidate of choice of flow actuation technique for NMR or MRI analysis[6].

7.4 Summary

This chapter was aimed to describe several aspects of the integration of microfluidics and MHD pumping together with NMR detection. We saw that substrates like Pyrex glass with HF etched cylindrical microchannels lead to

---

[5] The transient flow was indeed minimized in our developments by using nanometer-deep side-channels.

[6] The flow is slow enough for the excited spins not to leave the volume under the RF coil before being detected.

the ideal geometry for the integration of planar NMR coils. Preliminary experiments with interconnected glass MHD pump and SU-8 microchannel[7] were interrupted by fluidic connection perturbations due to the fragility of the SU-8 channel. The description of possible applications involving the combination of MHD pumping and NMR detection indicate the need in NMR techniques for low flow rates (in the range of 0.1 to 240 μL$\cdot$min^{-1}) so that the flow wasn't too fast for the excited spins to leave the RF coil before being detected. The high performances of MHD pumps at relatively low flow rates are therefore seen as an asset for NMR and MRI applications. Both examples of possible use of MHD in NMR devices are feasible if both systems are integrated in one planar microfabricated chip.

---

[7] with integrated NMR microcoils on top

Bibliography

[1] C. Massin, A. Daridon, F. Vincent, G. Boero, P.-A. Besse, E. Verpoorte, N.F. de Rooij, and R.S. Popovic. A microfabricated probe with integrated coils and channels for on-chip NMR spectroscopy. In Micro-TAS Conference, editor, *Micro Total Analysis Systems 2001*, Monterey - California, 2001.

[2] A. Homsy, J. Lichtenberg, C. Massin, F. Vincent, P.-A. Besse, R.S. Popovic, N.F. de Rooij, and E. Verpoorte. Fabrication of microfluidic channels with symmetric cross-sections for integrated NMR analysis. In Micro-TAS Conference, editor, *Micro Total Analysis Systems 2002*, Nara - Japan, 2002.

[3] C. Massin, F. Vincent, A. Homsy, K. Ehrmann, G. Boero, P.-A. Besse, A. Daridon, E. Verpoorte, N.F. de Rooij, and R.S. Popovic. Planar microcoil-based microfluidic NMR probes. *Journal of Magnetic Resonance*, 164:242–255, 2003.

[4] K.R. Minard, G.R. Holtom, L.E. Kathmann, P.D. Majors, B.D. Thrall, and R.A. Wind. Simultaneous 1H PFG-NMR and confocal microscopy of monolayer cell cultures: Effects of apoptosis and necrosis on water diffusion and compartmentalization. *Magnetic Resonance in Medicine*, 52:495–505, 2004.

[5] K. Ehrmann, N. Saillen, F. Vincent, C. Massin, P.-A. Besse, and R.S. Popovic. Microfabrication of Helmholtz coils with integrated channels for NMR spectroscopy. In Roland Zengerle, editor, *19th IEEE*

International Conference on Micro Electro Mechanical Systems, Istambul, Turkey, 2006.

[6] H. Wensink, F. Benito-Lopez, D.C. Hermes, W. Verboom, H.J.G.E. Gardeniers, D.N. Reinhoudt, and A. van den Berg. Measuring reaction kinetics in a lab-on-a-chip by microcoil NMR. *Lab On a chip*, 5:280–284, 2005.

[7] A. Chen and M.J. Shapiro. Affinity NMR. A new drug-screening tool that probes ligand-receptor interactions. *Analytical Chemistry*, 71(19):669 A, 1999.

[8] M. Pursch, L.C. Sander, and K. Albert. Understanding reversed-phase LC with solid-state NMR. *Analytical Chemistry*, 71(21):773 A, 1999.

[9] M. Kakuta, D.A. Jayawickrama, A.M. Wolters, A. Manz, and J.V. Sweedler. Micromixer-based time-resolved NMR: Applications to ubiquitin protein conformation. *Analytical Chemistry*, 75:956–960, 2003.

[10] A. Caprihan and E. Fukushima. Flow measurements by NMR. *Physics Reports*, 198(4):195–235, 1990.

[11] A.G. Goloshevsky, J.H. Walton, M.V. Shutov, J.S. de Ropp, S.D. Collins, and M.J. McCarthy. Integration of biaxial planar gradient coils and an RF microcoil for NMR flow imaging. *Measurement Science and Technology*, 16:505–512, 2005.

[12] J.H. Walton, J.S. de Ropp, M.V. Shutovand A.G. Goloshevsky, M.J. McCarthy, R.L. Smith, and S.D. Collins. A micromachined double-tuned NMR microprobe. *Analytical Chemistry*, 75:5030–5036, 2003.

Chapter 8

Summary and Outlook

We have demonstrated a novel concept for a DC MHD micropump, allowing the use of DC current without gas bubble perturbation in the pumping channel. We used a micromachined frit-like structure to provide electrical contact between the main channel and side reservoirs where the electrodes were located. Such a chip design allowed MHD pumping with a flow rate up to 0.3 µl·min^{-1} (mean velocity of 0.5 mm·s^{-1}) for an applied current density of 4000 A·m^{-2} in 75-µm-deep glass microchannels on top of a 0.42 T permanent magnet. We then observed and demonstrated MHD pumping in an NMR environment for the first time using a more compact MHD pump design. The pumping flow rate in the 7 T NMR superconductive magnet had a maximum of 1.5 µL·min^{-1} (mean velocity of 2.8 mm·s^{-1} in the microchannel) for an applied current density of 1600 A·m^{-2}. Table 8.1 shows a comparison of experimental conditions and main properties of our MHD pump with the state of art of DC and AC MHD micropumps. In this table, we highlight the parameters affecting the performance of such pumping systems. The pumps that had the best performance in term of flow rate and velocity are the ones where J, B and depth of channel (*h*) are maximized. In practice, they carried out those performances by maximizing the channel cross-sectional area (*A*). On the other hand, the best performances in terms of generated body force were the pumps where J, B and electrode length (*l*) were maximized. The micropumps that fulfilled this sort of performance had the electrode cross-sectional area (A_J) minimized. The body force and flow velocity generated by our pump in NMR environment has surpassed all previously published MHD pumps this far. In our system, we achieved such performances by minimizing A_J and maximizing J. Preliminary experiments with interconnected glass MHD pump and SU-8 microchannel[1] were interrupted by fluidic connection perturbations with the SU-8 channel. The description of envisioned applications involving the combination of MHD pumping and NMR detection indicate the need in NMR techniques for flow rates in the range of 0.1 to 240 $\mu L \cdot min^{-1}$. The high performances of MHD pumps at relatively low flow rates are therefore seen as an asset for NMR and MRI applications. Both examples of possible use of MHD in NMR devices are feasible if both systems are integrated in one monolithic microfluidic system.

Outlook

Future research about MHD pumping with integrated NMR detection should first focus on the integration within one monolithic chip of both functionalities. An NMR coil generating the analyzing magnetic field in the same plane as the MHD pump [7] is necessary for proper function of the chip. The performance in terms of generated MHD flow rate should also be raised by a minimum factor of 10 (and maximum 150) for the pump to be indispensable for NMR analysis applications.

The parasite eof flow originating from the side-channels (in the direction perpendicular to MHD pumping) was not studied in detail. A meticulous eof experimental study as a function of the pumped buffer's ionic strength and surface chemistry of the microfluidic system could help to better understand eof side effects on the micropump performances. Changing the surface chemistry of the glass microchip with a hydrophillic uncharged molecule (like sugars) should help the user reducing eof, as uncharged surfaces should drop the zeta potential at the channel walls (in best cases, down

---

[1] with integrated NMR microcoils on top

	U (V)	I (mA)	A (mm^2)	A_J (mm^2)	l (mm)	J ($A \cdot m^{-2}$)	B (T)	ΔP_{MHD} (Pa)	v_{MHD} ($mm \cdot s^{-1}$)	Q_{MHD} ($\mu L \cdot min^{-1}$)
Jang *et al.* [1]	30 DC	1.8	0.4	30	30	60	0.44	1	2.6*	63*
Leventis *et al.* [2]	>1.3 DC	35	18	225	75	155	1.35	16	0.4	$450 \cdot 10^3$
Bau *et al.* [3]	4 DC	15	1.9	292	172	51	0.4	3.5	0.4	45
Lemoff *et al.* [4]	6.6 AC	140	0.2	1.5	4	92105	0.013	5	1.5	18
West *et al.* [5]	5 AC	90	0.2	5	28	17684	0.011	5.5	0.24	3
Eijkel *et al.* [6]	4 AC	40	$6 \cdot 10^{-3}$	2	63	21100	0.1	133	0.04	$14 \cdot 10^{-3}$
Chapter 4	16 DC	4.8	$8.8 \cdot 10^{-3}$	1.2	16	4000	0.42	27	0.5	0.3
Chapter 6	19 DC	2	$8.8 \cdot 10^{-3}$	1.2	16	1600	7.05	180	2.8	1.5

Table 8.1: Performance comparison of previously published MHD pumps with our MHD pump presented in Ch 4 and 6. All values for voltage (U), current (I), channel cross-sectional area (A), total length of electrodes along the pumping channel (l), MHD flow mean velocity in the pumping channel (v_{MHD}) and MHD flow rate (Q_{MHD}) were experimental data, and were taken from references [1–6]. Most of the values for the electrode cross-sectional area (A_J) and current density (J) across the pumping channel had to be calculated. The body force (ΔP_{MHD}) generated by the pumps was calculated thanks to relation 2.14. **Both values were taken from experimental measurements. If calculated with relations 2.16 and 2.15, the predicted velocity and flow rate would be 0.16 $mm \cdot s^{-1}$ and 4 $\mu L \cdot min^{-1}$ respectively.*

to zero). On the other hand, this eof side-effect from the side channels could be exploited and amplified to transform the pump into a micro-mixer.

Bibliography

[1] J. Jang and S.S. Lee. Theoretical and experimental study of MHD magnetohydrodynamic micropump. *Sensors and Actuators A*, 80:84–89, 2000.

[2] N. Leventis and X. Gao. Magnetohydrodynamic electrochemistry in the field of Nd-Fe-B magnets. Theory, experiment, and application in self-powered flow delivery systems. *Analytical Chemistry*, 73:3981–3992, 2001.

[3] H.H. Bau, J. Zhong, and M. Yi. A minute magnetohydrodynamic (MHD) mixer. *Sensors and Actuators B*, 79:207–215, 2001.

[4] A.V. Lemoff and A.P. Lee. An AC magnetohydrodynamic micropump. *Sensors and Actuators B*, 63:178–185, 2000.

[5] J. West, B. Karamata, B. Lillis, J.P. Gleeson, J. Alderman, J.K. Collins, W. Lane, A. Mathewson, and H. Berney. Application of magnetohydrodynamic actuation to continuous flow chemistry. *Lab On a Chip*, 2:224–230, 2002.

[6] J.C.T. Eijkel, C. Dalton, C.J. Hayden, J.P.H. Burt, and A. Manz. A circular ac magnetohydrodynamic micropump for chromatographic applications. *Sensors and Actuators B*, 92:215–221, 2003.

[7] K.R. Minard, G.R. Holtom, L.E. Kathmann, P.D. Majors, B.D. Thrall, and R.A. Wind. Simultaneous 1H PFG-NMR and confocal microscopy of monolayer cell cultures: Effects of apoptosis and necrosis on water

diffusion and compartmentalization. *Magnetic Resonance in Medicine*, 52:495–505, 2004.

Appendix A

Glossary

Latin Symbols	**Description**	**SI Units**
a	Valence of ion	
A	Channel cross-sectional area	[m^2]
A_J	Electrode cross-sectional area	[m^2]
B	Magnetic field	[T]
C	Concentration	[$\mathrm{kg \cdot m^{-3}}$]
C_{dl}	Double layer capacitance	[$\mathrm{C \cdot V^{-1}}$]
D	Diffusion coefficient	[$\mathrm{m^2 \cdot s^{-1}}$]
D_h	Hydraulic diameter	[m]
ΔE	Transition energy	[J]
E	Electric field	[$\mathrm{V \cdot m^{-1}}$]
E^0	Redox standard potential	[V]
E_p	Electrode potential	[V]
F	Faraday constant	[$\mathrm{C \cdot mol^{-1}}$]
F_L	Lorentz force	[N]
G	Magnetic field gradient	[$\mathrm{T \cdot m^{-1}}$]
h	Planck's constant	[$\mathrm{J \cdot s}$]
h	Height of channel	[m]

H_a	Hartmann number	
I	Electric current	[A]
I_n	Nuclear spin	
J	Current density	[A$\cdot$m^{-2}]
k	Boltzmann's constant	[J$\cdot$K^{-1}]
L	Length of channel	[m]
L	Angular momentum	[J$\cdot$s^{-1}]
l	Length of electrodes	[m]
m	Nuclear moment	[A$\cdot$m^2]
m	Mass	[kg]
M	Macroscopic magnetization	[A$\cdot$m^{-1}]
N	Number of moles	[mol]
P	Pressure	[Pa]
q	Charge of a particle	[C]
Q	Volumetric flow rate	[m$^3\cdot$s^{-1}]
Q_d	Power dissipation	[W$\cdot$m^{-1}]
r	Radius	[m]
R	Electrical resistance	[Ω]
Re	Reynolds number	
Re_t	Transitional Reynolds number	
Rm	Magnetic Reynolds number	
R_{hy}	Hydraulic resistance	[N$\cdot$s$\cdot$m^{-5}]
t	Time	[s]
T	Absolute temperature	[K]
U	Applied voltage	[V]
v	Velocity	[m$\cdot$s^{-1}]
V	Volume	[m^3]
w	Width of channel	[m]

Greek Symbols	**Description**	**SI Units**
δ	Chemical shift (in ppm)	
δ	Thickness	[m]
ε	Dielectric constant of the medium	$[\mathrm{C\cdot V^{-1}\cdot m^{-1}}]$
η	Kinematic viscosity	$[\mathrm{m^{2}\cdot s^{-1}}]$
γ	Gyromagnetic ratio	$[\mathrm{rad\cdot T^{-1}\cdot s^{-1}}]$
λ	Magnetic diffusivity	$[\mathrm{m^{2}\cdot s^{-1}}]$
μ	Absolute viscosity	[Pa·s]
μ_m	Magnetic permittivity	$[\mathrm{V\cdot s\cdot A^{-1}\cdot m^{-1}}]$
ν_0	Frequency	[Hz]
ω	Angular frequency	$[\mathrm{s^{-1}}]$
ρ	Density	$[\mathrm{kg\cdot m^{-3}}]$
ρ_e	Charge density	$[\mathrm{C\cdot m^{-3}}]$
ϱ	Resistivity	[Ω·m]
σ	Electrical conductivity	$[\mathrm{S\cdot m^{-1}}]$
θ	Angle	[rad]
ζ	Zeta potential	[V]

Abbreviation	**Description**
1-D	One dimensional
AC	Alternating current
CVD	Chemical vapor deposition
DC	Direct current
DI	Deionized
ek	Electrokinetic
ep	Electrophoretic
eo	Electro-osmotic
eof	Electro-osmotic flow
EPFL	Ecole polytechnique fédérale de Lausanne
FID	Free induction decay
IMM	Institute of microelectronics and microsystems
IMT	Institut de microtechnique
LMIS3	Laboratoire de microsystèmes n°3
MHD	Magnetohydrodynamic
MRI	Magnetic resonance imaging
NMR	Nuclear magnetic resonance
PDMS	poly(dimethylsiloxane)
SAMLAB	Sensors, actuators, and microsystems laboratory
SU-8	High aspect ratio Epoxy based photoresist
UNINE	Université de Neuchâtel
µTAS	Micro total analysis system

Appendix B

MHD pump details

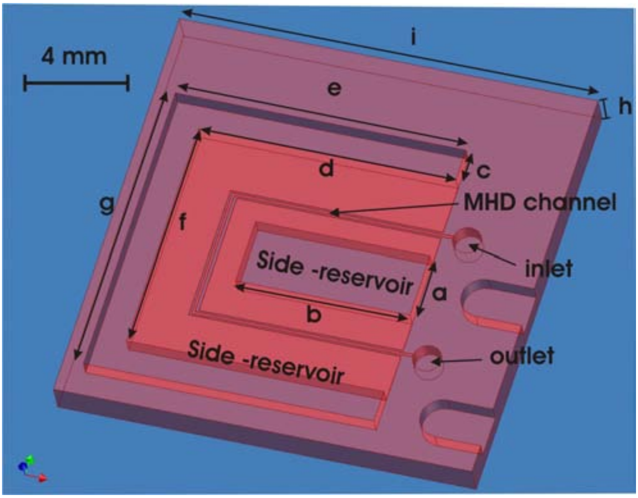

Figure B.1: Three dimensional drawing of the MHD pump (Drawing courtesy of F. Lucklum). The dimensions of the side reservoirs openings were: a = 2.35 mm, b = 5.2 mm, c = 1.3 mm, d = 7.2 mm, e = 8.4 mm, f = 6.35 mm, g = 8.95 mm, h = 1 mm, i = 12.65 mm. We measured the dimensions on a processed chip, with a precision of ± 0.05 mm.

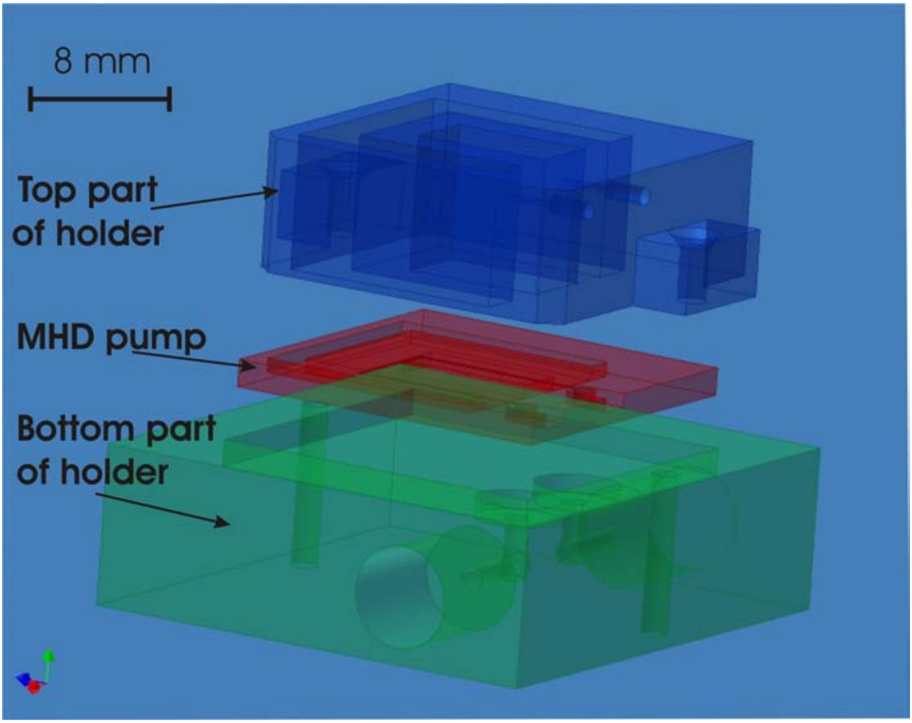

Figure B.2: Three dimensional drawing of the holder.

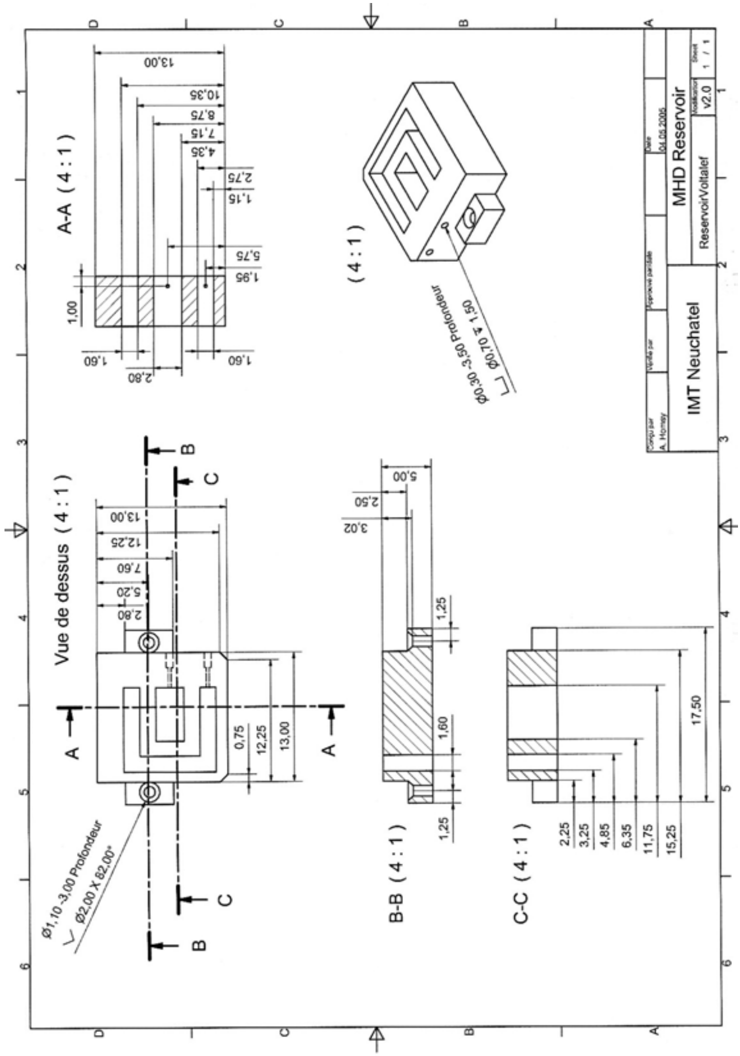

Figure B.3: Technical drawing of the top part of holder with detailed dimensions and views.

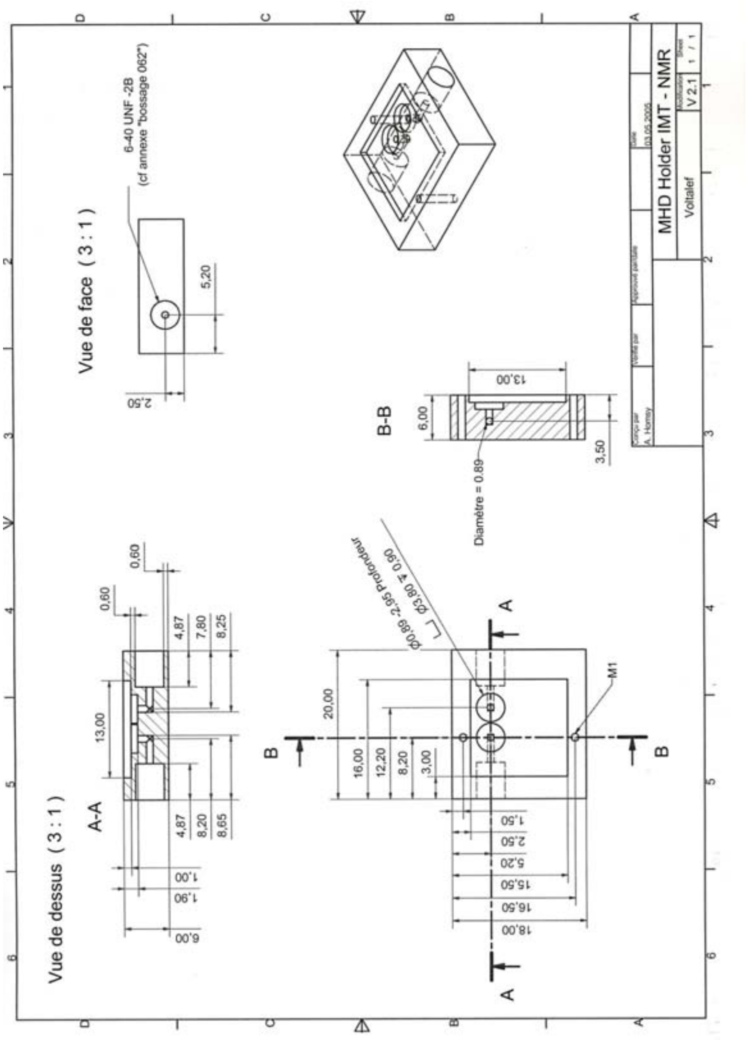

Figure B.4: Technical drawing of the bottom part of holder with detailed dimensions and views.

Appendix C

Classification of Magnetic Materials

All materials can be classified in terms of their magnetic behavior falling into one of five categories depending on their bulk magnetic susceptibility. The two most common types of magnetism are diamagnetism and paramagnetism, which account for the magnetic properties of most of the periodic table of elements at room temperature (see Fig. C.1). These elements are usually referred to as non-magnetic, whereas those which are referred to as magnetic are actually classified as ferromagnetic. The only other type of magnetism observed in pure elements at room temperature is antiferromagnetism. Finally, magnetic materials can also be classified as ferrimagnetic although this is not observed in any pure element but can only be found in compounds, such as the mixed oxides, known as ferrites, from which ferrimagnetism derives its name.

Diamagnetism

In a diamagnetic material the atoms have no net magnetic moment when there is no applied field. Under the influence of an applied field (B) the spinning electrons precess and this motion, produces a magnetisation (M) in the opposite direction to that of the applied field. All materials have a diamagnetic effect, however, it is often the case that the diamagnetic effect is masked by the larger paramagnetic or ferromagnetic term. The value of susceptibility is independent of temperature. Most elements in the periodic table are diamagnetic materials, including copper, silver, gold, glass, or water.

Paramagnetism

Paramagnetic metals have a small and positive susceptibility to magnetic fields. These materials are slightly attracted by a magnetic field and the material does not retain the magnetic properties when the external field is removed. Paramagnetic properties are due to the presence of some unpaired electrons and from the realignment of the electron orbits caused by the external magnetic field. Paramagnetic materials include platinum, magnesium, lithium, and tantalum.

Ferromagnetism

Ferromagnetic materials have a large and positive susceptibility to an external magnetic field. They exhibit a strong attraction to magnetic fields and are able to retain their magnetic properties after the external field has been removed. Ferromagnetic materials have some unpaired electrons so their atoms have a net magnetic moment. They get their strong magnetic properties due to the presence of magnetic domains. In these domains, large numbers of atoms moments (1012 to 1015) are aligned parallel so that the magnetic force within the domain is strong. When a ferromagnetic material is in the demagnetized state, the domains are nearly randomly organized and the net magnetic field for the part as a whole is zero. When a magnetizing force is applied, the domains become aligned to produce a strong magnetic field within the part. Iron, nickel, and cobalt are examples of ferromagnetic materials. Components with these materials are commonly inspected using the magnetic particle method. Iron, for example, is a ferromagnetic material.

Antiferromagnetism

In the periodic table the only element exhibiting antiferromagnetism at room temperature is chromium. Antiferromagnetic materials are very similar to ferromagnetic materials but the exchange interaction between neighboring atoms leads to the anti-parallel alignment of the atomic magnetic moments. Therefore, the magnetic field cancels out and the material appears to behave in the same way as a paramagnetic material. Like ferromagnetic materials these materials become paramagnetic above a transition temperature, known as the Néel temperature, T_N. (Cr: $T_N = 37^{o}C$).

Ferrimagnetism

Ferrimagnetism is only observed in compounds, which have more complex crystal structures than pure elements. Within these materials the exchange interactions lead to parallel alignment of atoms in some of the crystal sites and anti-parallel alignment of others. The material breaks down into magnetic domains, just like a ferromagnetic material and the magnetic behavior is also very similar, although ferrimagnetic materials usually have lower saturation magnetization.

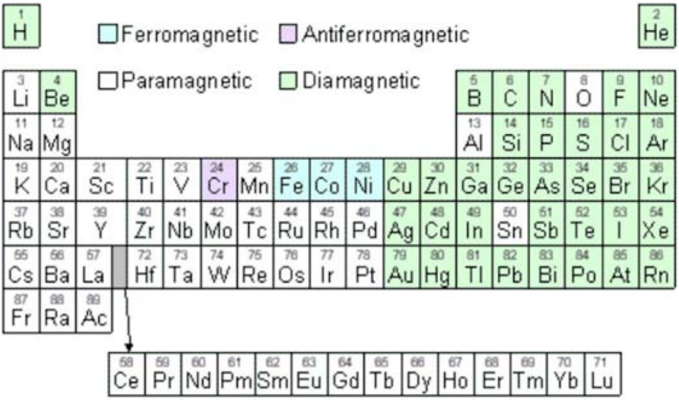

Figure C.1: Periodic table showing the type of magnetic behavior of each element at room temperature.

Appendix D

Citrate-Phosphate buffer preparation

The table showed next page was extracted from a paper written by P.J. Elving *et al.* in 1956. Elving *et al.* described the way to fabricate buffer solutions of varying pH but constant ionic strength. The buffer compositions were selected from the McIlvaine formulas, and the desired ionic strength is maintained by the addition of potassium chloride.

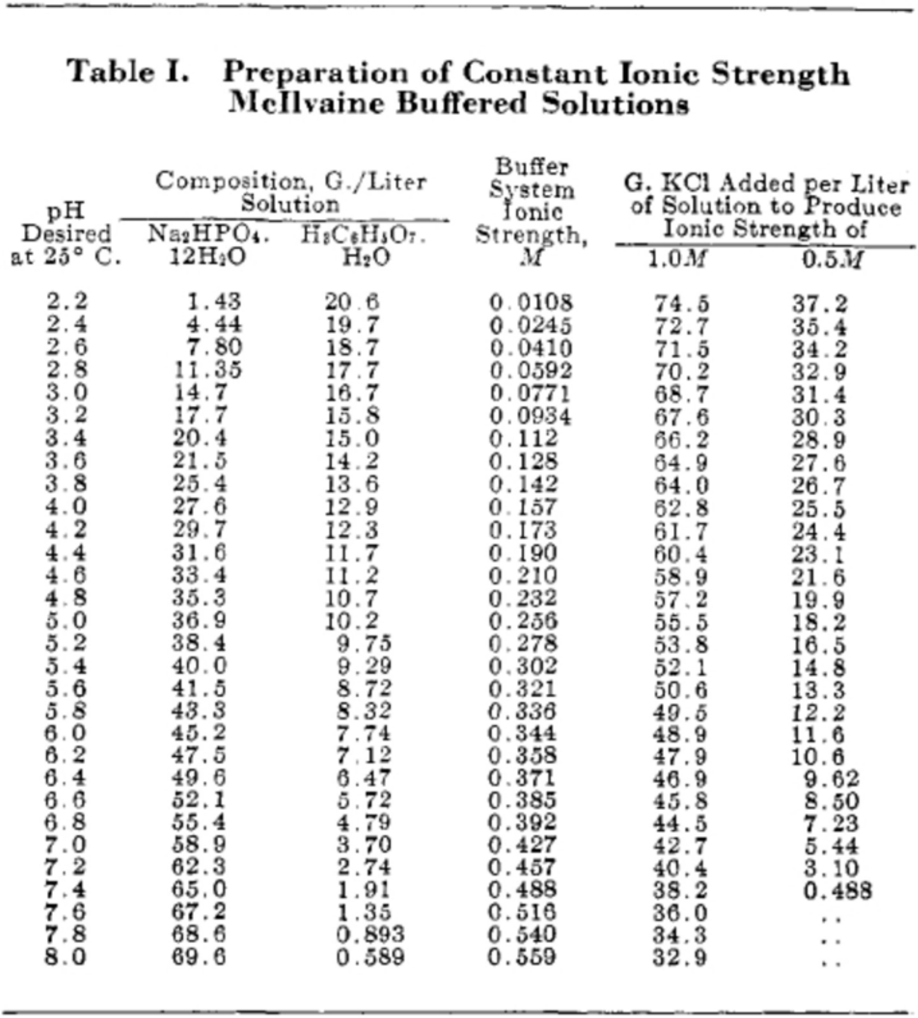

Table I. Preparation of Constant Ionic Strength McIlvaine Buffered Solutions

pH Desired at 25° C.	Composition, G./Liter Solution		Buffer System Ionic Strength, *M*	G. KCl Added per Liter of Solution to Produce Ionic Strength of	
	$Na_2HPO_4 \cdot 12H_2O$	$H_3C_6H_5O_7 \cdot H_2O$		1.0*M*	0.5*M*
2.2	1.43	20.6	0.0108	74.5	37.2
2.4	4.44	19.7	0.0245	72.7	35.4
2.6	7.80	18.7	0.0410	71.5	34.2
2.8	11.35	17.7	0.0592	70.2	32.9
3.0	14.7	16.7	0.0771	68.7	31.4
3.2	17.7	15.8	0.0934	67.6	30.3
3.4	20.4	15.0	0.112	66.2	28.9
3.6	21.5	14.2	0.128	64.9	27.6
3.8	25.4	13.6	0.142	64.0	26.7
4.0	27.6	12.9	0.157	62.8	25.5
4.2	29.7	12.3	0.173	61.7	24.4
4.4	31.6	11.7	0.190	60.4	23.1
4.6	33.4	11.2	0.210	58.9	21.6
4.8	35.3	10.7	0.232	57.2	19.9
5.0	36.9	10.2	0.256	55.5	18.2
5.2	38.4	9.75	0.278	53.8	16.5
5.4	40.0	9.29	0.302	52.1	14.8
5.6	41.5	8.72	0.321	50.6	13.3
5.8	43.3	8.32	0.336	49.5	12.2
6.0	45.2	7.74	0.344	48.9	11.6
6.2	47.5	7.12	0.358	47.9	10.6
6.4	49.6	6.47	0.371	46.9	9.62
6.6	52.1	5.72	0.385	45.8	8.50
6.8	55.4	4.79	0.392	44.5	7.23
7.0	58.9	3.70	0.427	42.7	5.44
7.2	62.3	2.74	0.457	40.4	3.10
7.4	65.0	1.91	0.488	38.2	0.488
7.6	67.2	1.35	0.516	36.0	..
7.8	68.6	0.893	0.540	34.3	..
8.0	69.6	0.589	0.559	32.9	..

Figure D.1: Table for the preparation of the constant ionic strength buffer. This table was taken from P.J. Elving *et al.*

Acknowledgements

My greatest thanks go to Professor Nico de Rooij for giving me the opportunity to follow my PhD research in his group, and for those past four wonderful years. Thank also to Sabeth Verpoorte who accepted me as one of her PhD students within the µTAS team.

My special thanks go to Milena Koudelka-Hep and Peter van der Wal, who were always available to answer my "stupid" questions about chemistry and electrochemistry. Your support has been highly valuable to a humble physicist.

I also gratefully acknowledge Jan Eijkel, of the lab on a chip group at the university of Twente in The Netherlands, and Prof. Radivoje Popovic, of the microsystems design group at EPFL, for kindly agreeing to be the co-examiners of my PhD thesis.

This work wouldn't have been possible without the valuable financial support provided by an EPFL Presidential Fund (Nr. 581.552) and by the Swiss National Science Foundation (Project Nr. 2100-61549.00).

Great thanks to Sander Koster and Vincent Linder for their support in the management of my project. And to a great extend to all of my fellow µTAS-colleagues Jan Lichtenberg, Frieder Lucklum, Anpan Han, Anna-Maria Spehar, Tobias Kraus, Gian-Luca Lettieri, Arash Dodge, Laura Ceriotti, Roos Guijt, and Nathan Lacher.

Thanks to Charles Massin, Franck Vincent, Klaus Ehrmann, Pierre-Andre Besse, and Giovanni Boero for their support in the NMR and magnetic part of the project.

The microfabrication of the devices presented in this thesis would not have been possible without the help of IMT's very valuable technical team: Sylvain Jeannneret, Gianni Mondin, Edith Milotte, Nicole Hegelbach-Guye, Giovanni Bergonzi, Pierre-André Clerc, Sabina Jenny, Sylviane Pochon, and José Vaquera. Your valuable help and great mood was always greatly appreciated. Thanks also to Claudio Novelli for his patience and great skills towards all my computer worries... Thanks to Florence Rohrbach and Karine Frossard for their secretarial work. Mireille Leboeuf and Massoud Dadras have contributed to the beautiful electron microscope images seen in this work.

I give my deepest thank my friend Laure Aeschimann, who introduced me to SAMLAB for the first time. This journey wouldn't have been the same without your friendship and support all through the years here in Neuchatel, but also during our studies in EPFL Lausanne. Thanks also to Luca Berdondini for our valuable and highly motivating scientific discussions in the train on our way home to Lausanne. I thank also all of you in the SAMLAB group for the unforgettable friendly and efficient team atmosphere.

The daily travel from Lausanne to Neuchatel in the train wouldn't have been the same without all the people I met during this journey. Thanks to all of you for your friendship!

A special thanks to my friend Sumita Pennathur, from the Mechanical Engineering Department at Stanford University, who patiently verified and carefully corrected my english in every chapter of this thesis.

Thank you Remo for your love, your friendship, and unlimited patience during this whole writing of thesis.

And last but not least, I would like to give my endless thanks to my parents and to my sister. Without your infinite love and support none of this would have ever been possible. I love you! Thank you XXX

Publications

List of publications

C. Massin, F. Vincent, A. Homsy, K. Ehrmann, G. Boero, P.-A. Besse, A. Daridon, E. Verpoorte, N.F. de Rooij, and R.S. Popovic. *Planar microcoil-based microfluidic NMR probes*. Journal of Magnetic Resonance **164**, 286-293 (2003).

A. Homsy, S. Koster, J.C.T. Eijkel, A. van den Berg, F. Lucklum, E. Verpoorte, and N.F. de Rooij. *A high current density DC magnetohydrodynamic (MHD) micropump*. Lab On a Chip **5**, 466-471 (2005).

A. Homsy, V. Linder, F. Lucklum, and N.F. de Rooij. *Magnetohydrodynamic Pumping in Nuclear Magnetic Resonance Environments*. Sensors and Actuators B: Chemical (accepted September 2006).

Contribution to Conferences

Oral presentation

A. Homsy, S. Koster, J.C.T. Eijkel, A. van den Berg, E. Verpoorte, and N.F. de Rooij, *A high flow rate DC magnetohydrodynamic (MHD) micropump*. Presented at the Micro-TAS 2004 Conference, Malmo, Sweden, **Proceed-**

ings pp. 372-374, Sept. 26-30 (2004).

Posters

A. Homsy, N.F. de Rooij, E. Verpoorte, C. Massin, F. Vincent, G. Boero, P.A. Besse, R.S. Popovic. *Glass technology for microfluidic channels with symmetric cross-Sections*. 3rd CMI-ComLab revue, Ecole Polytechnique Fédérale de Lausanne, Lausanne, Switzerland (2002).

A. Homsy, J. Lichtenberg, C. Massin, F. Vincent, P.-A. Besse, R.S. Popovic, N.F. de Rooij, and E. Verpoorte. *Fabrication of microfluidic channels with symmetric cross-sections for integrated NMR analysis*. Micro-TAS 2002 Conference, Nara, Japan, **Proceedings** pp. 115-117, Nov. 3-7 (2002).

A. Homsy, S. Koster, E. Verpoorte, N.F. de Rooij. *Microfluidic system for integrated NMR analysis and MHD pumping*. GRC Physics and Chemistry of Microfluidics conference, Big Sky, Montana, USA (2003).

A. Homsy, S. Koster, N.F. de Rooij. *Glass technology for microfluidic channels with integrated platinum electrodes*. 5th CMI-ComLab revue, Ecole Polytechnique Fédérale de Lausanne, Lausanne, Switzerland (2004).

A. Homsy, S. Koster, N.F. de Rooij. *A high current density magnetohydrodynamic (MHD) micropump*. 6th CMI-ComLab revue, Ecole Polytechnique Fédérale de Lausanne, Lausanne, Switzerland (2005).

A. Homsy, F. Lucklum, V. Linder, N.F. de Rooij. *Magnetohydrodynamic pumping in nuclear magnetic environments*. GRC Physics and Chemistry of Microfluidics conference, Oxford, GB (2005).